AN ABSTRACT OF THE DISSERTATION OF

Lily Ranjbar for the degree of Doctor of Philosophy in Radiation Health Physics presented on March 9, 2016.

Title: A Two-element CZT-based Radioxenon Detection System for Nuclear Weapon Test Monitoring

Abstract approved:

_____

Abi T. Farsoni

Detection of xenon radioisotopes (radioxenons) has proven to be an important method for detecting nuclear explosions and is particularly well suited for detecting undeclared underground testing. The radioxenon isotopes ^{131m}Xe ($t_{1/2}$ = 11.934 d), ^{133m}Xe ($t_{1/2}$ = 2.19 d), ^{133}Xe ($t_{1/2}$ = 5.243 d) and ^{135}Xe ($t_{1/2}$ = 9.14 h) are produced in significant amounts in nuclear explosions and are of particularly high-value in identifying such events and thus are the focus of current radioxenon detection systems.

The main objective of this dissertation is to design, build and test a new radioxenon detection system to study the response of CdZnTe (CZT) detectors to xenon

radioisotopes in order to support the CTBT for discovering clandestine nuclear weapon tests. This prototype detection system was intended to be small and compact with minimal number of channels which reduces complexity, power and size and still can achieve good energy resolution at room temperature compared with other scintillator-based radioxenon detectors. The prototype design uses two CZT crystals for this purpose, with the ultimate goal of using six CZT crystals for optimum geometric efficiency. The system measures xenon radioisotopes through beta-gamma coincidence detection between the two detection elements.

The CZT-based detection system was characterized with radioactive lab sources and four radioxenons produced in the OSU's TRIGA reactor. The detection system offers excellent energy resolution and background count rate compared with scintillator-based beta-gamma coincidence detectors currently in operation at the IMS stations.

The detection system was also simulated using MCNP to understand the response of the system to radioxenons of interest. PTRAC card was used for this purpose to find the track of beta/conversion electrons and gamma/X-rays in each CZT detector. The MCNP simulations were compared with the measurement results and shows very good consistency.

The minimum detectable concentration (MDC) of this system for ^{133}Xe is estimated to be less than the requirement set by the IMS (1 mBq/m^3). Our estimations also show that by increasing the number of CZT crystals to 6, the MDC of all radioxenons will be improved to less than 1 mBq/m^3 which is comparable with the most sensitive radioxenon detection systems currently in operation.

A Two-element CZT-based Radioxenon Detection System for Nuclear Weapon Test Monitoring

by
Lily Ranjbar

A DISSERTATION
Submitted to

Oregon State University

in partial fulfillment of
the requirements for the
degree of

Doctor of Philosophy

Presented March 9, 2016
Commencement June 2016

Doctor of Philosophy dissertation of Lily Ranjbar presented on March 9, 2016.

APPROVED:

Major Professor, representing Radiation Health Physics

Head of the School of Nuclear Science and Engineering

Dean of the Graduate School

I understand that my dissertation will become part of the permanent collection of Oregon State University libraries. My signature below authorizes release of my dissertation to any reader upon request.

Lily Ranjbar, Author

ACKNOWLEDGEMENTS

To my spouse, Ali, thank you for being a continuous source of love, help, support and encouragement from the beginning of this journey all the way to the end. I am deeply grateful to have you by my side.

To my parents, thank you for all of your love, support and inspiration throughout my life, especially during my education from the starting point until now. I cannot conceive of much less ask for, better parents.

To my sister and brothers, thank you for being always there for me not only as my siblings but also as my best friends and help me whenever I needed.

To my advisor Dr. Abi Farsoni, thank you for giving me the opportunity to work under your supervision in one of the most advanced detection labs. Thank you for your help, guidance and support throughout this work. Working with you, I have learned highly valuable technical skills and gained a lot of knowledge and experience. I'm always impressed by your knowledge and hard work.

To my doctoral committee members, Dr. Kenneth Krane, Dr. David Hamby, Dr. Hoari Yang and Dr. Huaping Liu, thank you for accepting to be on my committee and for your help and guidance throughout this work.

To those who have helped me along the way: thank you for your contributions! Specifically:

Thank you to my friend and lab mate Dr. Eric Becker for all your help, support and valuable comments you provided for me during my PhD years. You were always ready to help me, whenever I asked for; thank you to Dr. Bemnet Alemayehu for letting me to work with you and teaching me a lot about radioxenon detectors; thank you Salam Alhawsawi for helping me in the lab and the clean room and for great discussion we had always about our projects in the office; thank you all my friends here in Corvallis especially my Persian that made the past 3.5 years enjoyable.

TABLE OF CONTENTS

Page

LIST OF FIGURES

LIST OF FIGURES (Continued)

Figure Page

LIST OF FIGURES (Continued)

Figure Page

LIST OF FIGURES (Continued)

Figure Page

LIST OF FIGURES (Continued)

Figure Page

LIST OF FIGURES (Continued)

Figure Page

LIST OF TABLES

If you split a particle
You'll find a sun inside of it
Hatif Isfahani, 18th century Persian poet

1 Introduction

1.1 Overview

The Comprehensive Nuclear-Test-Ban Treaty (CTBT) is a multilateral treaty that bans all civilian and military nuclear explosions in all environments [1]. The International Monitoring System (IMS) is a worldwide network of observational technology that was established to detect and confirm violations of the CTBT. Monitoring xenon radioisotopes, often referred to as radioxenons, released from nuclear detonations is an important method the IMS uses to verify violations of the CTBT and provide unambiguous proof for the nuclear nature of any detected explosion. Thus, developing new and advanced radioxenon detection systems with high sensitivity and ease of operation is an immediate need for the IMS to support the CTBT [2].

Different radioxenon detectors have been developed and tested over the past decade to facilitate nuclear weapon test monitoring. Four different radioxenon detectors are currently deployed at various IMS stations around the globe to monitor atmospheric concentrations of radioxenons [3]. These detectors work either based on beta-gamma coincidence (ARSA (USA), SAUNA (Sweden) and ARIX (Russia)) [4]–[6] or high-resolution gamma-ray spectroscopy (SPALAX (France)) [7].

The current radioxenon detection systems have been able to detect signs of nuclear explosions in the past such as Fukushima accident in 2011 and North Korea nuclear weapon tests in 2006, 2010 and 2013 [8]–[18]. However, these detection systems do possess some

disadvantages. Detectors based on plastic scintillators are subject to the memory effect, which degrades the sensitivity of the system due to added background from previous radioxenon measurements. Detection systems relying on multiple readout instruments are difficult to calibrate and match, and detection systems that use high-purity germanium, like SPALAX, require a maintenance-intensive liquid nitrogen cooling system, both of which are not conducive to unattended systems.

In order for radioxenon monitoring to be more reliable at remote locations, it is vital to develop automated detection systems that could be operable unattended. They must also be sensitive enough to measure trace amounts of radioxenons in the atmosphere. To meet these requirements, address the aforementioned issues with the current detection systems, and to study the response of CZT detectors to radioxenons, a new radioxenon detection system was designed, built and tested at OSU based on this well-known room temperature semiconductor material and a beta-gamma coincidence technique. It is the first time that such a material is being used for radoxenon detection. The prototype device is shown in Figure 1-1.

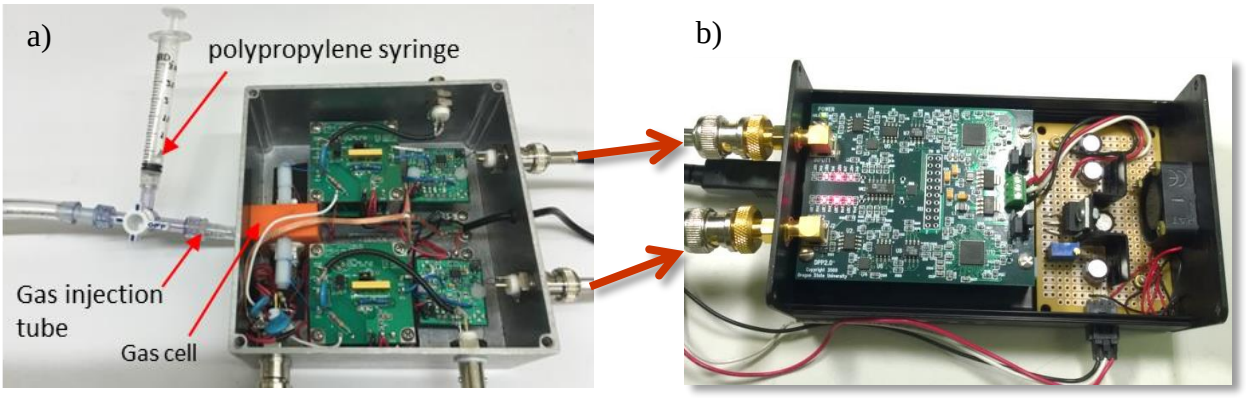

Figure 1-1. The full TECZT radioxenon detection system and electronics, showing a) The radioxenon sample syringe, gas injection tube, TECZT detector assembly, preamplifiers, and subtraction circuits, and b) The two-channel digital pulse processor.

The prototype design, namely *Two-Element Coplanar CZT* (TECZT) detection system utilizes two face-to-face coplanar CZT detectors for coincidence detection of beta/conversion electrons and gamma/X-rays with the ultimate goal of using six CZT crystals for optimum geometric efficiency.

CZT detectors used in this system are capable of excellent energy resolution compared with other scintillator-based beta-gamma coincidence detectors currently in operation. Another advantage of CZT detectors is their capability to be operated at room temperature, making the system lower maintenance compared to radioxenon detection systems relying on the maintenance-intensive, cryogenically-cooled HPGe detectors.

The new CZT-based radioxenon detection system is also expected to significantly reduce the memory effect [19] which is currently observed with radioxenon detectors that use plastic scintillators. The high-Z nature of the CZT material is anticipated to minimize radioxenon diffusion into the detector elements compared to the low-Z nature of plastic scintillator materials. A reduction in memory effect will lead to improvements in the Minimum Detectable Concentration (MDC) of the detection system for all xenon radioisotopes.

1.2 Goals

This work covers the design, construction, and characterization of the TECZT prototype device.

The specific areas of the characterization for the complete device includes:

- General design and assembly

- MCNP simulation

- Coincidence module in FPGA
- Optimum cathode and grids bias voltages
- Optimum subtraction gain
- Optimum flat and peaking time for the digital trapezoidal filter
- Optimum CTW in FPGA
- General characterization using radioactive lab sources
- Radioxenon measurements
- Minimum detectable concentration (MDC) estimations

You are not a drop in the ocean;
You are the entire ocean, in a drop.
Rumi, 13th century Persian poet

2 Literature Review

After World War II and beginning of the nuclear age, a massive number of nuclear bomb tests were carried out by the world powers. During these years, due to the arm race and cold war the safety of a world with many nuclear weapon states was a big concern for all countries with and without nuclear weapons.

Having more nuclear-weapon states would reduce security for all, multiplying the risks of miscalculation, accidents, unauthorized use of weapons, or from escalation in tensions, nuclear conflict. At this time the concern of proliferation was also came to the accounts as many other countries pursued or consider acquiring nuclear weapons. If the number of states to possess nuclear weapons continued to grow, it was believed that the risks of nuclear war would greatly increase [20]. Therefore, a number of test ban treaties were proposed and signed to reduce these concerns [1], [20]–[23]. The Comprehensive Nuclear Test-Ban Treaty (CTBT) is one of these treaties and was developed to progress on nuclear non-proliferation and disarmament.

2.1 The Comprehensive Nuclear Test-Ban Treaty (CTBT)

The Comprehensive Nuclear-Test-Ban Treaty (CTBT) was proposed in 1994 to progress on nuclear non-proliferation. CTBT was adopted on September 10, 1996. It was opened for signature on September 24, 1996. Since then, as of February 2016, 183 countries have signed the treaty, while 164 have ratified it [1], [24].

CTBT is a multilateral treaty which bans all civilian and military nuclear explosions in all

environments: under water, underground, on the earth's surface and in the atmosphere [1]. It bans nuclear explosions by everyone; therefore countries with nuclear bombs in their hand cannot make more powerful bombs, while it makes it very difficult for countries without any nuclear bomb to develop one. This treaty is observed as a vital tool for stopping development of new weapons and spread of nuclear weapons [25].

CTBT is almost universal but has not yet entered into force. The CTBT cannot enter into force until a number of specified states [1] have ratified the treaty. Therefore, the Preparatory Commission for the Comprehensive Nuclear-Test-Ban Treaty Organization (CTBTO Preparatory Commission) which is an international organization based in the Vienna International Center was established to prepare for the moment when the CTBT enters into force [26]. This preparation ensures that a global verification regime is in placed at entry into force. This verification regime must be capable of detecting nuclear explosions in all environments; in water, underground and in the atmosphere. Establishing such a comprehensive verification regime is the main job of the CTBTO [26].

2.2 International Monitoring System (IMS)

One of the key parts of the CTBTO verification regime is the International Monitoring System (IMS) [2]. IMS is a global network of monitoring stations established by the CTBTO to monitor the earth for evidence of a nuclear explosion. While it is not currently completely developed, the IMS, when fully operational, will consist of 321 monitoring stations alongside the existing 16 radionuclide laboratories [3]. Figure 2-1 shows the geographical distribution of IMS stations around the globe.

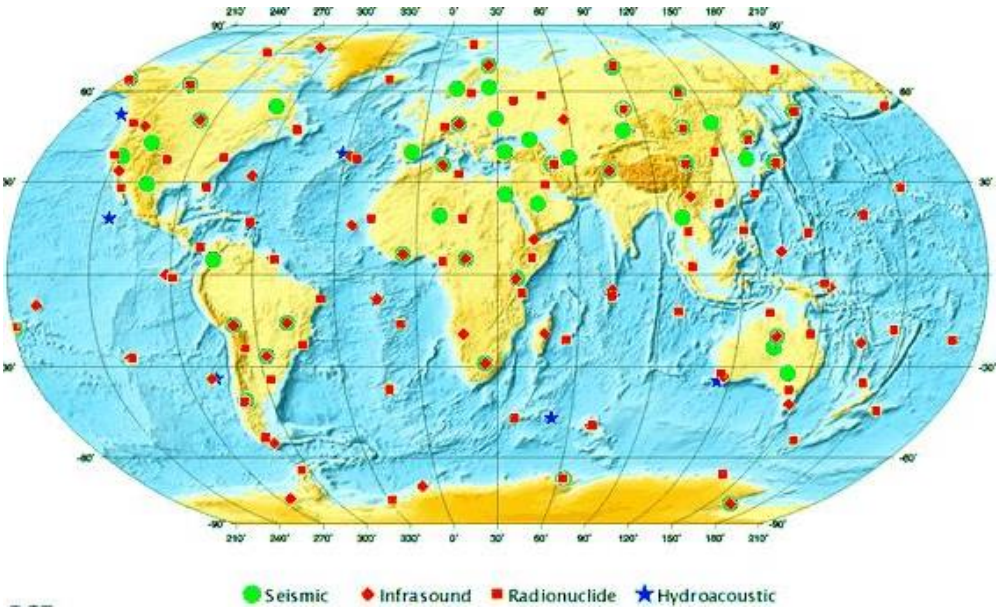

Figure 2-1. Geographical distribution of the IMS stations monitoring [27].

IMS has the advantage of using four state-of-the-art technologies to monitor nuclear explosions globally. Infrasound, hydroacoustics, forensic seismology and radionuclide monitoring are among these technologies [3]. However, these technologies are not completely effective without the inclusion of radionuclide monitoring. This method is the only method that can provide proof that any detected explosion was a nuclear detonation [2].

2.3 Monitoring Technologies for Nuclear Weapon Tests

After nuclear weapon tests, energy is released and radioactive products are created. The released energy affects the environment by the sound vibration which propagates through the ocean, earth and atmosphere. Released radioactive products with a variety of half-lives can also escape from a bomb's explosion chamber and vent out to the atmosphere. These released energy

and physical products are the basic component for the design of the monitoring technologies, hydroacoustic monitoring, seismic monitoring, infrasound monitoring and radionuclide monitoring, compliance with the CTBTO [2].

2.3.1 Hydroacoustic Monitoring

Sound waves created by nuclear explosions can travel extremely far underwater which makes it possible to record underwater signals several thousand kilometers away from the starting point. In hydroacoustic monitoring these sounds waves in the ocean are monitored to find any sign of explosions [2]. While it is not currently completely settled, the hydroacoustic monitoring, when fully functioning, will consist of 11 monitoring stations to monitor wave's sounds. This method is well suited for underwater nuclear weapon tests [2].

2.3.2 Seismic Monitoring

Waves generated by seismic events are also monitored by the seismological components of the IMS. The vast majority of the detected waves are typically generated by earthquake, but some also come from nuclear weapon tests [2]. For instance, some seismic events were detected following North Korea nuclear tests in 2006, 2009, 2013 and 2016 [28]–[31]. Therefore, the primary use of the seismic data in the verification system is to distinguish between an underground nuclear explosion and the frequent earthquakes that happen around the world.

Based on the above mentioned statements, seismic monitoring is well suited for underground tests.

The IMS seismic network consists of 50 primary stations, which send their data in real time to the International Data Centre (IDC) in Vienna, and 120 auxiliary stations that make data

available upon request from the IDC [2].

2.3.3 Infrasound Monitoring

Ultra-low frequency sound waves that are generated by large explosions and are inaudible to the human ear can be detected by 60 infrasound stations installed around the globe. The IDC uses infrasound data to locate and distinguish between atmospheric explosions and natural phenomena. Therefore, this method is well suited for atmospheric nuclear weapon tests [2].

2.3.4 Radionuclide Monitoring

Radionuclide monitoring stations are equipped to detect and measure radioactive particles and gases generated in a nuclear explosion. While it is not currently completely developed, the radionuclide monitoring, when fully operational, will consists of 80 monitoring stations installed around the globe [2]. Among these stations, 40 of them are also additionally able to detect noble gases. Radionuclide monitoring is the only method that can clearly confirm whether a detonation detected by other monitoring methods had actually a nuclear origin. This method is well suited for detecting radionuclides from all environments [2], [32], [33].

2.3.4.1 Radioxenon Monitoring

After any nuclear explosion, fission products are released either in the form of radioactive particles or radioactive noble gases. Typically the radioactive particles remain trapped in the explosion chamber during an underground test. Noble gases, however due to their inert chemical properties and their small sizes can easily escape through cracks and rocks and reach the surface, allowing for detection. By detection of these noble gases, the CTBTO can provide unambiguous evidence of a nuclear explosion or clandestine nuclear testing. Among the noble gases,

radioactive xenon (radioxenon) isotopes are produced in significant amounts [34].

Four radioxenon isotopes are of particular interest to the CTBTO: ^{131m}Xe ($t_{1/2}$ = 11.934 d), ^{133m}Xe ($t_{1/2}$ = 2.19 d), ^{133}Xe ($t1_{/2}$ = 5.243 d) and ^{135}Xe ($t_{1/2}$ = 9.14 h). The half-lives of these isotopes are long enough that they can be detected several days or even months after a nuclear explosion [35]–[37]. Table 2-1 shows characteristic energies for the decay of these radioxenons.

In addition to production in nuclear explosions, radioxenons are also released by civilian processes from nuclear reactor operations, medical isotopes facilities and hospitals and create a permanent background for radioxenon measurements [32], [33]. Therefore, detection of a single radioxenon is not sufficient to identify a nuclear weapon test and it is significantly important to distinguish between civilian-produced radioxenons and those are produced during nuclear explosions [33]. This distinction is made by the ratio of these four radioxenons, which differ meaningfully with the source of release [38].

The activity ratios of ^{133m}Xe/^{133}Xe and ^{135}Xe/^{133}Xe produced during nuclear explosions are larger by a factor 100 and 10,000, respectively, than for reactor activities. These ratios can be used to identify nuclear explosions from the civilian releases, making radionuclide monitoring the only method that can clearly confirm whether a detonation detected by other monitoring methods had actually a nuclear origin. At present the most abundant isotope is ^{133}Xe, which is released during the operation of nuclear power reactors [32], [39], [40].

Figure 2-2 shows distinction of reactor emissions from nuclear weapon tests based on Xe isotope ratios.

Table 2-1. Characteristic energies for the decay of ^{131m}Xe, ^{133m}Xe, ^{133}Xe and ^{135}Xe [3].

Isotope	Decay energy (keV)	Half-life (days)	Branching ratio (%)
^{131m}Xe		11.93	
X-rays	29.46		15.4
	29.78		28.6
	33.60		10.2
	34.61		1.85
Gamma rays	163.93		1.95
Conversion electrons	129.4		61
Coincident decays	31 keV X-rays and 129 keV CE		56.1[a]
^{133}Xe		5.25	
X-rays	30.62		14.1
	30.97		26.2
	35.00		9.4
	36.01		1.7
Gamma rays	80.99		37
Conversion electrons	45		55.1
Betas (max)	346		100
Coincident decays	31 keV X-ray+45 keV CE +346 keV beta		48.9[a]
	81 keV gamma+346 beta		37.2[a]
^{133m}Xe		2.19	
X-rays	29.46		16.1
	29.78		29.8
	33.60		10.6
	34.61		1.9
Gamma rays	233.2		10
Conversion electrons	198.7		64
Coincident decays	31 keV X-rays and 199 keV CE		58.4[a]
^{135}Xe		0.38	
X-rays	30.62		1.45
	30.97		2.69
	35.00		0.97
	36.01		0.185
Gamma rays	249.8		90
	608.2		2.9
Conversion electrons	214		5.7
Betas (max)	905		100
Coincident decays	31.63 keV X-rays+214 keVe +910 keV beta		5.7
	250 gamma+910 keV beta		90[a]

Based on this technique IMS stations have been able to detect signs of nuclear explosions

in the past. Following the Fukushima nuclear accident, ^{133}Xe was detected only four days after the incident at Pacific Northwest National Laboratory (PNNL) [8], 16 days after the accident in Xi'an, China [9] and one month after the accident at the Darwin IMS noble gas station in Australia [10]. ^{131m}Xe and ^{133}Xe were also detected 11 days after the accident in Beijing [11].

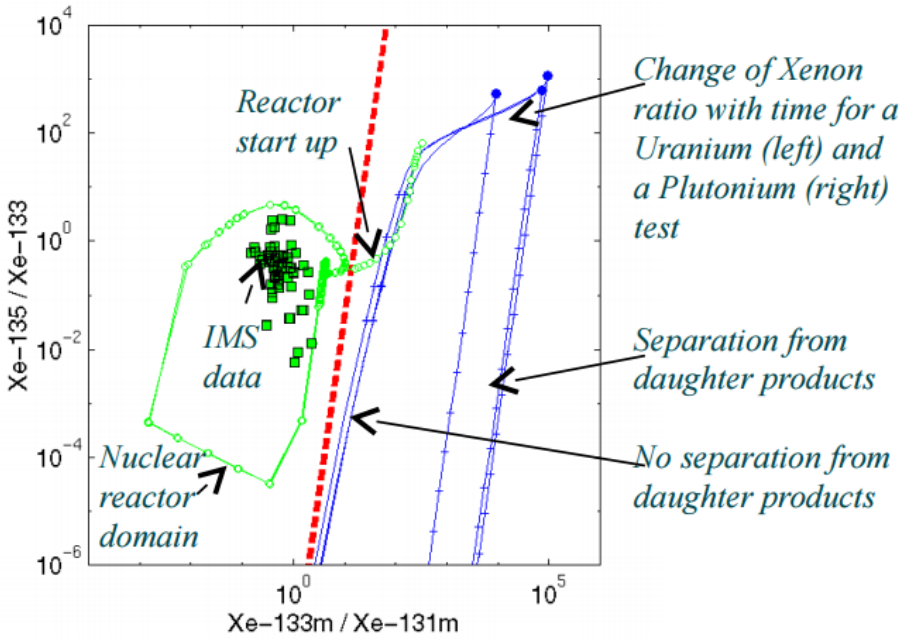

Figure 2-2. Distinction of reactor emissions from nuclear weapon tests based on Xe isotope ratios. The green area indicates the nuclear reactor production and the blue region shows weapons. The dashed red line which separates these two area is known as the possible "discrimination line" [38], [41].

Radioxenon monitoring has been very effective to detect any sign of nuclear weapon tests in the past. The announced October 2006 North Korean nuclear test was confirmed by radioxenon detection one month after the test in South Korea [12]. Radioxenons from this test were also detected 7000 km away in Canada [13]. It was the first real test showing the technical

capabilities of the verification system built by the CTBTO [14].

The North Korean nuclear weapon tests in 2010 and 2013 were also confirmed by radioxenon monitoring in various IMS stations. In 2010 multiple detection of radioxenon isotopes at various IMS stations in Eastern Asia (two in Japan and one in Russia) also indicated that a possible low-yield nuclear test had been conducted by North Korea [15], [16]. Observation of rapid changes in the ratios of ^{133}Xe and ^{131m}Xe at measurement stations in Japan and Russia indicated that they belonged to the underground nuclear test conducted by North Korea, 7-8 weeks prior (on February 12, 2013) [17], [18].

During the past decade, several radioxenon detection systems have been developed and tested for detection and measurement of radioxenon isotopes. They work either based on beta-gamma coincidence technique or high resolution gamma spectroscopy. Amongst these systems four of them are currently deployed by the IMS and are installed in various stations around the globe [42]. These systems are: the Swedish automatic unit for noble gases (SAUNA), the France's syste´me de pre´le`vements et d'analyse en ligne d'air pour quantified le xenon (SPALAX) unit, the automated radioxenon sampler and analyzer (ARSA) and analyzer of xenon radioisotopes (ARIX). Among these systems, SAUNA, ARSA and ARIX use beta-gamma coincidence technique to detect beta particles and gamma rays simultaneously, whereas, SPALAX deploys high spectral resolution gamma spectrometry [5], [6], [33], [43], [44].

Several other radioxenon detection systems have been also developed and are under improvement to meet the IMS requirements.

Table 2-2, shows some of the detection systems already developed for radioxenon

monitoring and their most important properties.

Table 2-2. Various systems developed for radioxenon detections. Among them SAUNA, ARSA, ARIX and SPALAX have been already installed in various IMS stations around the globe.

Detector Type	**Detection Materials**	**Detection Mechanism**	**MDC for ^{133}Xe (mBq/m^3)**
SAUNA	BC404 for β/CE detection NaI(Tl) for γ/X-ray detection	beta–gamma coincidence technique	0.18 [45]
SPALAX	HPGe	high spectral resolution γ spectrometry	0.15 [43]
ARSA	BC404 for β/CE detection NaI(Tl) for γ/X-ray detection	beta–gamma coincidence technique	0.5 [46]
ARIX	polystyrene organic scintillator for β/CE detection NaI(Tl) for γ/X-ray detection	β-Gated γ -Coincidence Spectrometry	0.2–0.3 [3]
PW5	BC-404 plastic for β/CE detection CSI(Tl) for γ/X-ray detection	beta-gamma coincidence technique	0.5 [47]
24-element PIN Diode	Si PIN diode	X-rays-CE Coincidence gating	0.11 [45]
OSU ASPD	BC-400 for β/CE detection CsI (Tl) for γ/X-ray detection BGO for Compton suppression	beta–gamma coincidence technique	NA
OSU WASPD	BC-400 for β/CE detection CsI (Tl) for γ/X-ray detection BGO for Compton suppression	beta–gamma coincidence technique	0.46 [34]

A set of minimum requirements for IMS radioxenon systems has been defined by the

CTBTO. These requirements partly focus on operational requirements of the IMS network, but also specify the detection requirements for IMS radionuclide stations (Table 2-3) [48]. Radioxenon detection systems must be able to detect all radioxenons separately and also must be sensitive enough to detect trace amounts of radioxenon. One of the most fundamental requirements for radioxenon detection systems is that the MDC of the detector for ^{133}Xe must be 1 mBq/m^3 of air for a 24 h sample [48].

Table 2-3. Noble gas station specifications for the IMS [33].

Characteristic	Minimum requirement
Air flow	0.4 m^3/h
Total volume of sample	10 m^3
Collection time	⩽24 h
Measurement time	⩽24 h
Time before reporting	⩽48 h
Reporting frequency	Daily
Isotopes measured	^{131m}Xe, ^{133}Xe, ^{133m}Xe, ^{135}Xe
Measurement mode	Beta-gamma coincidence or high resolution gamma-ray spectroscopy
Minimum detectable concentration	1 mBq/m^3 for ^{133}Xe
State-of-health	Status display transmitted to IDC
Communication	Two-way
Data availability	95%
Down time	⩽7 consecutive days, ⩽15 days annually

2.3.5 Available Radioxenon Detection Systems

2.3.5.1 Système de Prélèvement Automatique en Ligne avec l'Analyse du Xénon Atmosphérique (SPALAX)

The SPALAX detection system has been developed by the French Atomic Energy Commission (CEA) in the late 1990s.

Figure 2-3 shows the schematic Diagram of the SPALAX system which consists of

detection, concentration and purification and sampling unit and a typical SPALAX radioxenon detection system.

a) b)

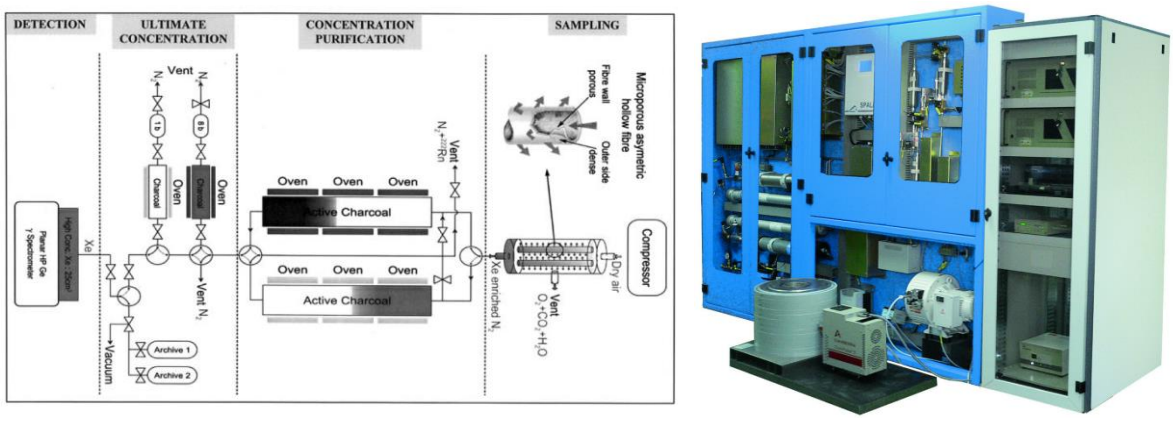

Figure 2-3. a) Schematic Diagram of the SPALAX radioxenon detection system shows sampling, purification, concentration and detection units [43]. b) A typical SPALAX radioxenon detection system [49].

SPALAX detection system differs from other radioxenon detection systems deployed at the IMS station by using a high resolution broad energy germanium (BEGe) spectrometer. All four radioxenons of interest (^{131m}Xe, ^{133m}Xe, ^{133}Xe and ^{135}Xe) are detected simultaneously using this spectrometer and are quantified by their major gamma lines [43].

The SPALAX system has the capability to sample atmospheric air and then extract, purify and concentrate radioxenons from the sampled air to be injected in the detector gas cell. In this system all four relevant radioxenons are discriminated using dual X-gamma ray spectrometry [43].

Figure 2-4 shows an example of gamma spectrum obtained by the SPALAX system. As it

is illustrated in this figure 81 keV X-rays from ^{133}Xe is clearly detected by this system.

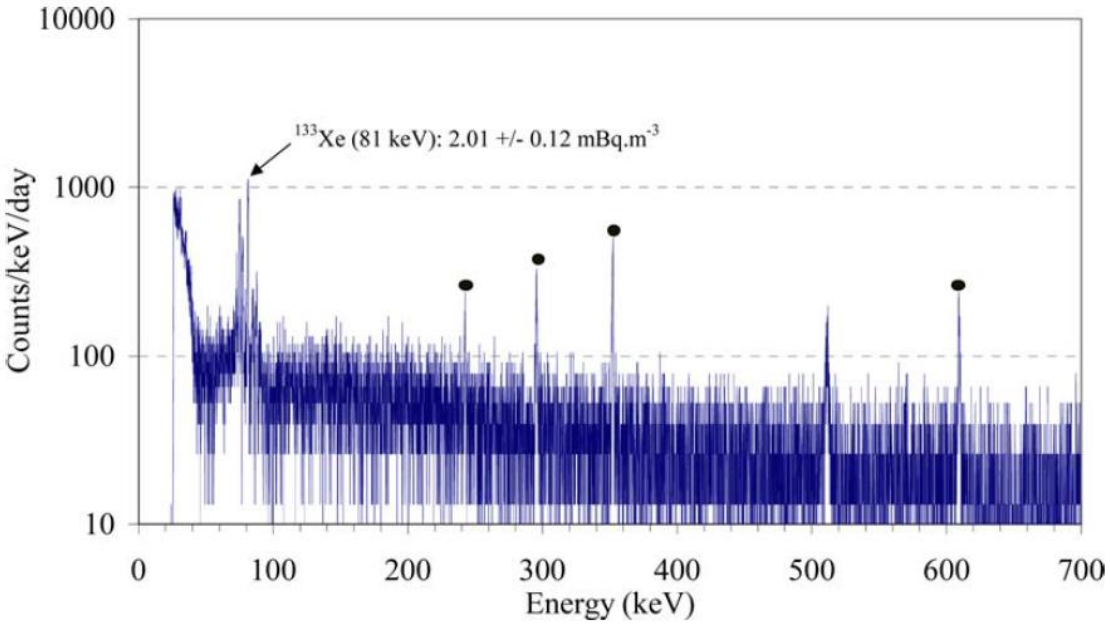

Figure 2-4. An example of gamma spectrum obtained by the SPALAX system in Marseille, France. ^{133}Xe is clearly detected during a 24-hour sampling cycle [43].

In SPALAX system due to the high sensitivity of the sampling and purification units, only radioxenons and small amount of radon enter the detection unit. Thus, the resulting spectrum is not very complicated and radioxenon identification can be easily done only by the limited number of possible peaks [43]. However, the detection of ^{131m}Xe and ^{133m}Xe is more challenging due to the low intensity of the gamma emissions from these radioxenons and also having the same X-ray peaks [3]. Therefore, the distinction between ^{131m}Xe and ^{133m}Xe is done based on the gamma activity measurement. To do so, gamma emissions from ^{133m}Xe that have higher intensity can be used for the quantification of ^{131m}Xe, using the information on the absence or

presence of ^{133m}Xe [3].

Another challenge with the SPALAX system is associated with the occurrence of background events in low energies in the region of interest which make the detection of the X-ray peaks in these regions sophisticated [50]. To deal with this problem Aatami software is used in the spectrum analysis. The main function of this software is to calculate the background baseline under a spectrum to be used in construction of the radioxenons spectrum [50].

Radioxenons of interests emit beta/conversion electrons in coincidence with gamma/X-rays. This feature can also be used to detect and distinguish radioxenons. Indeed, the beta-gamma coincidence measurement was found to be beneficial over the high resolution gamma spectroscopy. The reason is that the aforementioned background problem seen in the SPALAX system is not observed in the systems based on the beta-gamma coincidence method. Since these systems act like as a passive shield in addition to the other active shielding methods that are used. Therefore, the sensitivity of the system will be further increased. SAUNA, ARSA, and ARIX are among those installed detection system at IMS stations that use this technique for radioxenon measurement.

2.3.5.2 Automated Radioxenon Sampler and Analyzer (ARSA)

The ARSA radioxenon detection system was designed and developed at the Pacific Northwest National Lab (PNNL). It collects, purifies and measures all the radioxenons of interest. Collection and purification of xenon from air is performed using cooled, activated charcoal from 48 m^3 samples collected every 8 hours [4].

The ARSA system uses four beta cells surrounded by two NaI(Tl) crystals (Figure 2-5) to

distinguish radioxenons using the beta-gamma coincidence technique [4].

The beta cells are 1.2 mm thick hollow plastic cylinders (Bicron BC-404) with diameter of 1.25 cm and length of 5 cm. Two 5 inches by 8 inch NaI(Tl) planes are optically separated and configured such that face one another. Between these two planes four 3.175 cm diameter holes are located to hold the beta cells. [4]

To shield the background radiation, the entire detector assembly is placed inside a 2 inches thick lead shielding with 0.25 inches thick copper shielding as well. This active shieling plus beta-gamma coincidence technique and rejecting of coincidence beta and gamma-rays provide very good background suppression for this system [4].

The two independent NaI(Tl) crystals allow rejection of multiple scatter and background events; however gain matching the PMTs is also difficult and time consuming. Figure 2-5 shows schematic Diagram of the beta and gamma cells for the ARSA system and the entire assembly of this detection system enclosed in copper cave (5 mm thick) surrounded by 5 cm of lead shielding.

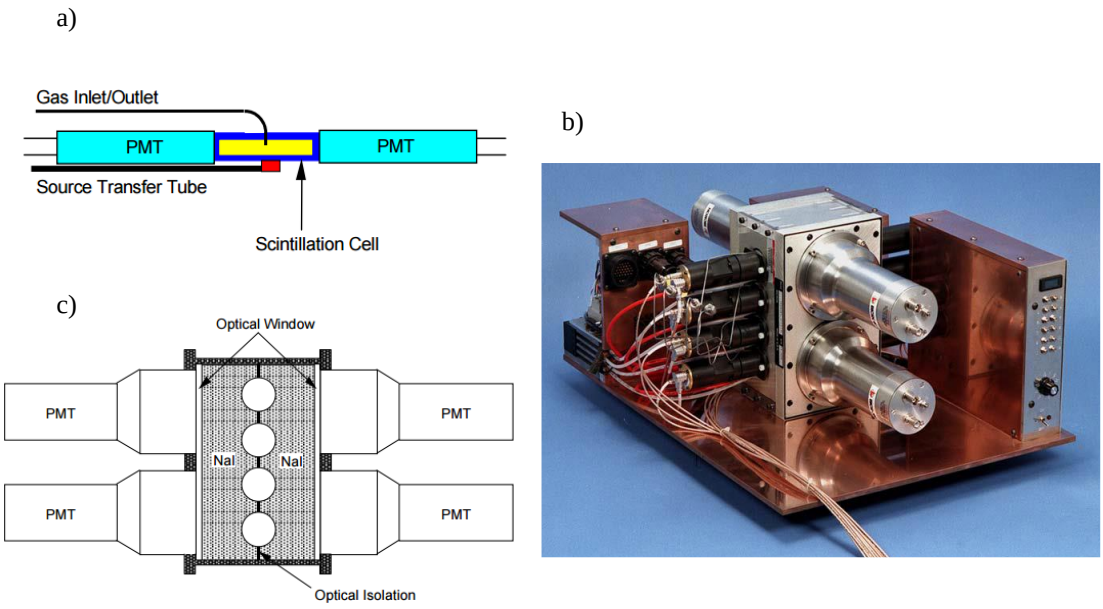

Figure 2-5. Schematic Diagram of beta and gamma cells for the ARSA system. a) Plastic scintillators beta cell with PMTs, gas transfer line and calibration source transfer. b) NaI(Tl) crystal with four holes where beta cells sit. c) The entire assembly of ARSA detection system enclosed in copper cave (5 mm thick) surrounded by 5 cm of lead shielding [51].

Electronic conditioning and readout for ARSA is done via standard NIM modules and a PNNL manufactured computer interface box.

For systems based on the beta-gamma coincidence technique usually a 2-Dimensional (2-D) beta-gamma spectrum is generated from coincidence events. Since each radioxenon has its unique signature, they occupy certain regions in this spectrum. Therefore, distinction between different radioxenons can be made. Figure 2-6 shows the two-dimensional spectrum obtained from ARSA detector. The boxed regions indicate the specific region for each radioxenon.

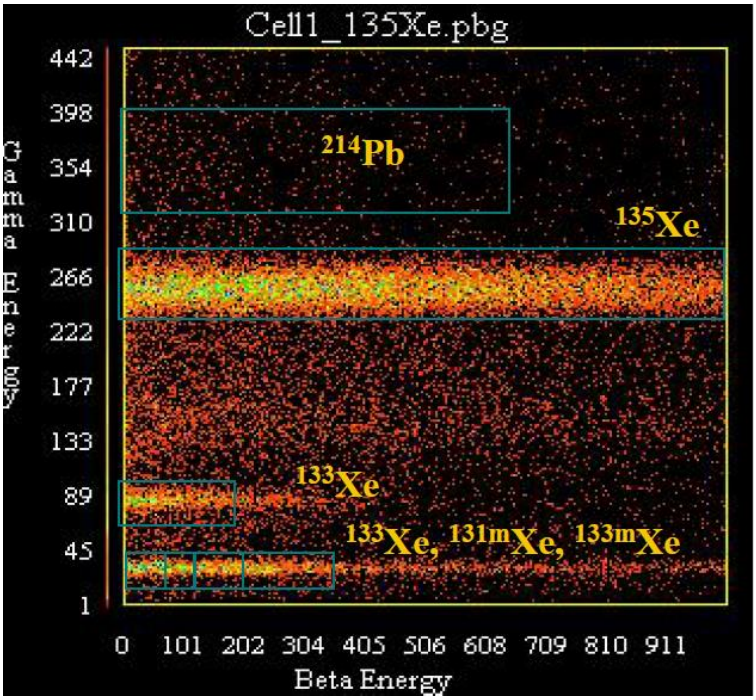

Figure 2-6. Two-dimensional beta-gamma coincidence spectrum obtained from ARSA detector [52].

2.3.5.3 The Swedish Automatic Unit for Noble gas Acquisition (SAUNA)

The SAUNA system was designed and developed by the Swedish defense research agency (FOI). Similar to the SPALAX system, this system also has 3 main units: sampling, processing and detection units as shown in Figure 2-7. However, unlike the SPALAX, this system is fully automatic, meaning that all sampling, processing and detection jobs are done automatically. This system samples air and extracts xenon present in the air, then xenon from the sampled air is purified, quantified, and the concentrations of the radioxenons are measured using a sensitive beta-gamma coincidence technique [5].

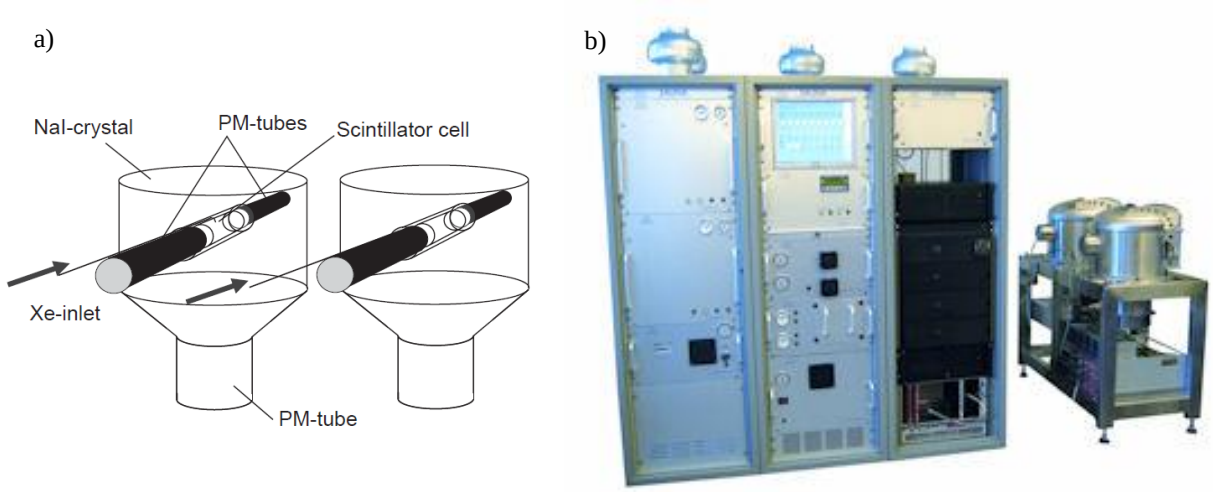

Figure 2-7. a) Schematic drawing of the SAUNA radioxenon detection system. The two identical detectors are placed inside a lead-cupper shielding [5]. b) Entire assembly of the SAUNA II detection system [53].

All radioxenon detections in this system are performed using scintillator materials. The detection unit of this system consists of four plastic scintillators (BC404) surrounded by two NaI(Tl) crystals in a 4π configuration. Plastic scintillators are responsible for both containing the xenon samples and also beta/conversion electron measurements. The total volume of the gas cell is 6.4 cm^3 with inner radius of 6.35 mm and a length of 50.8 mm. The thickness of this material was selected to fully stop 350 keV conversion electrons from ^{133}Xe (1mm). These plastic scintillators are viewed by two PMT's at each end [5].

Gamma/X-ray detectors (NaI(Tl)) have cylindrical shape with diameters of 4 in. and heights of 5 in. viewed by one PMT each and attached to a light guide as well. Beta detectors are placed inside a 35 mm hole at the middle of the NaI(Tl) crystals. The two identical detectors are placed inside a lead-copper shielding. The shielding consists of a set of 5-cm-thick bricks of low activity lead. A layer of 5-mm cupper shielding is placed inside the lead shielding as well to

remove 70 kev X-rays produced inside the lead shield by the ambient gamma ray radiation [5].

In this system processing the detector signals and data readout is done using standard CAMAC and NIM electronics. Coincidence measurements are also done by looking at the PMT's responses from the beta and gamma detectors. The time for the trigger signal is defined by one of the PMTs viewing the beta detector and when combined with the other beta detector's PMT forms the beta-coincidence signal. This coincidence signal is then delayed to be used for creating the third coincidence with the NaI(Tl) pulse [5].

The NaI(Tl) pulse height versus the summed pulse heights from the two beta detector PMTs will then be used to create a two-dimensional beta-gamma energy spectrum to identify the radioxenons of interests. An example of this spectrum for an injected sample containing both ^{133}Xe and ^{135}Xe is displayed in Figure 2-8 [5].

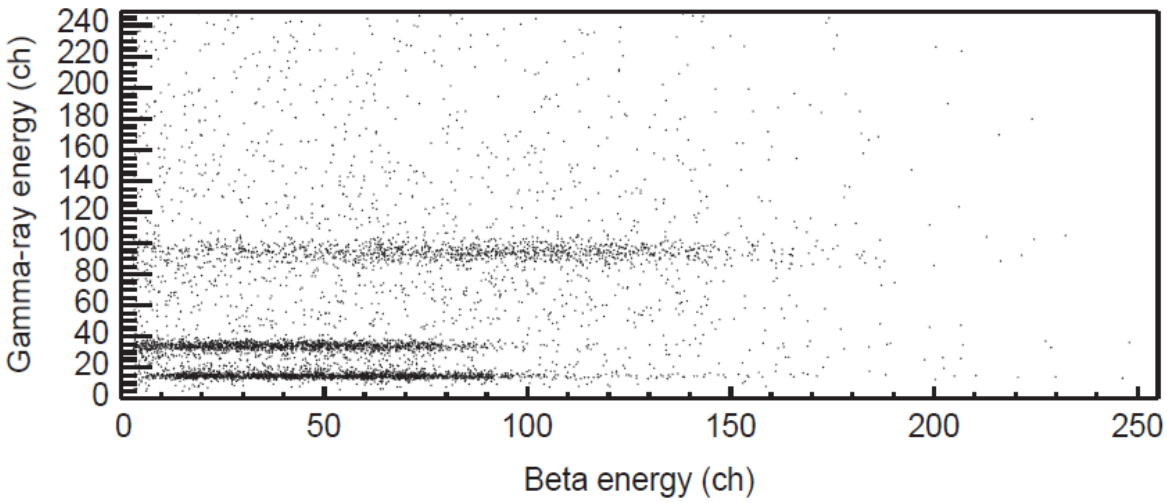

Figure 2-8. Two-dimensional beta-gamma coincidence spectrum for an injected sample containing both ^{133}Xe and ^{135}Xe from the SAUNA detector [5].

2.3.5.4 Automatic Radioanalyzer for Isotopic Xenon (ARIX)

The ARIX radioxenon detection system was developed at Khlopin Radium Institute, Russia. It automatically extracts xenon from air and has the capability of preparation of the samples, spectrometric analysis of the samples and activity measurement [6]. Figure 2-9 shows the general ARIX detection system.

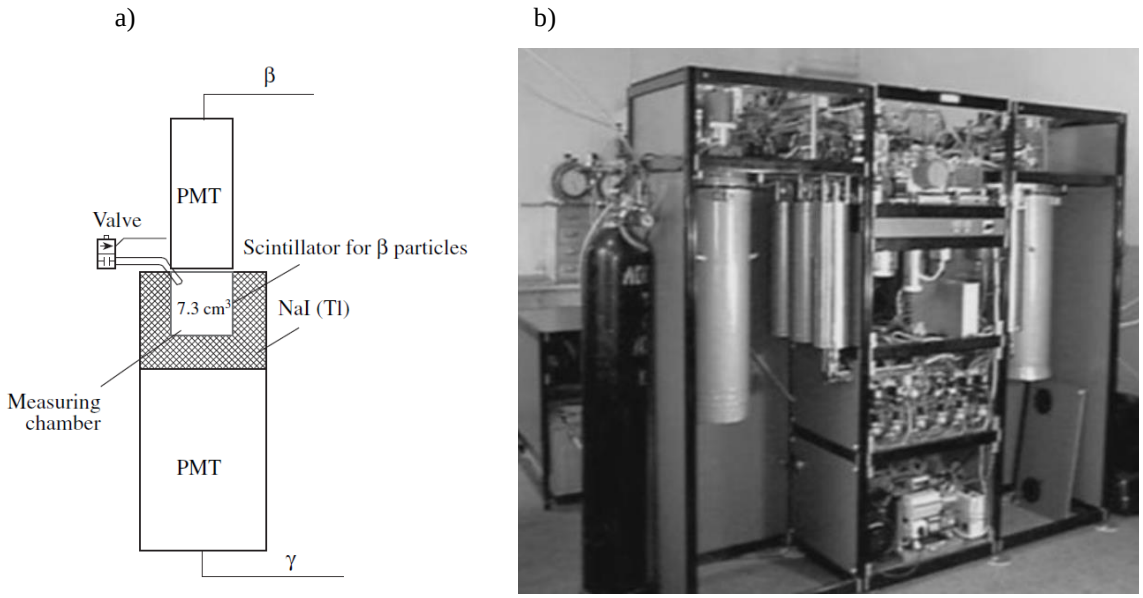

Figure 2-9. a) Schematic drawing of the detector unit of the ARIX radioxenon detection system. b) General ARIX detection system [44], [54].

Like ARSA and SAUNA detector, it also uses beta-gamma coincidence technique to detect radioxenons of interest. This system includes a radiation detector unit, a passive lead shielding, a reference radioactive source with a mechanism for its insertion and withdrawal and a 1024-channel pulse-height analyzer. Figure 2-9 (a) shows the schematic drawing of ARSA detection

unit. It deploys a well-type NaI crystal with outer diameter of 40 mm and height of 37 mm to detect gamma and X-rays. The crystal has also a well with diameter of 1mm and height of 28 mm. The volume of this well is 7.3 cm^3 [54]. Beta particles and conversion electrons are also detected using an organic scintillator (polystyrene) which has been coated inside the aluminum gas cell. The thickness of this scintillator layer is 0.1mm. The aluminum gas cell has the diameter of 17 mm and height of 27 mm which has been placed inside the NaI detector to maximize its efficiency for gamma and X-rays. Two PMTs are also used in this system to record the beta and gamma detectors signals in coincidence [54].

Figure 2-10 shows gamma ray spectrum from a xenon sample measured in beta-gamma coincidence mode with dominant peaks from ^{133}Xe and ^{135}Xe.

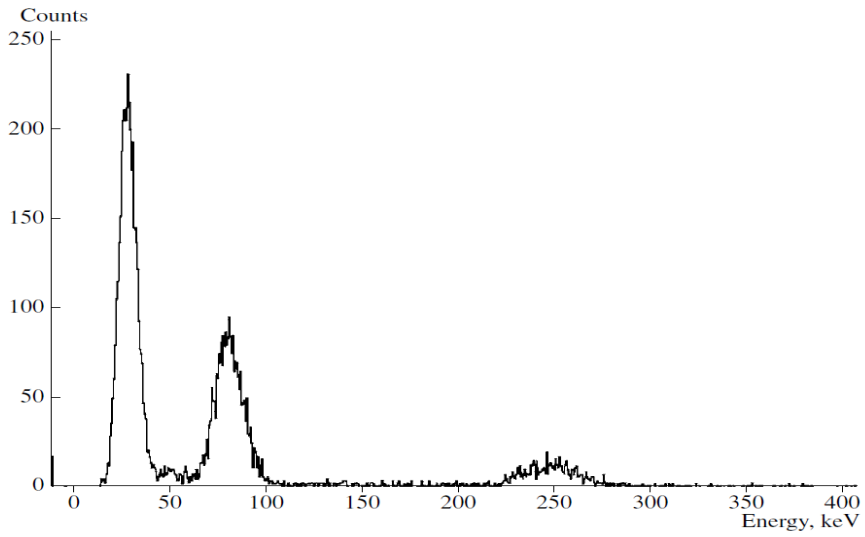

Figure 2-10. Gamma-ray spectrum of a xenon sample, measured in the β–γ coincidence mode for 10 h [44].

For detection systems to be installed at the IMS stations, power consumption and space limitations are major factors that should be considered. In ARSA, SAUNA and ARIX detection systems multiple PMTs are used to detect beta/conversion electrons and gamma/X-rays in separate scintillator materials. Therefore, gain matching and calibration of these systems is cumbersome. In addition, due to the use of several PMTs they consume more power, need large spaces and are more fragile which are drawbacks of these systems. These problems have been mitigated or eliminated by the use of a phoswich configuration. In phoswich radioxenon detection systems both beta and gamma detectors are viewed by a single PMT in a compact configuration and then pulse shape analysis techniques are used to detect beta-gamma coincidences. This approach greatly reduces the complexity of the system as only one single detector and readout channel are used.

2.3.5.5 PNNL Phoswich Radioxenon Detection System

The first phoswich radioxenon detection system was developed at PNNL. It uses a custom made 2x2 inch NaI(Tl) cylindrical crystal from Saint-Gobain [55] for detection of gamma/X-rays which has a 0.04-inch-thick window of calcium fluoride (CaF_2(Eu)) on one end to detect beta/conversion electrons. The thickness of CaF_2 (Eu) is large enough for beta/conversion electrons to deposit all of their energy inside CaF_2 (Eu).

The other end of NaI(Tl) is coupled to a PMT to read signals from both crystals with an integrating preamplifier to generate slow or fast rising pulses depending on which scintillator was triggered.

Pulses from NaI(Tl) and CaF_2 (Eu) have different rise time (250 ns rise time for NaI(Tl) vs.

940 ns for CaF_2 (Eu)) which makes pulse shape discrimination easier.

Pulse shape discrimination were done based on different pulse rise time, i.e.; the amount of time took the pulses reach from 10% to 90% of the maximum height and also with respect to the energy of different radixonons [56]. Figure 2-11 shows a 2-D spectrum from xenon pulses resulted using this pulse shape discrimination method. As can be seen the fast and slow rising pulses were separated into two distinct regions.

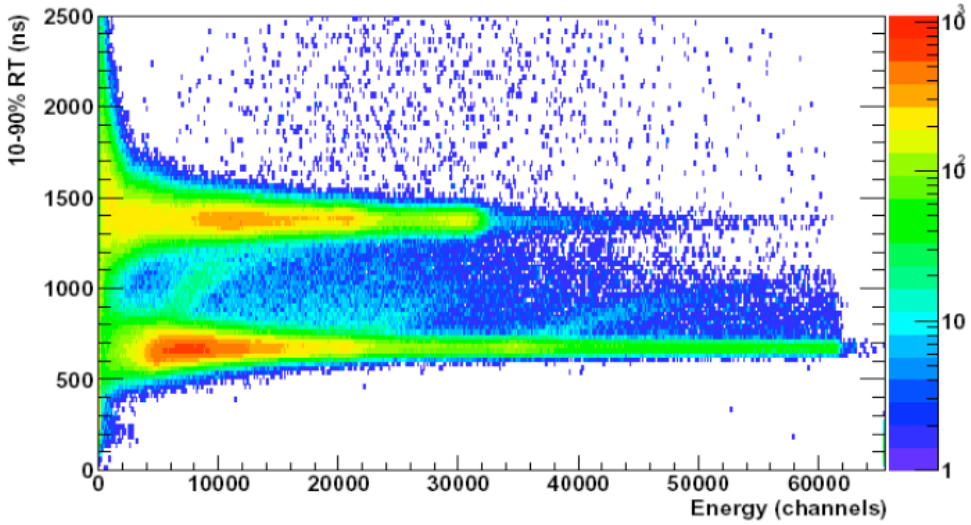

Figure 2-11. 2-D spectrum from xenon pulses resulted using this pulse shape discrimination method [57].

This detector was well-suited to distinguish interactions in any single part of the detector, however it wasn't able to easily identify interactions in both parts of the detector corresponding to the beta-gamma coincidences. Therefore, it was almost impossible to measure beta and gamma energies separately using this device.

In an effort to improve phoswich detection systems to be able to detect beta-gamma coincidences and measure energies accurately, XIA designed and developed a new phoswich

detector along with a different pulse shape analysis method.

2.3.5.6 Single Channel Beta-Gamma Coincidence Detection (Phoswach)

XIA developed a single channel beta-gamma coincidence detection system which (Figure 2-12) consists of a disk shape plastic scintillator (BC-404) with thickness of 1mm and diameter of 25.4 mm to absorb beta and conversion electrons. This scintillator is coupled to a cylindrical CsI (Tl) crystal with length of 25.4 mm to absorb mainly gamma and X-rays. Both crystals are viewed by a single PMT which is directly connected to a high-speed digital pulse processor (XIA DGF Pixie-4) [58]. In this device similar to the PNNL phoswich detector different time constant of the crystals is used to discriminate between beta pulses (very fast pulses) and gamma pulses (slow rising pulses) and also coincidence pulses which are combination of slow and fast pulses [58], [59].

Figure 2-12 shows different pulse shapes from phoswich detector acquired using a ^{60}Co source.

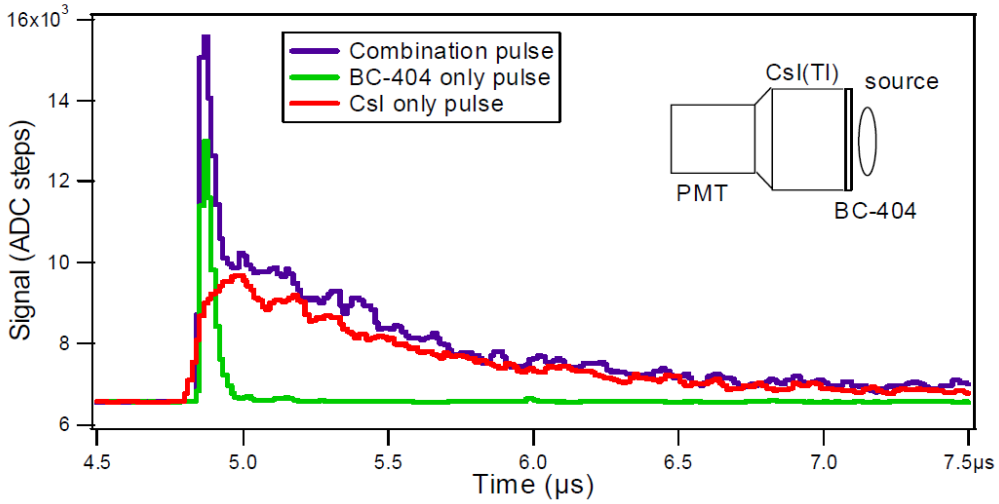

Figure 2-12. Different pulse shape from XIA phoswich detector using a ^{60}Co source [58].

A pulse shape discrimination algorithm is then used to separate combination pulses corresponding to the coincidence events from other event types and to find the energy deposited in each part of the detector.

Figure 2-13 shows 2-D energy scattered plot of ^{133}Xe where vertical and horizontal axis represent CsI only events and BC-404 only events, respectively.

In Pixie-4, total energy of each pulse is measured using a digital trapezoidal filter with a rise time of 7 μs, implemented in the Pixie-4 field programmable gate arrays.

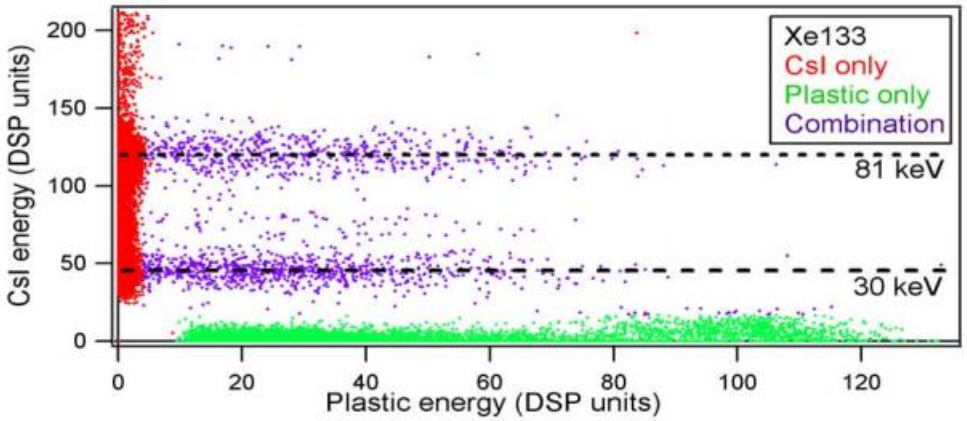

Figure 2-13. 2-D energy scattered plot of ^{133}Xe obtained using XIA phoswich detector. Plastic only, CsI only and combination events are clearly separated in this plot [58].

2.3.5.7 OSU two channel triple layer phoswich detector

OSU two channel triple layer phoswich detector consists of 3 layers (Figure 2-14). A thin hollow disk with thickness of 2 mm and diameter of 76.2 mm serves as the gas cell which houses 9.12 cm^3 of radioxenon samples. The gas cell is surrounded by two planar phoswich detectors

[60] . These phoswich detectors are identical and each has three scintillator layers with different decay times. The first layer (BC-400) with thickness of 1.5 mm is a low-Z material and appropriate to be used for beta and conversion electrons detection. The second layer (NaI) with thickness of 25.4 mm is a high-Z material to accommodate gamma and X-rays detection [60].

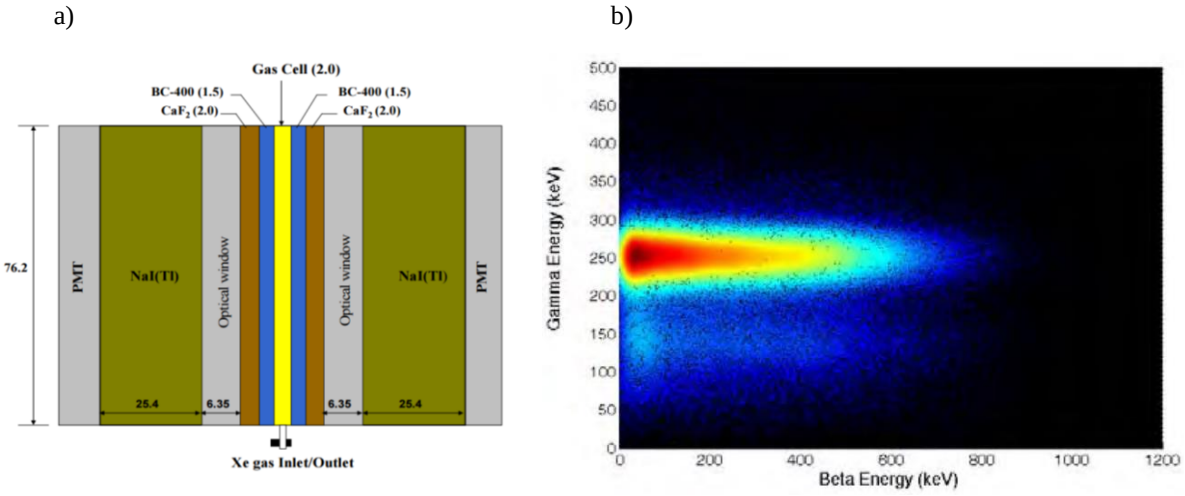

Figure 2-14. a) Schematic Diagram of triple-layer two-channel phoswich detector. All dimensions are in mm. b) the 2-D betta-gamma coincidence energy histogram of ^{135}Xe between the two phoswich detectors [61].

Since NaI is hygroscopic, it is isolated from the plastic layer by a layer of 6.35 mm quartz. However it is not suitable to detect 30 keV X-rays. Therefore a layer of CaF_2 with thickness of 2 mm is also placed between the BC-400 and quartz layers [60].

In this detector also different decay times of the scintillator layers are used to discriminate different events. A digital pulse shape analysis method based on how incident radiation releases energy in each scintillator layer is used for this purpose. In this method different pulses are

separated using digital trapezoidal filters to calculate fast and slow component ratios [62].

The 2-D beta-gamma coincidence energy histogram of ^{135}Xe between the two phoswich detectors is shown in Figure 2-14 b). 250 keV gamma ray line is clearly seen in this figure which is extended up to 900 keV.

2.3.5.8 Actively shielded Phoswich Detector (ASPD)

The second generation of OSU phoswich detector is an Actively Shielded Phoswich Detector (ASPD) which has the capability to suppress unwanted Compton scattering events and enhances the detector performance [63].

This detector consists of three scintillation layers, a cylindrical CsI (Tl) crystal with diameter of 56 mm to detect gamma and X-rays, BC-400 with diameter of 76 mm and thickness of 1.5 mm to detect beta and conversion electrons and a BGO crystal which has high density to detect scattering events also to shield CsI (Tl) crystal from the unwanted external backgrounds. The Gas cell of this system which is a cylinder with height of 2 mm and diameter of 76 mm is located at the top of the BC-400 crystal. BC-400 is also coated with a thin layer of aluminum to minimize the memory effect [64]. Schematic Diagram of this detector is depicted in Figure 2-15.

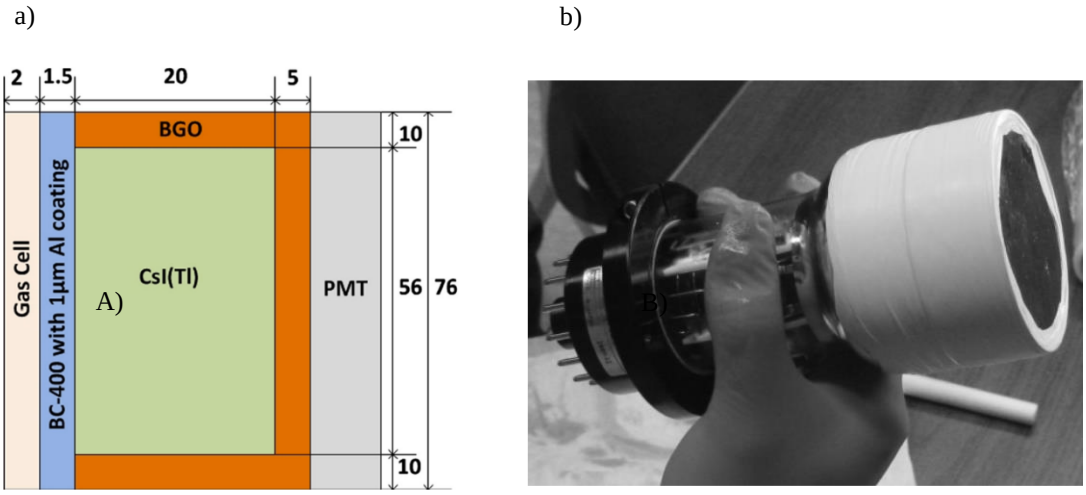

Figure 2-15. a) Schematic Diagram of the Actively Shielded Phoswich Detector (ASPD). All dimensions are in mm. b) The ASPD assembly wrapped with teflon tape [63], [64].

Anode pulses from this detector are processed using an FPGA-based digital pulse processor. Likewise of the first OSU phoswich detector coincidence events are detected using fast and slow component ratios [64]. Figure 2-16 shows 3-D beta-gamma coincidence energy histograms of ^{135}Xe obtained using this detector.

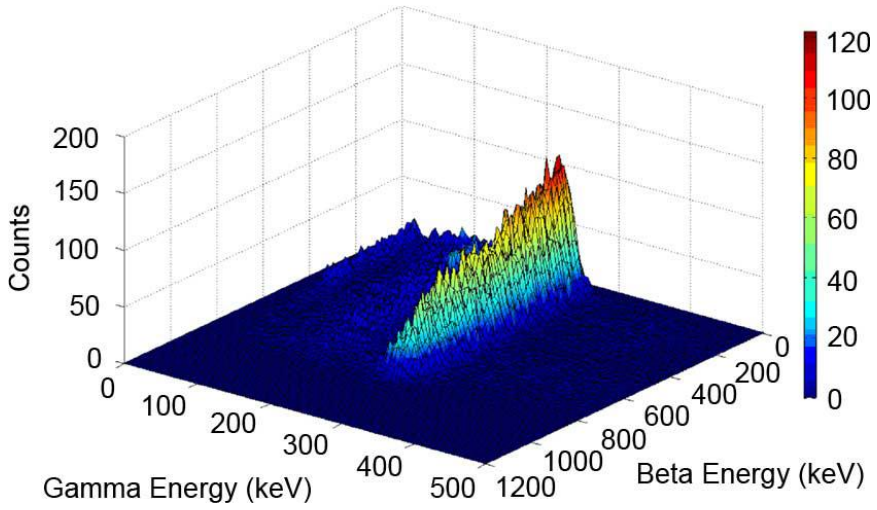

Figure 2-16. 3-D beta-gamma coincidence energy histograms from ^{135}Xe obtained using the ASPD detector [64].

The ASPD system showed pretty good performance in identifying radioxenons of interest; however the gas cell of this system has been placed at the top surface of the detector. Therefore, at least half of the radiation are lost without entering the active volume of the detector, reducing the detector efficiency and hence its sensitivity to radioxenon isotopes [34].

2.3.5.9 Well-type Actively Shielded Phoswich Detector (WASPD)

To compensate for the aforementioned problem, a new generation of phoswich detector called the well-type actively shielded phoswich detector (WASPD) was designed and developed at OSU. In this new design, the gas cell is located in a well in the detector, so gas samples are almost surrounded by the active detection volume resulting in a large solid angel for radiation detection. This geometry gives the WASPD better radioxenon detection efficiency compared to the planar design [34].

In the WASPD (Figure 2-17), a fast scintillator (BC-400) is used both as the gas cell to contain radioxenon samples and to detect beta particles and conversion electrons. It has an internal diameter of 15 mm and a wall thickness of 2.5 mm to absorb most beta particles and conversion electrons emitted from xenon radioisotopes. The BC-400 is surrounded by a layer of CSI(Tl) (decay time ~1,000 ns) with an internal diameter of 20 mm and wall thickness of 18 mm to detect gamma-rays and X-rays [34].

In order to have active shielding capability, the CSI(Tl) was enclosed by a layer of BGO (decay time ~300 ns). The BGO layer has an internal diameter of 56 mm and thickness of 10 mm. Having a high density (7.13 g/cm^3) and high efficiency, BGO is a good candidate to be used in Compton suppression systems [65], [66]. BGO identifies and rejects unwanted Compton

events in the CSI(Tl) scintillator and to reduce the Compton continuum in the CSI(Tl) gamma ray spectrum and hence improve the performance of the detector. In addition, the decay time of BGO (300 ns) is different enough from the other two scintillators (2.4 ns of BC-400 and ~1,000 ns of CSI(Tl)) to enable digital pulse-shape analysis algorithm to determine the origin of radiation interactions [34].

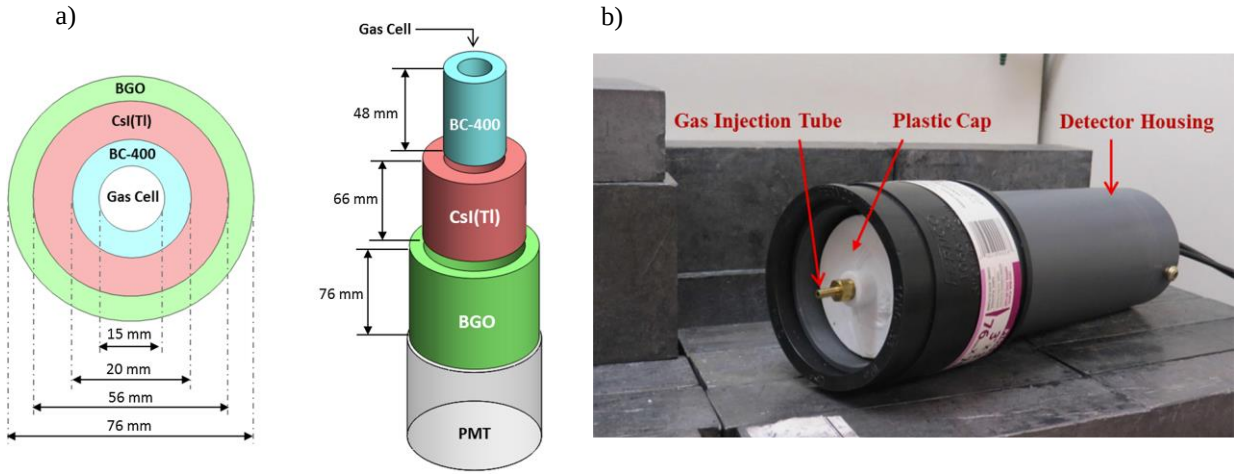

Figure 2-17. a) Schematic Diagram of the WASPD including PMT, BGO, CSI(Tl) and BC-400. b) WASPD final assembly showing the detector's housing, plastic cap and gas injection [34].

In this detector, a user-programmable 12-bit/200 MHz digital pulse processor (RX1200, Avicenna Instruments LLC) [67] was used to digitally process anode pulses from the phoswich detector. In addition, all digital processing functions including pulse-shape discrimination, beta-gamma coincidence detection, and energy histograms were implemented in an on-board FPGA device in real time. To discriminate between single and coincidence events and to measure the energy released in each scintillator layer, again the fast and slow component ratios were used [34]. Figure 2-18 shows 3-D beta-gamma coincidence energy spectrum from ^{135}Xe collected using CSI(Tl) + BC-400 coincidence events in real time.

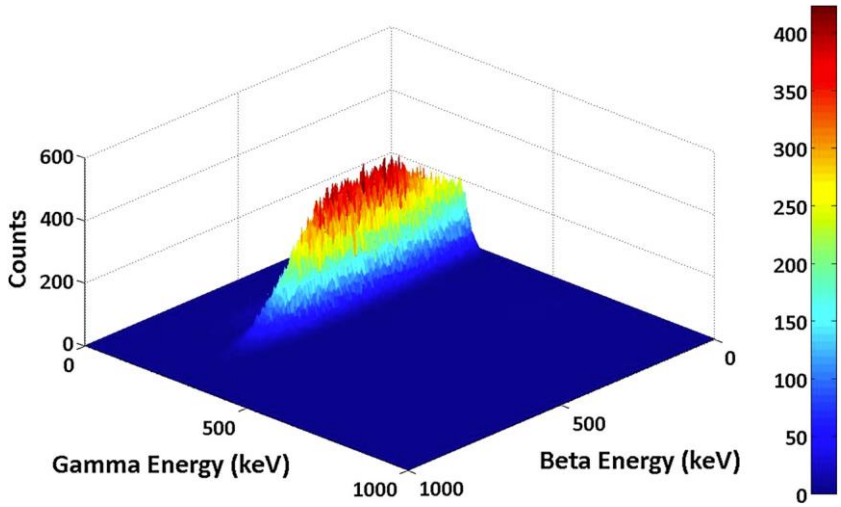

Figure 2-18. 3-D beta-gamma coincidence energy spectrum from ^{135}Xe collected using CSI(Tl) + BC-400 coincidence events in real time [34].

This system also has comparable MDC's with existing radioxenon detection systems as seen in Figure 2-19 and meets the IMS requirements for ^{133}Xe [34]. However, due to the use of plastic scintillators, this detector suffers from memory effect.

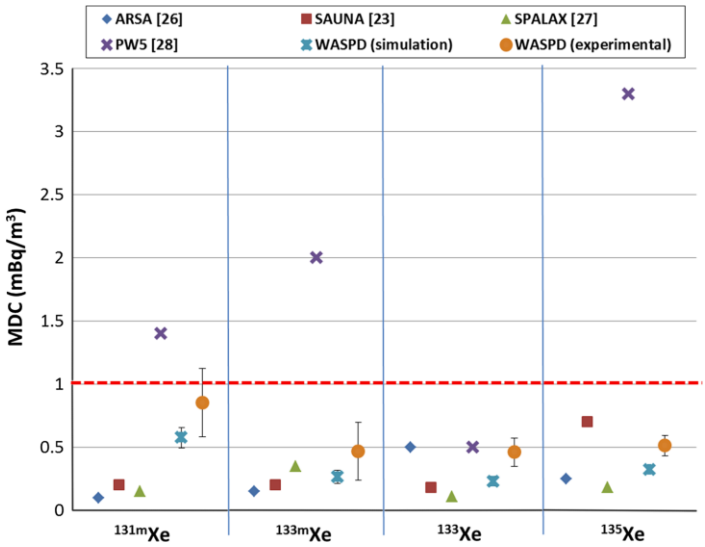

Figure 2-19. MDC comparison of WASPD detection system with other radioxenon detection systems: ARSA, SAUNA, SPALAX and PW5. The dashed red line shows the MDC requirement set by the International Monitoring System (IMS) for ^{133}Xe [34].

2.3.5.10 SPALAX NG new generation

New generation of the SPALAX system was developed by CEA in France. It consists of two face-to-face silicon detectors called PIPS™ (Passivated Implanted Planar Silicon) detectors from Canberra Semiconductor NV for beta/conversion electron measurements and a BEGe detector (from Canberra) for gamma/X-ray measurement [68]. The silicon detectors are part of a system called PIPSBOX (developed by CEA) made from ultrapure aluminum serve as the gas cell [68]. (Figure 2-20). The active volume of the gas cell is 11.7 cm^3. This new radioxenon detection system works in electron-photon coincidence mode.

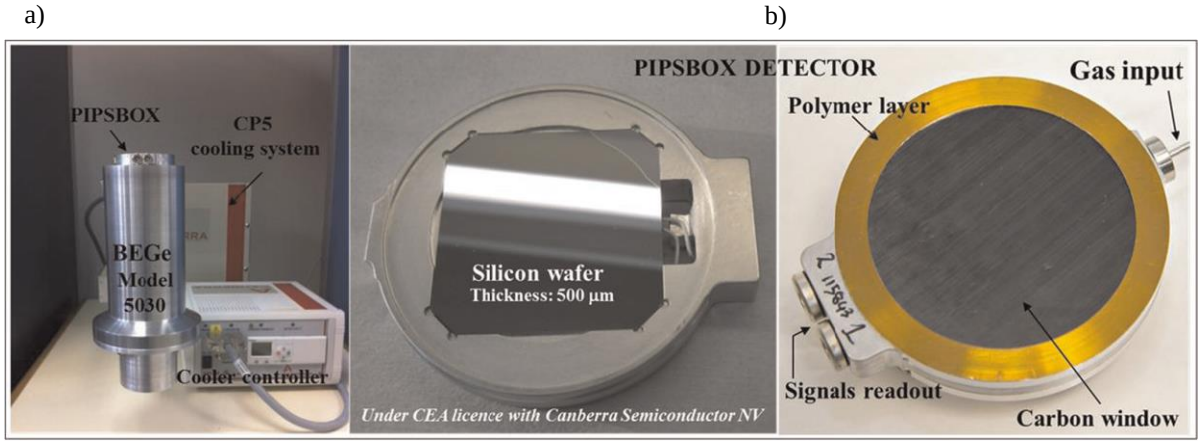

Figure 2-20. a) new generation of the SPALAX NG detection system without shielding. b) Gas cell of 11.7 cm^3 active volume equipped with two silicon detectors for electron detection and protected by a 600 µm carbon epoxy window entrance [68].

2.3.5.11 24-element Silicon PIN diode detector

This detection system was designed and developed at XIA using 24 silicon PIN diode detectors to measure both X-rays and conversion electrons emitted by radioxenons and uses coincidence gating the X-rays and conversion electrons to improve the detection sensitivity [45].

It consists of 4x25 mm^2 ceramic mounted PIN diodes on each of 6 sides of a cuboid gas cell made from copper. The active area of this detection system is 600 mm^2 [45].

Armstrong A12 epoxy is used to hold the diodes in place and also to make the vacuum sealing. The copper cuboid assembly and the preamplifiers are placed inside an airtight and light-tight Aluminum housing which is flushed with dry N_2 gas to stop water vapor condensation on the PIN diode outer surfaces when cooled [45].

Figure 2-21 shows various pictures of this detection system.

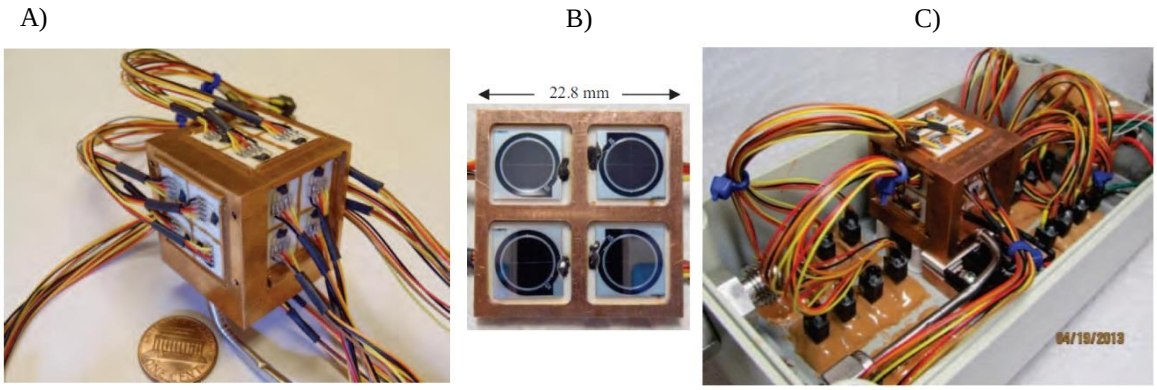

Figure 2-21. A) Outside view of the cuboid cupper. B) Window frame of 25 mm^2 PIN diodes mounted on ceramic holders. C) Detector cube inside the sealed box [45].

Coincidence between the PIN diode detectors is used to create 2-D spectrums and identify radioxenons. Figure 2-22 A) shows a 2-D coincidence plot from ^{127}Xe and ^{37}Ar. Each dot in this spectrum represents an event in any PIN diode which happened in coincidence with a second event in any other PIN diode [45]. Coincidence events between 30 keV X-ray conversion electrons at 112, 139, 170 and 198 keV, and also between the 139 and 170 keV events are clearly observable.

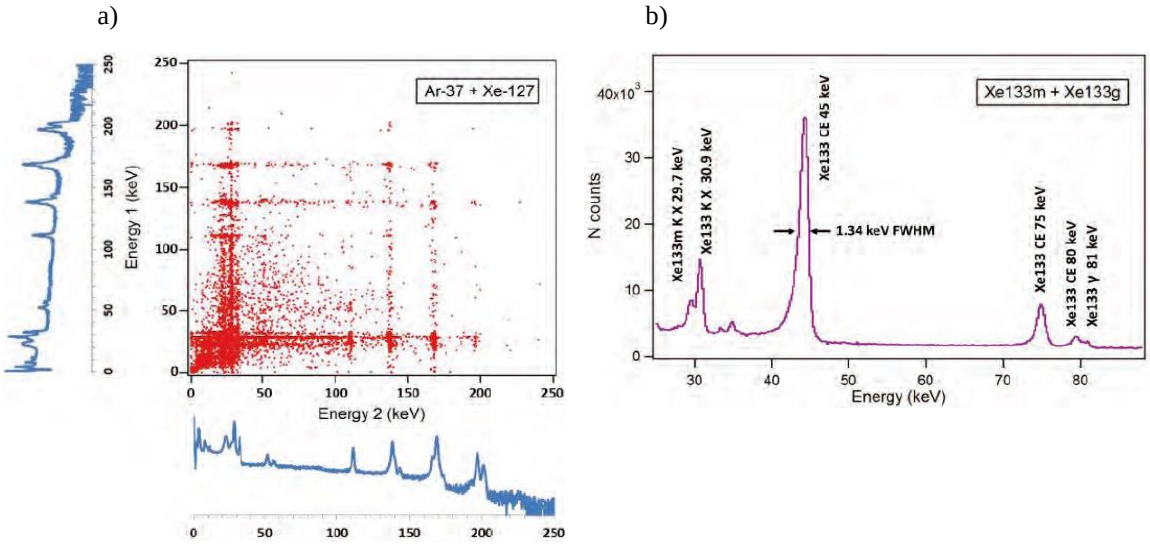

Figure 2-22. a) 2-D coincidence spectrum from a mixture sample of ^{127}Xe obtained using the 24-element silicon detector. (b) Spectrum from ^{133m}Xe and ^{133}Xe obtained using the 24-element silicon detector.

Figure 2-22 also shows the spectrum from a mixture of ^{133}Xe and ^{133m}Xe. Overlapping K X-ray lines around 30 keV, 45 keV conversion electrons and peaks around 80 keV are clearly visible [45]. Although, this detector has very good energy resolution to separate overlapping peaks, however from Figure 2-22 it can be seen that its efficiency for 81 keV is not remarkable. Therefore, this detection system is not well suited to detect radioxenons that emit higher gamma energies such as ^{133}Xe and ^{135}Xe.

2.3.5.12 Iranian Noble Gas Analyzing System (INGAS)

The Iranian Noble Gas Analyzing System (INGAS) utilizes a well-type NaI(Tl) scintillator to detect gamma and X-rays and a BC-400 plastic scintillator to detect beta and conversion electrons which also serves as the gas cell of the detection system. The NaI(Tl) crystal has a height and diameter of 76.2 mm. The depth and diameter of the well of NaI(Tl) are 52 mm and

25.4 mm, respectively. The internal walls of this well has been coated with 0.5 mm thick aluminum as well to mitigate the memory effect [69].

BC-400 which is 52 mm long and 2 mm thick, has an outer diameter of 20 mm. The active volume of this scintillator provides 9.24 cm^3 for the gas samples. The outer surfaces of BC-400 are wrapped with 5 layers of the teflon tape to increase the light collection efficiency, as well. The BC-400 is coupled to a PMT (XP3132) with a thin layer of silicon grease [69].

The whole detection system is shielded with 50 mm thick lead, while a layer of copper shield is also placed inside the lead shield to suppress induced X-rays. Figure 2-23 shows schematic drawing of the INGSAS and its shielding [69].

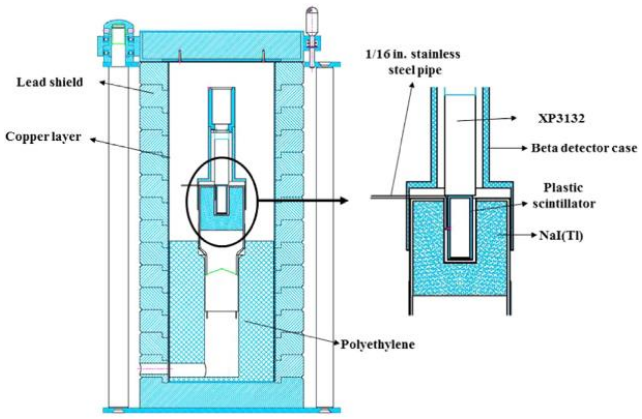

Figure 2-23. Schematic drawing of the INGAS detection system and its shielding [69].

This detection system works based on beta-gamma coincidence technique. Standard NIM modules are used to process pulses and detect coincidence events between the two detectors.

The INGAS detection system was tested by injection of ^{131m}Xe gases into the gas cell. Figure 2-24 shows 3D beta-gamma coincidence spectrum of ^{131m}Xe collected using INGAS. 129 keV conversion electrons in coincidence with 30 keV X-rays are clearly populated in this

spectrum. The minimum detectable activity of this detection system for ^{133}Xe is 1.24 mBq for 24 h measurement time [69] which doesn't meet IMS requirements.

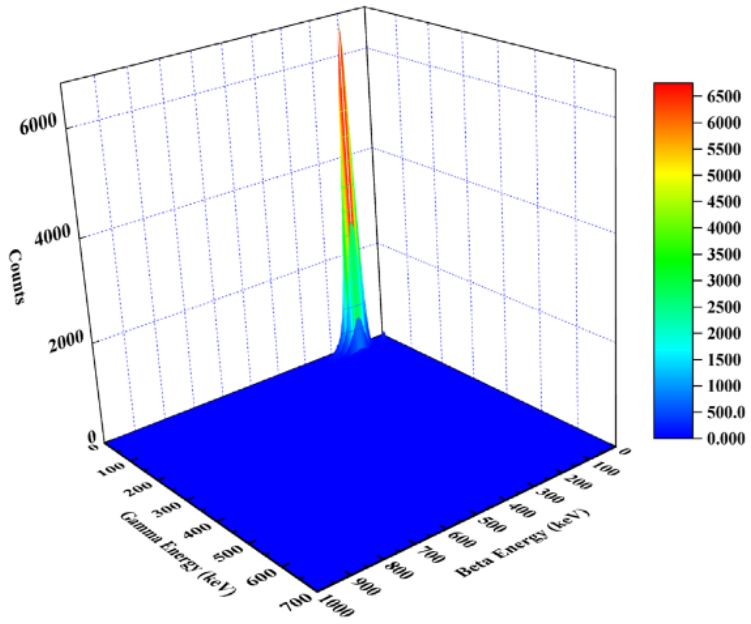

Figure 2-24. 3D beta-gamma coincidence spectrum of ^{131m}Xe collected using INGAS [69].

2.3.6 Coplanar Detectors in General

The coplanar grid technique was first introduced by P.N. Luke in 1994 [70] to address incomplete charge collection problems in CZT detectors. In this pattern (Figure 2-25 (a)), two sets of strips are interstitially connected together to form two grid electrodes known as collecting (CG) and non-collecting grids (NCG). By applying a slightly different bias voltage between these two grids, a strong electric field is generated near the anode surface. This electric field moves charge carriers (electrons and holes) toward the respective electrode. The electric field only affects the electrons when they are in close proximity to the anode. Moreover, movement of electrons in the detector will induce signals on both CG and NCGs, while the difference in voltage between the CG and NCGs pulls electrons toward the CG and pushes them away from

the NCGs [70]. Lastly, a net signal is obtained by subtracting the CG and NCG signals (Figure 2-25 (b)) which is only dependent of the movement of electrons. Therefore, the coplanar anode design almost completely eliminates the signal contribution from the slow-moving, more frequently trapped holes [70].

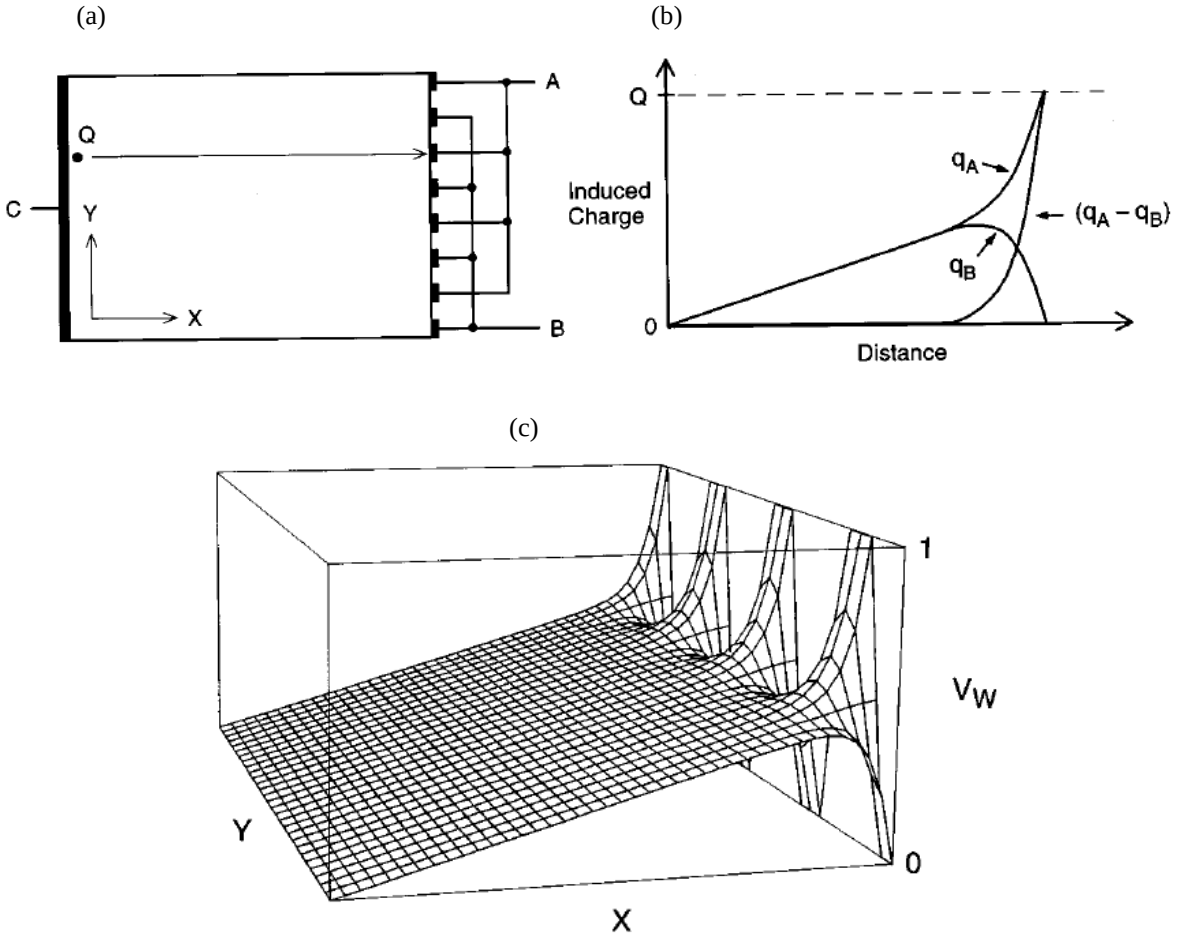

Figure 2-25. (a) Basic structure of the coplanar grids. (b) q_A, q_B and (q_A-q_B) induced charge at electrode A, induced charge at electrode B and the difference signal as a function of distance traveled by a charge Q which is ultimately collected at electrode A. (c) Weighting potential of one of the grid electrodes [70].

This induced signal in CG and NCG is a function of the weighting potential of each electrode.

The weighting potential (Figure 2-25 (c)) for a specific electrode is defined as the potential that would exist in the detector volume when the electrode of interest is set at unit potential, all other existing electrodes set at zero potential and no space charge exists [71]–[73].

2.3.7 Memory Effect

Three of the current radioxenon detection systems installed in IMS stations utilize plastic scintillators to detect beta/conversion electrons which is also serves as the xenon gas sample. One of the main drawbacks of these systems is that part of the xenon gas diffuses into the plastic during the measurement and stays there even after several evacuations. Therefore a residual activity is left behind which is referred to as the memory effect. This remained activity increases the background in the future measurements and interfere with these measurements. Thus, it enhances the minimum detectable concentration of these radioxenon detection systems and reduce the sensitivity of these devices. The memory effect is particularly noticeable at the IMS stations where strong radioxenon background sources such as medical isotope facilities or nuclear power plants is present [19], [74].

As mentioned in this chapter earlier, there are some issues with available radioxenon detection systems. Complexity is a major issue which affects ease of operation of some of the aforementioned detection systems.

Requiring regular maintenance due to the cryogenic cooling system in detectors that use HPGe, make these detection systems inappropriate for unattended application especially in IMS remote monitoring stations. They are also very expensive.

Memory effect is another issue that can be seen in detection systems with plastic

scintillators in their design. Memory effect degrades sensitivity of these detection system and enhances their MDC.

To address these issues and to find out whether CZT is a good candidate to be used for radioxenon detection or not, our new radioxenon detection system was designed and developed. Next chapter covers design and development of this detector.

What you seek is seeking you.
Rumi, 13th century Persian poet

3 Materials and Methods

3.1 Introduction

The main purpose of this work was making a prototype device for radioxenon detection and test whether CZT is a promising material to be used for radioxenon detection with reliable results. CZT was chosen for this purpose mainly due to its lower ionization energy compared to the conventional scintillation materials used in other radioxenon detection systems. Therefore, this detector possesses better energy resolution than the most available radioxenon detection systems.

Another advantage of this detection system is the absence of plastic scintillator which we anticipate to minimize the memory effect problem. There is also no need for cooling with liquid nitrogen for this detection system. Without the need for a cooling system, our detection system requires much less maintenance, a key feature for a remote-monitoring situation such as those at the various IMS stations.

Radioxenon detection system should also have less complicated electronics to avoid cumbersome work for its operation and maintenance. Using CZT helps to eliminate PMT's used in the available phoswich detectors and other radioxenon detection systems work based on multiple PMT's.

Our goal was to design and develop a small and compact radioxenon detection system. Therefore, it should have a minimal number of channels which reduces complexity, power and volume and we can still achieve very good energy resolution. To meet these requirements

coplanar pattern was chosen for our CZT detectors, since coplanar detectors do not need complicated electronics. This type of pattern was better suited to our needs as it also reduces the number of signals that must be processed from each CZT crystal. Using coplanar pattern each CZT generates only two signals that must be processed. Therefore, the electronics used in this detector is simple, decreasing the complexity of the system and its bulkiness. All these properties make the operation and maintenance of this detection system easier than available radioxenon detection systems.

This detection system possesses two CZT crystals for coincidence detection of gamma/X-rays and beta/conversion electrons. The general idea of coincidence detection in this system is detection of beta/conversion electrons in one CZT and detection of gamma/X-rays in another CZT or vice versa. All other possible events will be rejected for coincidence detection.

To test whether CZT is a good candidate to be used in radioxenon detection systems, two prototype devices were built and tested. The first prototype which possesses two 19.4x19.4x5 mm^3 CZT crystals failed and did not showed reliable results. Therefore, this design slightly changed to accommodate 10x10x10 mm^3 CZT crystals. With the second prototype trustworthy results were obtained for radioxenons of interest. In this chapter these two designs with their respective steps to finish the work will be introduced in more detailed.

3.1.1 Readout Electronics

3.1.1.1 Analogue Electronics

The readout electronics for our detection system is a combination of analog and digital components. The electronics required to implement coplanar technique for only one CZT

detector is shown in Figure 3-1. To integrate charges induced on the electrodes, the signals from CZT detectors need to be conditioned using a charge-sensitive preamplifier [75]. Thus, for each CZT two charge-sensitive preamplifiers are used to measure the induced signals from the two grid electrodes.

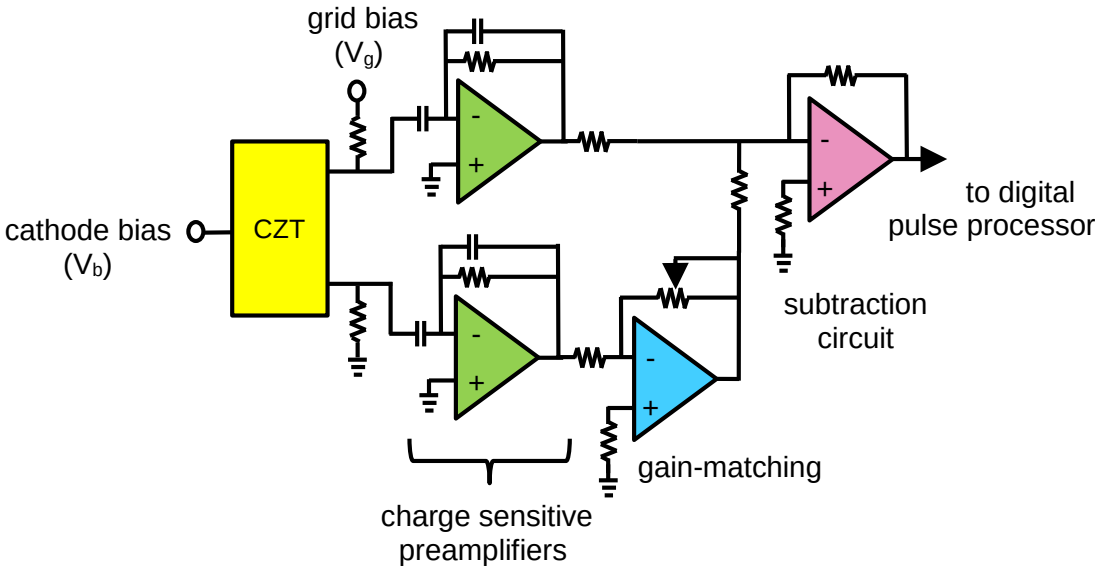

Figure 3-1. Block Diagram of electronics required for one coplanar CZT detector in the radioxenon detection system.

During operation, a high voltage (V_b) is applied to the cathode to sweep carriers across the detector, and a small voltage (Vg) is applied between the two grids to direct the electrons towards Collecting Grids (CGs) and away from the Non-Collecting Grids (NCGs). Since electron sensing is preferred in coplanar detectors a negative detector bias voltage will be used so that electrons move towards the coplanar anodes. Moving the electrons induces signal on both grids. Then the signals induced on these two grids by the movement of carriers are

subtracted to give a net output signal. This detector signal is mainly determined by the number of electrons reaching the collecting grid. Thus problem of poor hole's collection is mostly eliminated using coplanar technique.

Also a gain adjustment is provided to allow the relative gain of the two grid signals to be varied. By adjusting the relative gain of the two grid signals before subtraction, the effects of electron trapping can be almost compensated. Therefore, the net result becomes independent of the depths of interactions over much of the detector volume, and, therefore, excellent energy resolution can be obtained.

It should be highlighted that the output signal of each CZT is fed through an Analog to Digital Convertor (ADC) to digitize pulses from CZTs. This digital signal is then be passed to a Field-Programmable Gate-Array (FPGA) where coincidence events from the two detectors are identified and transferred to the PC for further digital processing.

3.1.1.2 Digital Pulse Processor and Digital Processing Techniques

A two-channel 250 MHz, FPGA-based Digital Pulse Processor (DPP 2.0) (Figure 3-2) developed in our lab was used to sample coincidence pulses from the two-channel analog preamplifier/subtraction circuit. Each channel of this pulse processor features a 12-bit, 250 MSPS ADC with LVDS output, digitally-adjustable offset and gain, a 3rd-order low-pass Bessel filter, and 4 diagnostic LEDs. Each of these channels feeds into the 1,500k gate-equivalent Xilinx Spartan 3 FPGA.

The FPGA is mounted on a commercial, off-the-shelf integration module. The FPGA is programmed via high-speed USB 2.0 connection to PC.

Though the DPP 2.0 was originally developed for use with a scintillator-based radioxenon detector, it was adapted for use with this CZT-based detector. This flexibility is made possible through the use of the on-board FPGA by changing the processing firmware.

The signal processing firmware developed for prototyping this CZT-based detector essentially consists of two waveform modules, one for each channel, and a coincidence detection module.

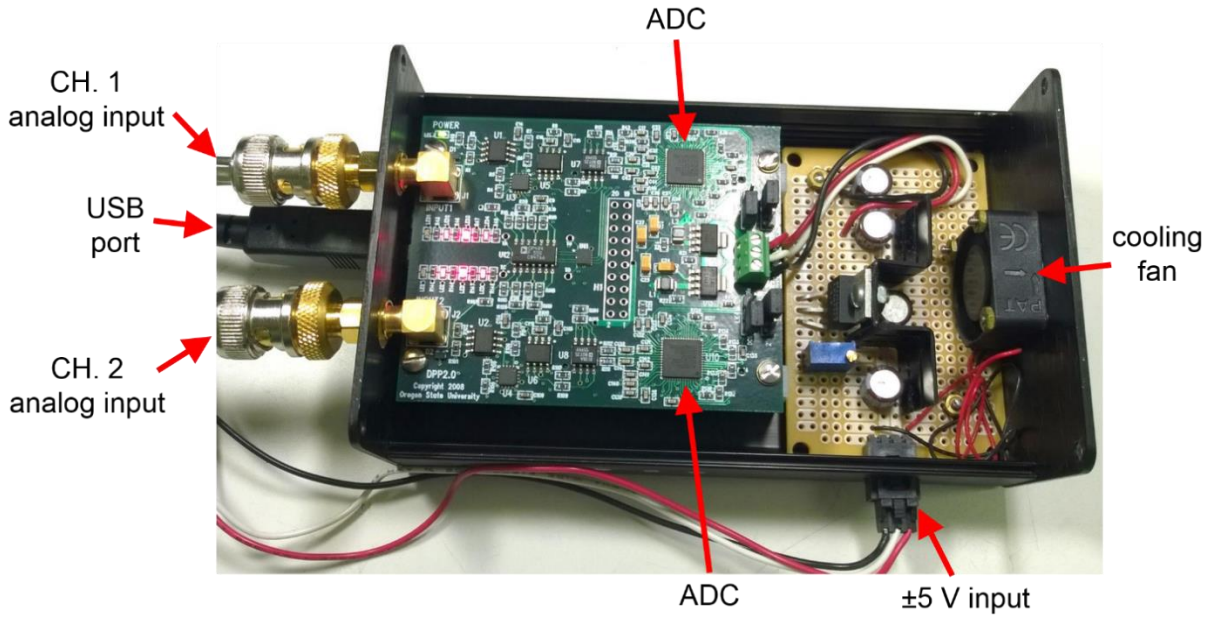

Figure 3-2. Two-channel 250 MHz, FPGA-based Digital Pulse Processor (DPP 2.0) developed in our lab.

The waveform modules each consist of a trigger module, pulse capture state machine, data transfer state machine, and a 4k dual-port block RAM, illustrated in

Figure 3-3.

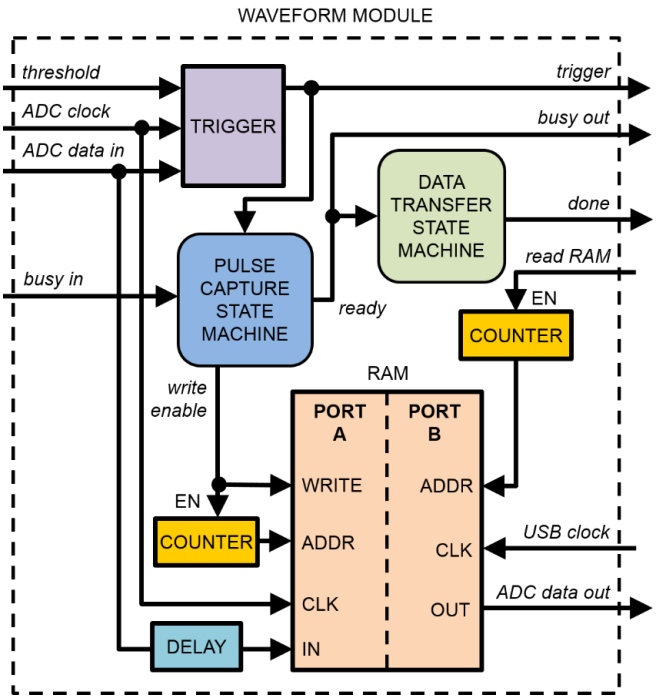

Figure 3-3. Diagram of the waveform module implemented in the FPGA.

To identify and capture coincidence events in real-time between the two channels, instead of using the time stamp method, a coincidence module was designed and added into the FPGA firmware. The coincidence module essentially consists of two identical state machines and an OR-gate, illustrated in

Figure 3-4.

When two channels are triggered in a predefined coincidence time window, those pulses are tagged as coincidence pulses (*coin* pulse indicated in

Figure 3-4 will go High), otherwise as singles.

Also for prototyping proposes and to have more flexibility in analyzing anode pulses from the two detectors, all the signal processing analysis are implemented in the PC side.

Thus valid pulses from each detector are captured in the digital processor, tagged as either coincidence or single and are uploaded to the PC via high-speed USB interface for further analysis.

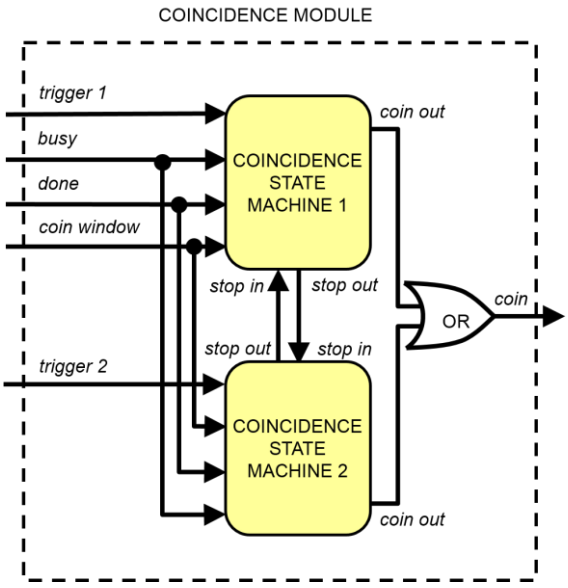

Figure 3-4. Diagram of the coincidence module implemented in the FPGA.

In high count rates, when the average time between two events is much less than the USB uploading time, most of the time one channel is waiting to be uploaded while the other channel is ready to be triggered and therefore small fraction of coincidence events can be practically captured. Obviously, this will reduce the efficiency of our digital processor in capturing coincidence pulses between the two detectors.

To improve the efficiency of capturing coincidence events, the coincidence state machine was designed to work in two modes: (1) Free-Running or (2) Synchronizing modes. In the Free-Running mode, both channels freely and independently can make a trigger for the system. In the Synchronizing mode, however, any channel can make a trigger when the other channel is ready to get triggered (e.g. not being in a wait state for uploading the pulse data to the PC).

In very low count rates, both modes perform similar functionality in terms of capturing coincidence events between the two detectors. In the Synchronizing mode, any free channel will wait until the other channel exits the wait state then is ready to get triggered, making both channels synchronized in capturing coincidence events.

To make a fast data interface between the DPP 2.0 and the MATLAB processing program, an USB interface module (Figure 3-5) was added to the FPGA firmware. The USB interface module is composed of three different types of endpoints: triggers, wires, and pipes. Triggers are one-shot binary pulses used for starting and stopping state machines. Wires carry set values that do not change often, and are used for user settings, such as the trigger threshold and run mode. Finally, pipes are used to transfer large sets of data, and used in the DPP 2.0 to transfer the 4k sampled ADC values from the FPGA to the PC. Each different trigger, wire, and pipe endpoint is selected based on its associated address and is pulled from the PC side of the interface. A MATLAB application program interface is used to set and receive trigger, wire, and pipe values from the FPGA firmware.

MATLAB interface can receive the anode pulses either in free running mode or in coincidence mode. For all of our measurements coincidence mode was used. In MATLAB,

coincidence pulses are captured and the user can check the condition of pulses and make necessary adjustments such as coincidence time window, offset level, amplification gain and threshold for each CZT detector by observing the associated pulses. After doing all adjustments, coincidence pulses are shaped using a trapezoidal filter, but before that the appropriate filter factors such as flat top and rise time are found. After shaping the pulses, the maximum value of the trapezoidal filter's output is picked and used for construction of deposited energy array of each CZT detector. These energy arrays are then used to generate the 2-D coincidence plot for each radioxenon. The MATLAB script used in this work can be found in Appendices.

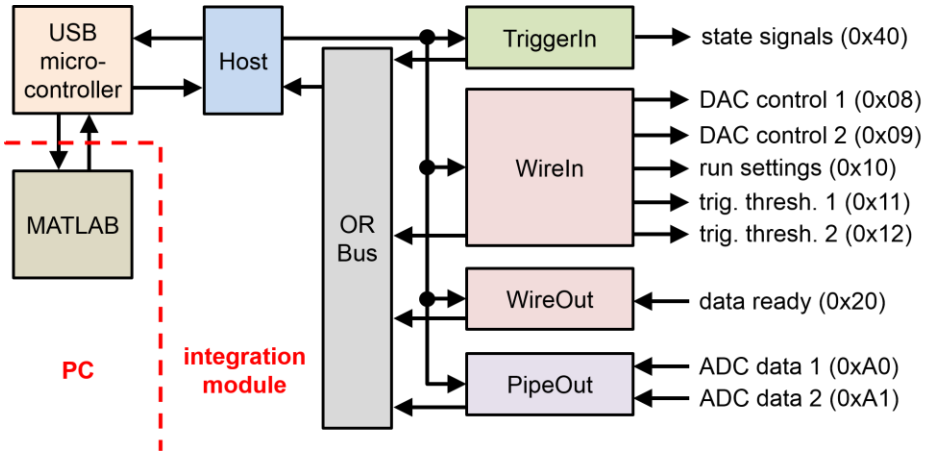

Figure 3-5. Diagram of the FPGA – PC communication interface.

This digital alongside with analog electronics discussed earlier, were used in our system to capture coincidence events from our device.

In the following section two detection systems will be introduced. The first one, is our first radioxenon detector prototype that we tried to make with our own coplanar pattern (designed

and simulated here at OSU) deposited on CZT crystals with dimension of 19.4x19.4x5 mm^3 which failed. And the second radioxenon detection system with pre-fabricated coplanar pattern on CZT crystals with dimension of 10x10x10 m^3 which worked as we expected.

3.2 Two-Element CZT Radioxenon Detection System (First Attempt)

This detection system possesses two 19.4x19.4x5 mm^3 coplanar CZT crystals. These crystals were mounted face-to-face at two opposite sides of a cubic gas cell while cathodes are facing each other (Figure 3-6).

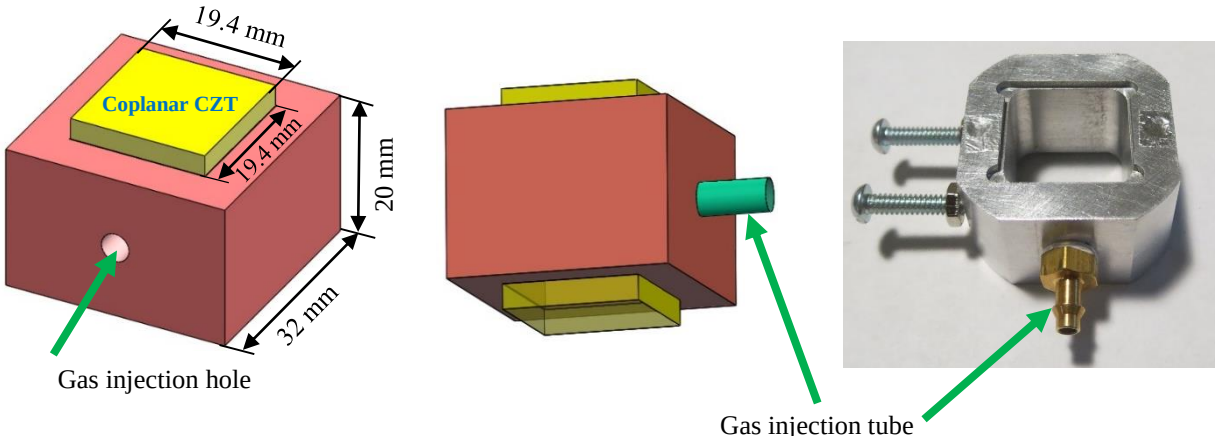

Figure 3-6 Gas cell of the first prototype two-element CZT radioxenon detection system.

19.4x19.4x5 mm^3 crystals generally are available only with pixelated patterns in the market. To use them as the coplanar detectors, a new pattern must be designed and adjusted to this dimensions. ANSYS Maxwell that uses finite element method to solve various static and time-varying problems [76] was found to be very powerful for this purpose. The designed coplanar pattern was then later deposited on the CZT crystals using the MASC facility [77] here at OSU.

Designing and assembling of this detection system includes several steps as the following:

1- Designing the coplanar patterns customized for 19.4x19.4x5 m^3 CZT crystals

2- CZT Substrate preparation for deposition

3- Deposition of the coplanar patterns on CZT crystals using the shadow mask

4- Designing and making the radioxenon gas cell

5- Readout electronics design

6- Test the detector with radioactive lab sources

3.2.1 Designing Coplanar Patterns Adjusted to 19.4x19.4x5 mm^3 CZT

The coplanar pattern was designed specifically for our CZT crystals using ANSYS Maxwell to achieve the most uniform response from these CZTs.

In coplanar detectors the induced signal is a function of the weighting potential of each electrode [70]. Therefore, by evaluating of the weighting potential one can evaluate the induced charges and hence the performance of the detector as it was done in this work.

To find the optimum pattern, the CG and NCGs weighting potentials were simulated based on the definition of weighting potential [71]–[73]. The CG's weighting potentials were simulated by assigning 1 V to the CG and 0 V to the NCGs and cathode. The weighting potentials were then found across the width of the detector along a line 1 mm below the anode surface and across the depth of the detector. For NCGs the same procedure was performed except that the CG and NCG's potentials were switched. Two things we were looking for, how closely the weighting potential of the grids matches each other (similarity) and how flat they are (uniformity).

Over 60 different designs were simulated for this purpose. The width of the grids, the

distance between grids and the distance between the grids and edges of the crystal were all varied between designs. The nine most promising designs were quantitatively evaluated based on the uniformity and similarity of the weighting potentials of the CG and NCG.

Uniformity is a measure of the degree to which the weighting potential for each grid maintains a constant value across the detector width. The uniformity value, *U*, was calculated individually for the collecting and non-collecting grids of each anode design according to Equation 1:

$$U = \sum_i \left(w_i - w_m \right) \qquad (1)$$

where w_i is the weighting potential at location i across the width of the detector and w_m is the weighting potential at the middle of the detector.

Similarity is a measure of the degree to which the weighting potentials of the collecting and non-collecting grids are equal across the width of the detector, 1 mm below the anode surface. The similarity value, *S*, was calculated once for each anode design using Equation 2:

$$S = \sum \left| w_{cg,i} - w_{ncg,i} \right| \qquad (2)$$

where $w_{cg,i}$ is the weighting potential of the collecting grid at location *i* across the width of the detector and $w_{ncg,i}$ is the weighting potential of the non-collecting grid at location *i* across the width of the detector.

The uniformity and similarity values of each anode design were then normalized to the largest of each respective value among all nine designs, and added together to calculate the figure of merit (FOM) for each design (Equation 3), with a lower FOM corresponding to a better design.

$$FOM_{design} = U_{design} + S_{design} \qquad (3)$$

Figure 3-7 shows the calculated FOM for selected designs using this approach.

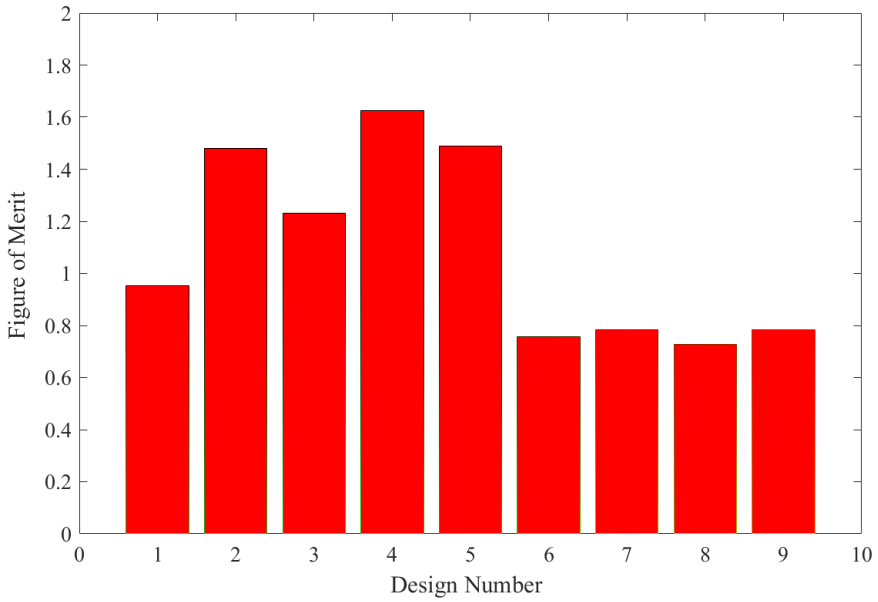

Figure 3-7. FOM of the best coplanar patterns designed using ANSYS Maxwell. Amongst them, design with lowest FOM was chosen for manufacturing.

Amongst these nine designs, design no. 8 has the lowest FOM and thus was chosen for manufacturing (Figure 3-8). Simulated CG and NCGs weighting potentials across the width and depth of the CZT are shown in Figure 3-9.

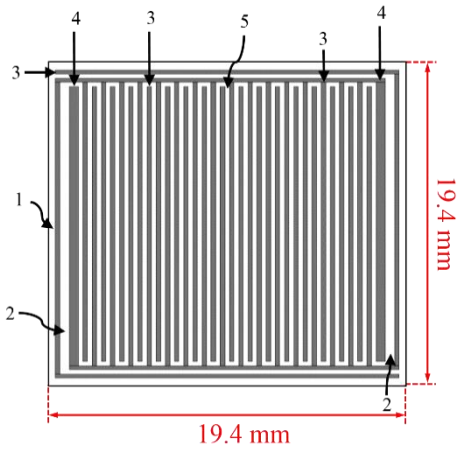

Figure 3-8. Anode pattern chosen for fabrication. Gap between anode and crystal edge (1): 0.325mm; gap between boundary grid edges (2): 0.51mm; grid width (3): 0.23 mm; boundary edge width (4): 0.5 mm; gap between grids (5): 0.27mm.

As illustrated in Figure 3-9(a) the weighting potentials across the width of the detector are almost uniform at the entire CZT volume except at the regions close to the edges of the CZT. Similarity of both CG and NCGs is clearly visible in this figure as well. In addition shape of CG, NCG and subtracted weighting potentials across the depth of the detector are as we expected to be for coplanar detectors Figure 3-9 (b). CG and NCG's weighting potentials have almost the same value except at a region which is very close to the anode (near grid region). At this point CG's weighting potential reaches maximum value (which is 1) whilst NCG's weighting potential drops to zero as we expected. This gives rise to a net (subtracted) signal which is zero almost at the entire detector volume and suddenly increases at the regions which is very close to the grids.

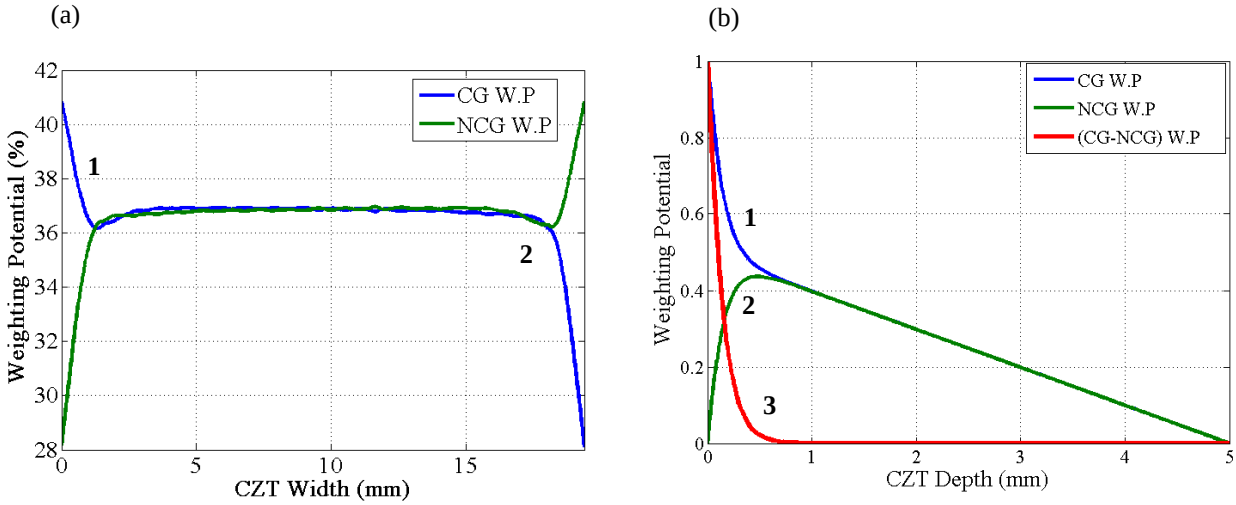

Figure 3-9. Simulated weighting potentials of the collecting grid (1), non-collecting grid (2), and their subtraction (3) across (a) the width of the detector and (b) the depth of the detector for the best design.

It should be mentioned that minimizing the near grid region was one of our considerations for designing coplanar patterns, since the smaller this region the better energy resolution can be achieved.

Although, our simulation showed that having a minimum distance between each grid in the coplanar pattern has a great influence on the uniformity and similarity of the weighting potentials as well as minimizing the near grid region and hence performance of the detector, but because of the manufacturing limitations the width of each grid was adjusted to be 0.23 mm and the distance between them was kept to be 0.27 mm.

3.2.2 Electrode Deposition

Coplanar electrode deposition was done in VEECO thermal evaporator chamber at Oregon State University MASC clean room [77] using a metal shadow mask (Figure 3-10) .

Au was preferred to be used as the conductive material. However, since Au is not adhesive enough in contact with semiconductor materials a two-step method was used to increase the adhesion strength of Au to the CZT. This method also reduces the inhomogeneity of the metal/semiconductor interface, which is very useful to improve the detector performance [78]. In this method first a thin layer of chromium (250 nm) was deposited on the CZT surface and then the Au layer (90 nm) was deposited on the top of the chromium layer.

The final result is shown in Figure 3-11. As can be seen the coplanar electrodes are deposited on the CZT surface uniformly as we expected.

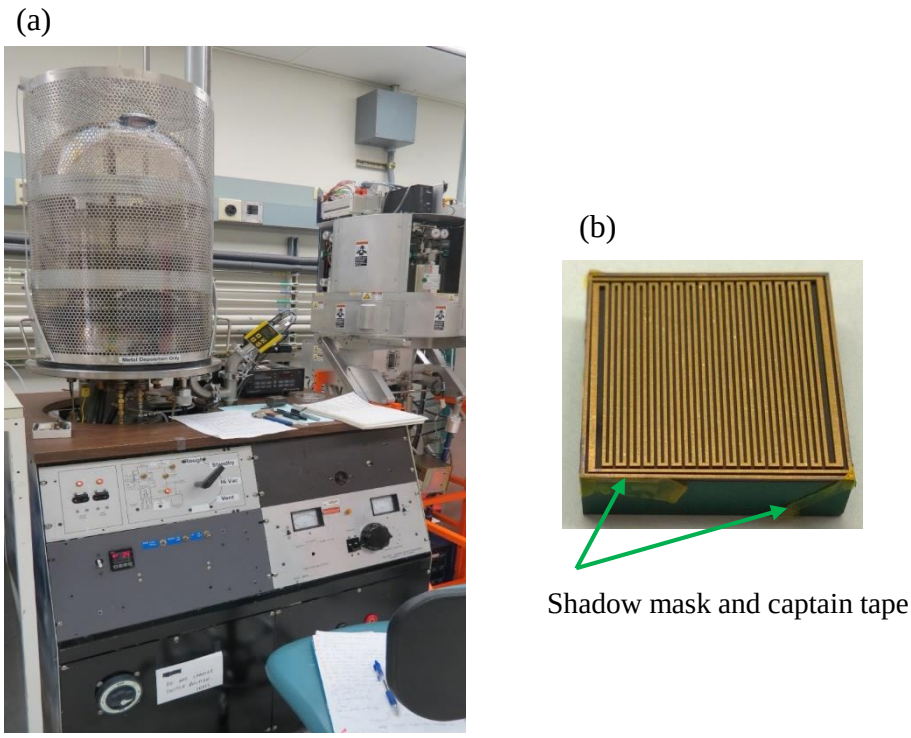

Figure 3-10. (a) VECCO thermal evaporator used for coplanar electrodes deposition on CZT crystals. (b) Shadow mask+CZT crystal ready for deposition

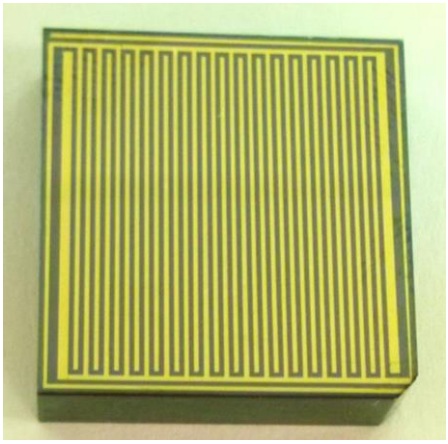

Figure 3-11. Coplanar patterns deposited on the CZT crystal.

After checking the electrodes an optical microscope was used to make sure that there are no physical defects in the deposited electrodes. Then a multi-meter was used to check the resistivity at different spots on the electrodes to make sure that there is no problem with electrodes connections. Two CZT crystals were patterned using this method and were mounted on two sides of the gas cell and were tested.

3.2.3 First Radioxenon Detection System Assembly

The first two-element detector prototype, including two 19.4x19.4x5mm^3 coplanar CZT crystals, gas cell, preamplifiers, and subtraction circuit, was assembled inside an EMI shielding box. The two coplanar CZT crystals were mounted face-to-face on either side of the custom-made 7.5 cm^3 aluminum gas cell (Figure 3-12).

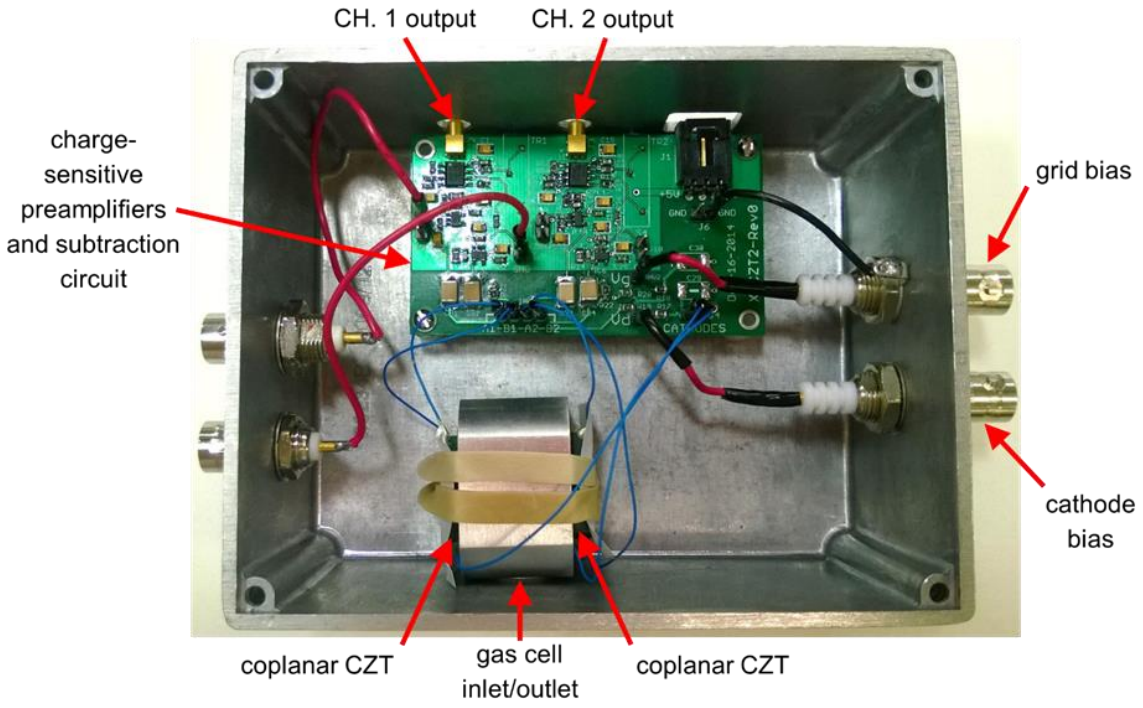

Figure 3-12. A top view from our first two-element CZT-based radioxenon detector prototype.

3.2.4 Testing and Troubleshooting of the Detection System

After the assembly, radioactive lab sources were used to test and troubleshoot the detector. CG, NCG and subtracted signals from each CZT crystal were checked for this purpose.

For this purpose, the outputs of CG, NCGs and subtraction circuit were connected to the oscilloscope separately. No detectable signal was identified from the CZT crystals on the first try. The preamplifier/subtraction PCB was tested using a digital oscilloscope and a pulse generator. The preamplifier/subtraction circuitry was found to be working as expected. When no issues with the analog electronics were found, the CZT crystals were then inspected carefully. It was determined that there were some disconnections/interruptions in the coplanar electrodes.

It was believed that the reason for this problem was the weak adhesion of the gold electrodes

to the CZT crystals, and that some gold separated from the CZT crystals by handling, shaking, or other mechanisms. Figure 3-13 shows spots where the deposited gold pattern is interrupted on one of the CZT crystals.

Figure 3-13. Interrupted strips were found in the deposited gold electrodes on the CZT crystal.

Photolithography was investigated as a means of solving this problem since it would increase the precision of the electrode deposition by eliminating the metal shadow mask used in previous depositions. However, our CZT crystal did not fit to the photolithography microscope to align the mask and the crystal. Instead, the thermal evaporation of chromium and gold was repeated, but using 250 nm of gold instead of 90 nm, an attempt to obtain better adhesion on the crystal. The first step in re-deposition was to remove the previously deposited gold layer. This was accomplished by first using a 5 μm particulate aluminum slurry (Figure 3-14). The crystals were then placed in a 2% bromine-methanol solution for 2 minutes (Figure 3-15) to decrease the roughness of the crystals surfaces and therefore reduce the leakage current [79].

(a)

(b)

Figure 3-14. (a) Aluminum slurry used to remove existing coplanar pattern and to smooth the CZT anode surface. (b) CZT surface after polishing with aluminum slurry.

(a)

(b)

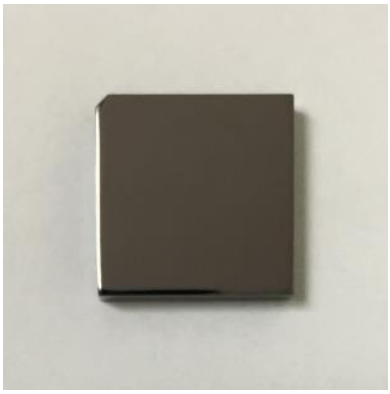

Figure 3-15. (a) CZT anode submerged in a 2% bromine-methanol solution for 2 minutes. (b) CZT anode surface after bromine-methanol treatment.

It should be mentioned that since bromine is an extremely dangerous and toxic chemical material, bromine-methanol treatment was done inside a fume hood. After the treatment CZT crystals were also washed using acetone, IPA, and DI water as mentioned in previous sections so that all the bromide is removed before the crystals are used in other deposition processes.

The CZT crystals with re-deposited electrodes were mounted face-to-face on either side of the aluminum gas cell.

Using these new patterns this time we were able to detect signals from each CZT crystal. The optimal operating settings for the cathode bias, grid bias and gain-matching were then determined by observing the shape of the CG and NCG's signals. The optimal shape of these signals occurs when the subtracted signal rise time is at a minimum.

Figure 3-16 shows the CG, NCG and subtracted signals from one of the coplanar CZT detectors with optimal biasing and gain-matching settings. As can be seen, the CG, NCG and subtracted signals behave as we expect for the coplanar detectors. The electronically subtracted signal functionality was verified by comparing it to the mathematical subtraction of the CG and NCG's signals. These signals were well identically matched, verifying the proper functionality of the preamplifier/subtraction circuitry.

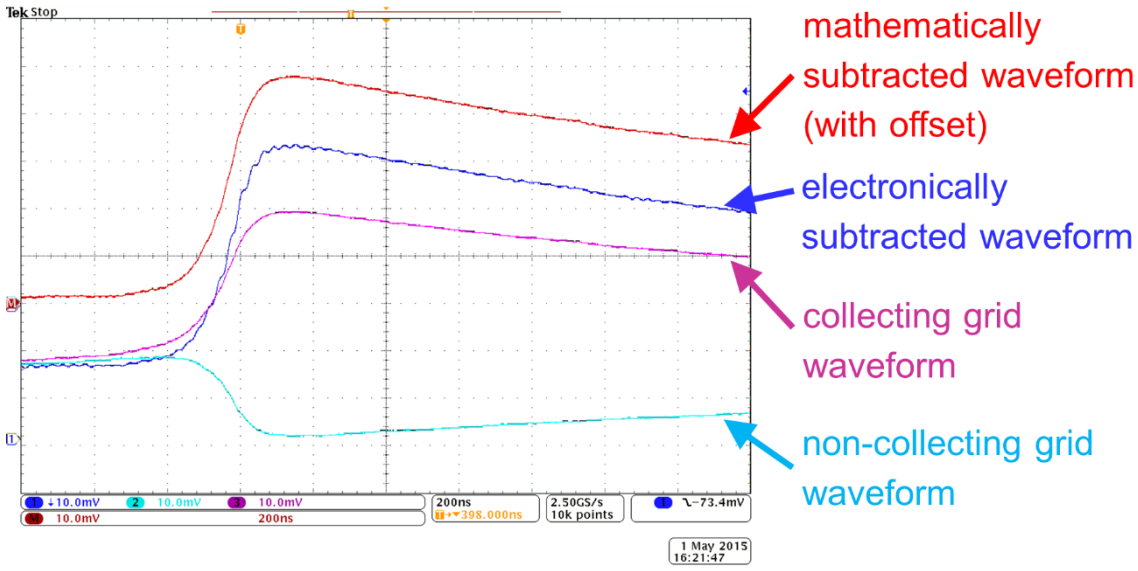

Figure 3-16. Signals extracted from one of the CZT crystals after gain matching.

Some troubleshooting was performed on the analog electronics to reduce the amount of noise observed in the signals. An issue with the power supply ground was identified and corrected.

To generate an energy histogram from our detectors, an offline histogram generation algorithm was developed in MATLAB using trapezoidal shaping.

Digitized waveforms and trapezoidal outputs from the two CZT crystals is shown in Figure 3-17. The response of this filter was then sampled to generate the histogram for each CZT crystal.

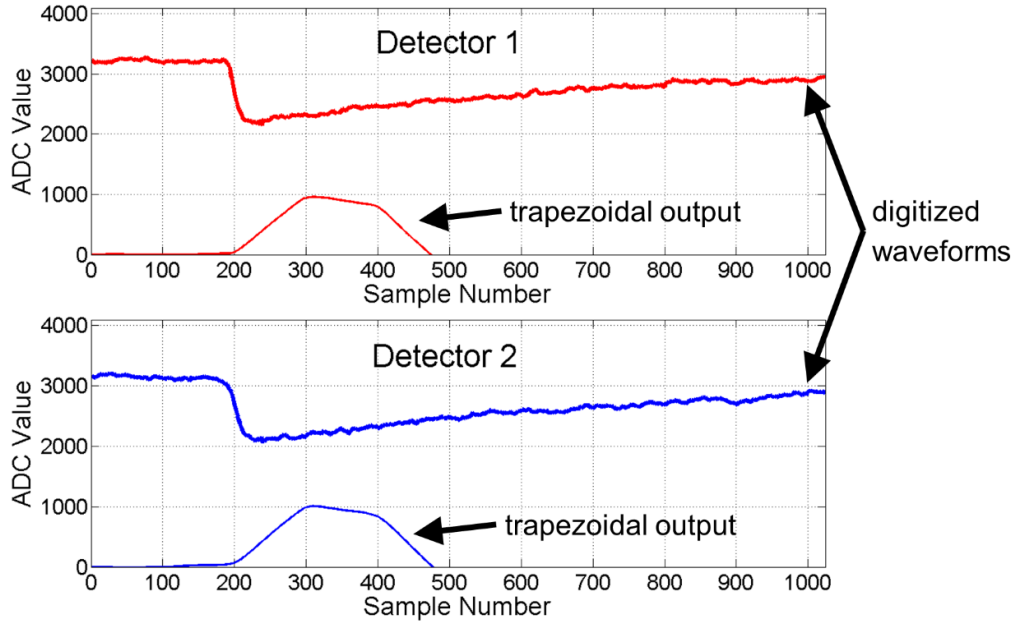

Figure 3-17. Digitized waveforms and trapezoidal outputs from the two CZT crystals.

Figure 3-18 shows the energy spectrum of ^{137}Cs (not calibrated) collected from the two CZT crystals. As it can be seen in this figure, the spectra resulting from both crystals were not in good shapes as expected, each showing a large number of events in the Compton continuum and poor energy resolution. Lots of adjustments such as changing the grid voltages, the subtraction gain, the cathode voltage, and the shaping time were investigated to identify and solve this problem, but no significant improvements were observed, leading us to once again investigate the coplanar electrodes.

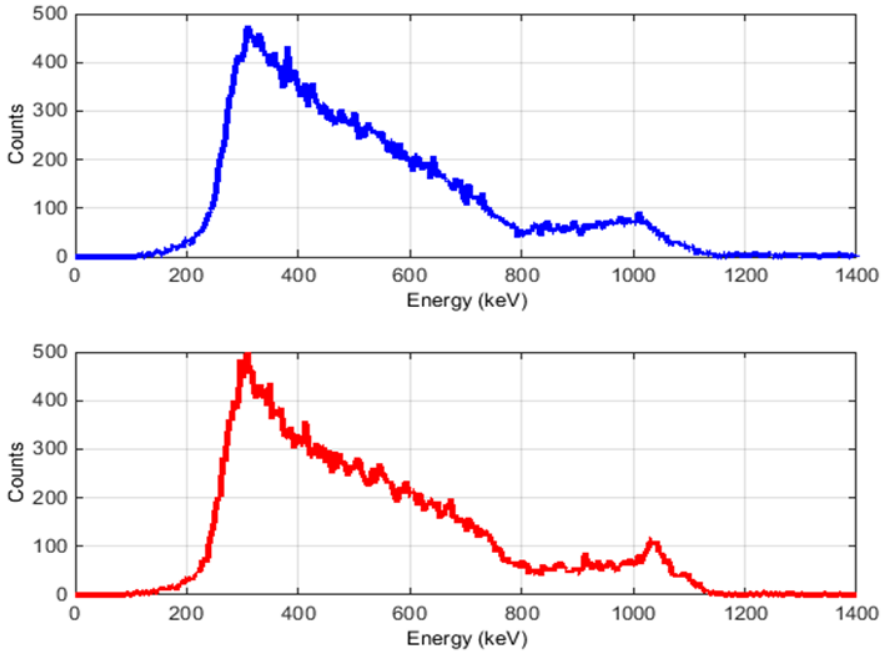

Figure 3-18. ^{137}Cs energy spectrum (not calibrated) of each CZT detector.

The coplanar electrodes were again inspected in more depth using electronic microscope. This time all of the electrode connections were observed to be intact. However, chromium shadowing was observed in the coplanar patterns (Figure 3-19). We suspect that this shadowing changed the uniformity of weighting potentials in the bulk of the crystals and resulted in incomplete charge collection.

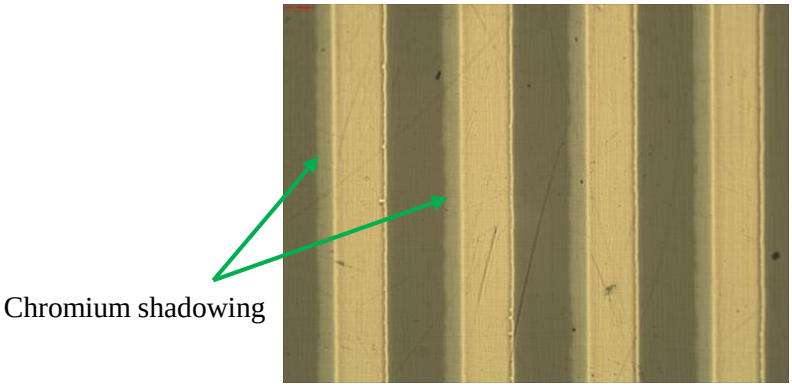

Figure 3-19. Chromium shadowing was observed in the deposited coplanar pattern.

To solve this problem, coplanar patterns were again washed away and a new deposition performed on only one CZT crystal. This time, a single deposition of 300 nm of gold was performed to ensure adhesion to the CZT and to eliminate the chromium shadowing.

The CZT crystal with the new 300 nm gold electrodes was then tested with the best gain and biasing settings to obtain the energy spectrum. Figure 3-20 shows the ^{137}Cs energy spectrum from this crystal. Though it showed better performance, as evidenced by the distinct presence of a single photopeak, it is still far from the expected spectrum from a coplanar CZT device.

We think that the main reason for this discrepancy could be the method of deposition itself since it is possible the deposition energy of the gold is not high enough to fully adhere to the CZT crystal surface. This could lead to significant non-uniformity in the weighting potentials, thus degrading the performance of the crystals.

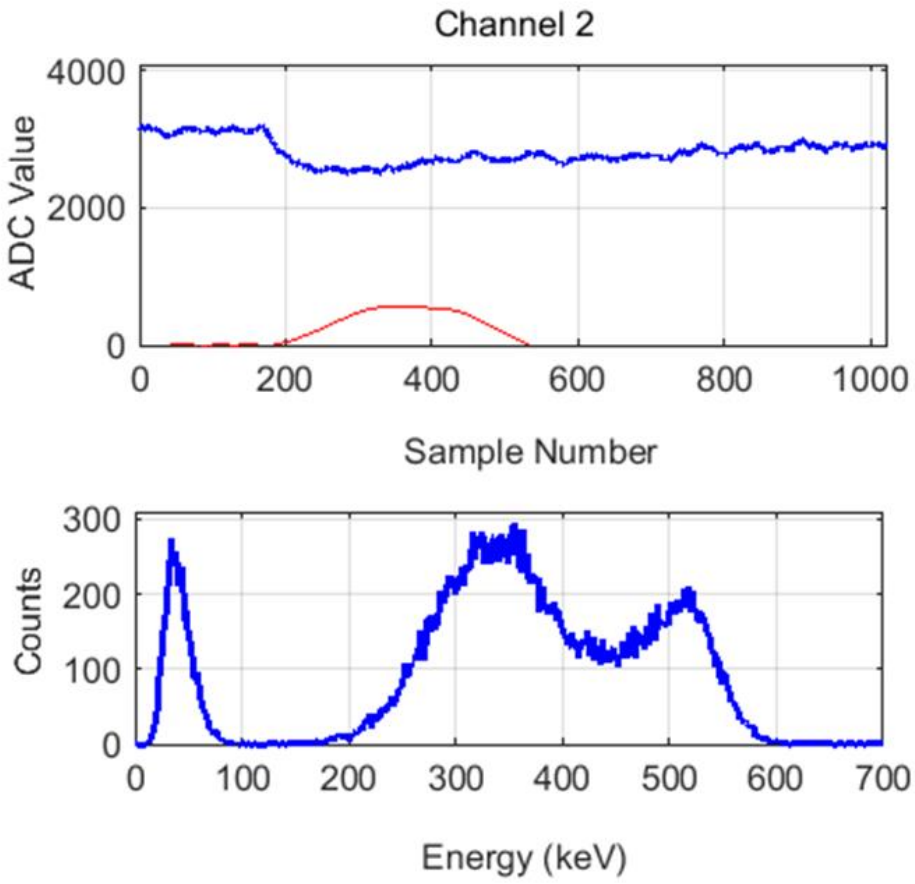

Figure 3-20. Digitized waveforms, trapezoidal output and the ^{137}Cs spectrum (not calibrated) when only gold was deposited on the crystal.

Another reason could be related to cleanness of the VECCO thermal evaporator chamber.

Any remaining contaminations from previous works could stick to the CZT surface and that might create non-uniformity in deposited coplanar pattern and hence degrade the device performance. Generally deposition must be done in a %100 clean facility and in devices that are only used for CZT. However, since the facility is a share place and VECCO is used for a variety of applications, we didn't have any control on the cleanness of the VECCO evaporation

chamber. If any remaining metals from previous deposition sits on the CZT surface, it can create a huge non-uniformity on deposited pattern, even if it is a very tiny particle.

Another reason might be related to the thermal shocks that CZT crystal experiences after deposition when it is being taken out of the VECCO chamber to the room temperature area. Usually temperature inside of the VECCO chamber is very high and so on the CZT's. Even though, VECCO chamber has a cooling system which flows water around the VECCO and cools down the tool, it is possible that CZT is still hot when it is being taken out from the VECCO chamber. This could initiate sudden thermal shocks on the CZT and hence disrupt the connections between the coplanar pattern and CZT surface.

Finally, VECCO evaporation chamber is a very old device. Therefore, it might not be as efficient as new devices.

After inspecting the whole detection system more in depth despite some improvement being made, CZT crystals did not result in a detector with energy resolution approaching the expected performance. Therefore, we decided to instead design and build the second version of our CZT-based radioxenon detection system using CZT crystals with pre-fabricated coplanar electrodes from Redlen Technologies [80].

3.3 Two-Element CZT Radioxenon Detection System (Second Attempt)

The second version of our CZT-based radioxenon detector namely Two-Element coplanar CZT detector (TECZT) uses two 10x10x10 mm^3 coplanar CZT crystals from Redlen technologies. The anode side of one of the coplanar CZT crystals used in this work is shown in Figure 3-21 (a). The anode strip and pitch sizes are both 263 μm.

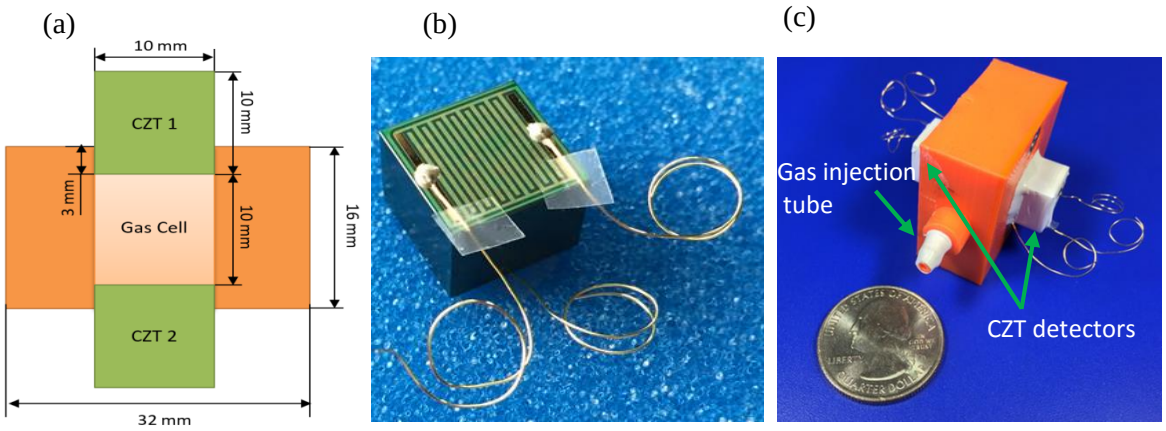

Figure 3-21. (a) Illustration of the TECZT radioxenon detector design. (b) Photograph of the anode side of a CZT crystal from Redlen Technologies used in the TECZT radioxenon detector showing the coplanar anode pattern. (c) Assembled and sealed TECZT radioxenon detector showing the two CZT crystals installed on either side of the gas cell.

3.3.1 Detector Assembly

The coplanar CZT detectors were installed face-to-face on opposite sides of the detector gas cell (Figure 3-21 (c)). This time the gas cell was 3-D printed at OSU using polylactic acid (PLA), a commonly used desktop 3D printing material [81]. We avoided using aluminum-made gas cell after discovering that aluminum interferes with the CZT internal electric field and causes signal instability and noise.

The opening around crystals was sealed using a high vacuum sealant (Torr Seal) to avoid leakage of radioxenon [82].

A new single-channel preamplifier/subtraction PCB was also designed and built to overcome noise issues. The basic design is the same as previous electronics except that this time for each CZT crystal two high performance charge sensitive preamplifiers were used in a

separate PCB board.

The CZT crystals were mounted in close proximity to the PCBs in order to overcome noise issues associated with long leads between the anodes and the preamplifiers. The TECZT detector assembly and the preamplifier and subtraction circuit PCBs were mounted inside an EMI shielded enclosure, shown in Figure 3-22 (a), to reduce noise.

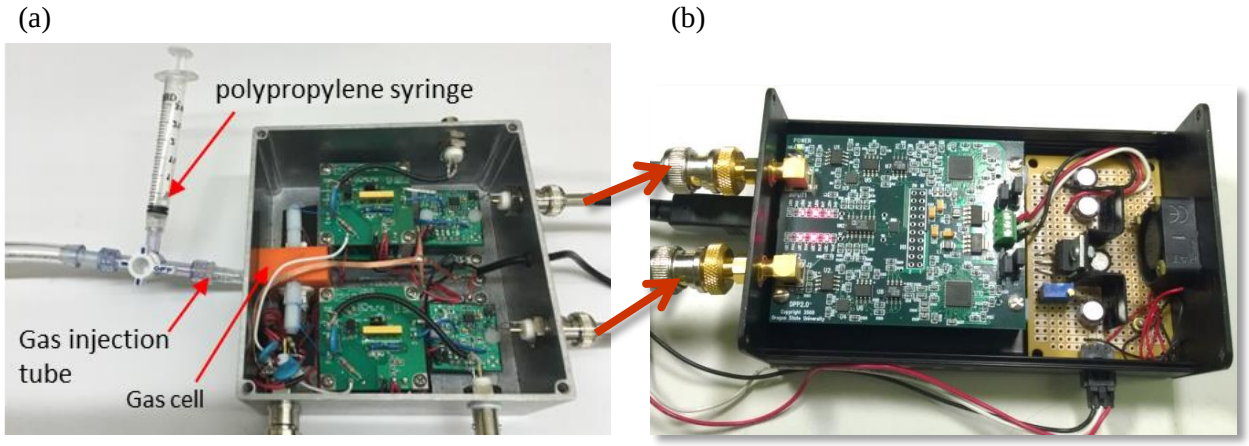

Figure 3-22. The full TECZT radioxenon detection system and electronics, showing (a) the radioxenon sample syringe, gas injection tube, TECZT detector assembly, preamplifiers, and subtraction circuits, and (b) the two-channel digital pulse processor.

Pulses from the TECZT detector were processed and coincidence events were captured in an FPGA as mentioned previously.

Different subtraction gains and different electrode biasing voltages were set for the detector and the energy resolutions of different radioactive laboratory sources were measured in order to find the optimal settings for the system.

In the TECZT system, coincidence detection was performed in real time in the FPGA. Coincidence events are captured and transferred to the PC when the two detectors are triggered within Coincidence Time Window (CTW), which is adjustable from 0 to 1.275 μs with 5 nsec steps (ADC's sampling period). Coincidence Detection Unit continuously monitors trigger signals from each channel and issues a one-shot signal (coincidence ready) when both channels have been triggered within the CTW.

To have better understanding of our detector response to radioxenons of interest, first our detection system was simulated in MCNP to get the coincidence events from radioxenons and generate 2-D coincidence plots.

3.4 MCNP Simulation

The CZT-based radioxenon detection system works based on the beta-gamma coincidence detection technique. To detect and distinguish radioxenon from other atmospheric radionuclides, a two dimensional (2-D) spectrum is constructed based on the coincidence energy released by beta and gamma interactions in each CZT detector.

In another word, the energy deposited in CZT1 (channel 1) must be plotted versus the energy deposited in CZT2 (channel 2). In order to accurately predict the shape and regions of interest of the 2-D spectrum, the CZT-based detector was simulated using MCNP6 [83].

The dimensions of the simulated components were chosen to be the same as the real detector system, including the 10 x 10 x 10 mm^3 CZT crystals and 1 cm^3 gas cell volume, as shown previously in Figure 3-21 (a).

The gas cell material was defined as a mixture of C, H, N, and O best approximating the

PLA 3D-printing material and was filled with a mixture of nitrogen and xenon.

To properly imitate the 2-D spectrum, it is required to obtain beta-gamma coincidence events of each radioxenon in both CZTs. To find these coincidence events it is essential to track each particle (beta and gamma) separately in each of the CZT detectors. The PTRAC card was used to find the track of beta and gamma particles in CZT crystals and get the coincidence information for our detector. This card follows each particle individually and records the entire history of that particle which is written in an output file called PTRAC. This file contains the important parameters of each particle such as the position of interaction, the energy of the particle, and the history number, which are all used to determine whether a given particle was coincident with another.

Since the PTRAC card generates an output file on the order of gigabytes and extracting the information is very difficult and time consuming, some parameters were filtered in the MCNP deck to decrease the PTRAC output size by almost 50%.

A cluster computer consisting of 12-processor 3.0 GHz Intel Xeon servers, with 200GB SDRAM each was used to run the simulations for 10^7 particles.

Using the same method, for each radioxenon of interest a separate PTRAC file for betas/conversion electrons and another PTRAC file for gamma/X-ray was built to be used later to find the coincidence events.

3.4.1 Algorithms to Parse the PTRAC Files and Extract Coincidence Events

To parse PTRAC files and extract required information from those file a Python code was written based on two algorithms which will be discussed in more detail here.

3.4.1.1 Brief Description of the PTRAC Output File

Each particle history in PTRAC output file starts with the NPS number and the type of the following interaction. It then, depending on the type of the interaction, continues by some information about that specific interaction.

In each PTRAC output file, five different groups of events are present, represented as number, and listed in Table 3-1 [83], [84]. Figure 3-23 shows an example of the PTRAC card output file.

Table 3-1. Five different groups of events in PTRAC output file

PTRAC number	Event Type
2000	new particle history
3000	particle has crossed a surface
4000	particle has had a scattering event
5000	last event/history termination
9000	last line in PTRAC history

As can be seen in Figure 3-23, the PTRAC output format is like a data tree structure with branches which includes data structure of a particle and all the progeny which create other progeny. Therefore, it is not possible to simply extract the required information from the PTRAC output file and it must be parsed to extract the information relevant to the coincidence events.

To parse the PTRAC output, a separate code was written in Python [85] and used to extract

the energy released by all beta and gamma particles in each CZT detector as well as the respective history number (NPS) from their PTRAC files.

Another python code was then written to extract the energy released by only beta-gamma coincidence events in CZT 1 and CZT 2 based on coincidence interaction scenarios that we defined.

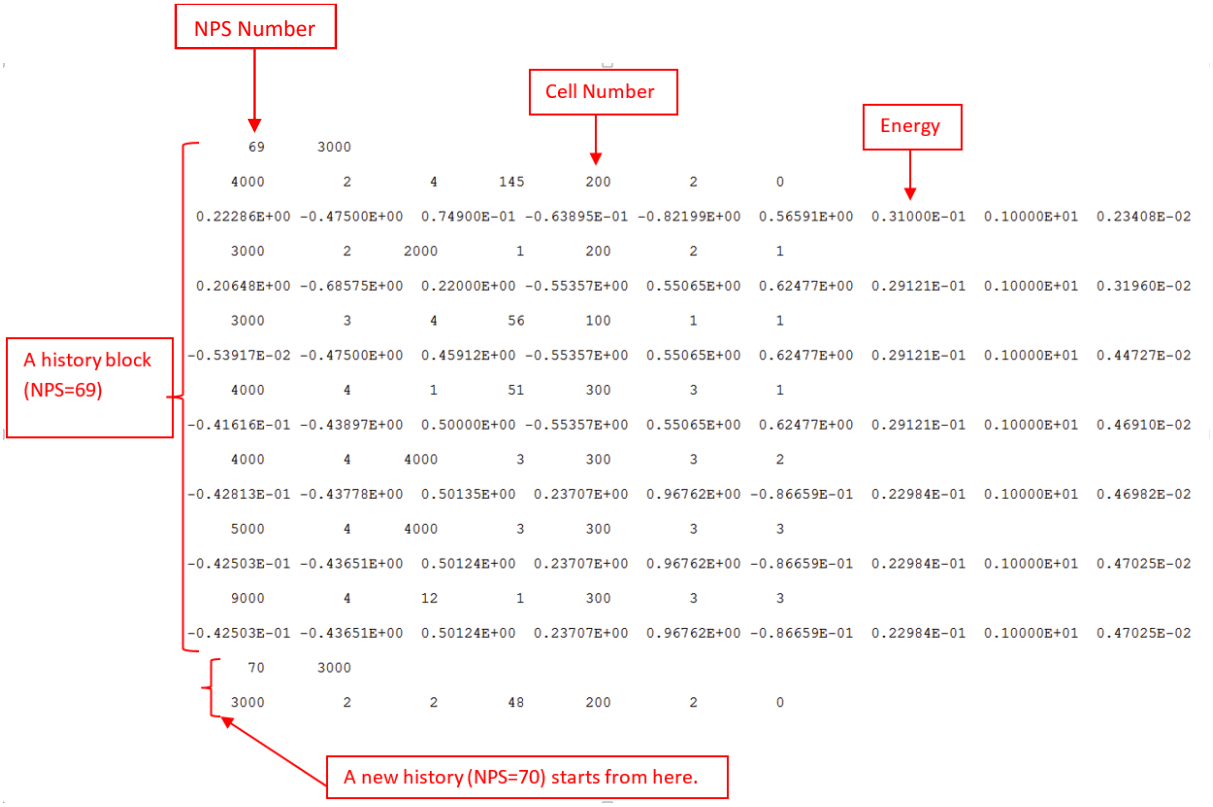

Figure 3-23. An example of one PTRAC history block from 31 keV X-rays of ^{131m}Xe.

For coincidence detection of beta and gamma only two scenarios were considered. Scenario 1 is when a beta particle interacts in CZT 1 and a gamma ray interacts in CZT 2, whereas

scenario 2 is defined as the opposite of scenario 1 (Figure 3-24).

The Python code considers an event the coincidence event if and only if the respective NPS for both beta and gamma for that event are the same.

The energy released in each CZT crystal by beta-gamma coincidence events was then used to construct the 2-D spectrum in MATLAB for each radioxenon isotope.

Gaussian broadening was also artificially applied to the gamma, X-ray and conversion electrons energies.

A flowchart of the Python codes are shown in Figure 3-25 and Figure 3-26.

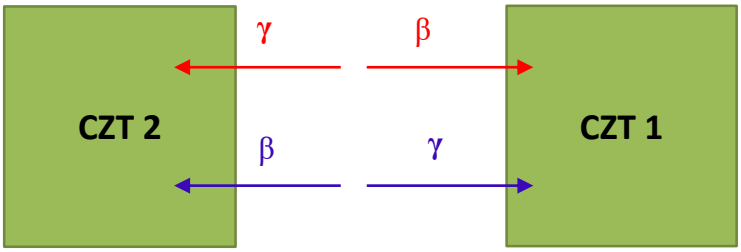

Figure 3-24. Coincidence interaction scenarios of beta and gamma in CZT detectors.

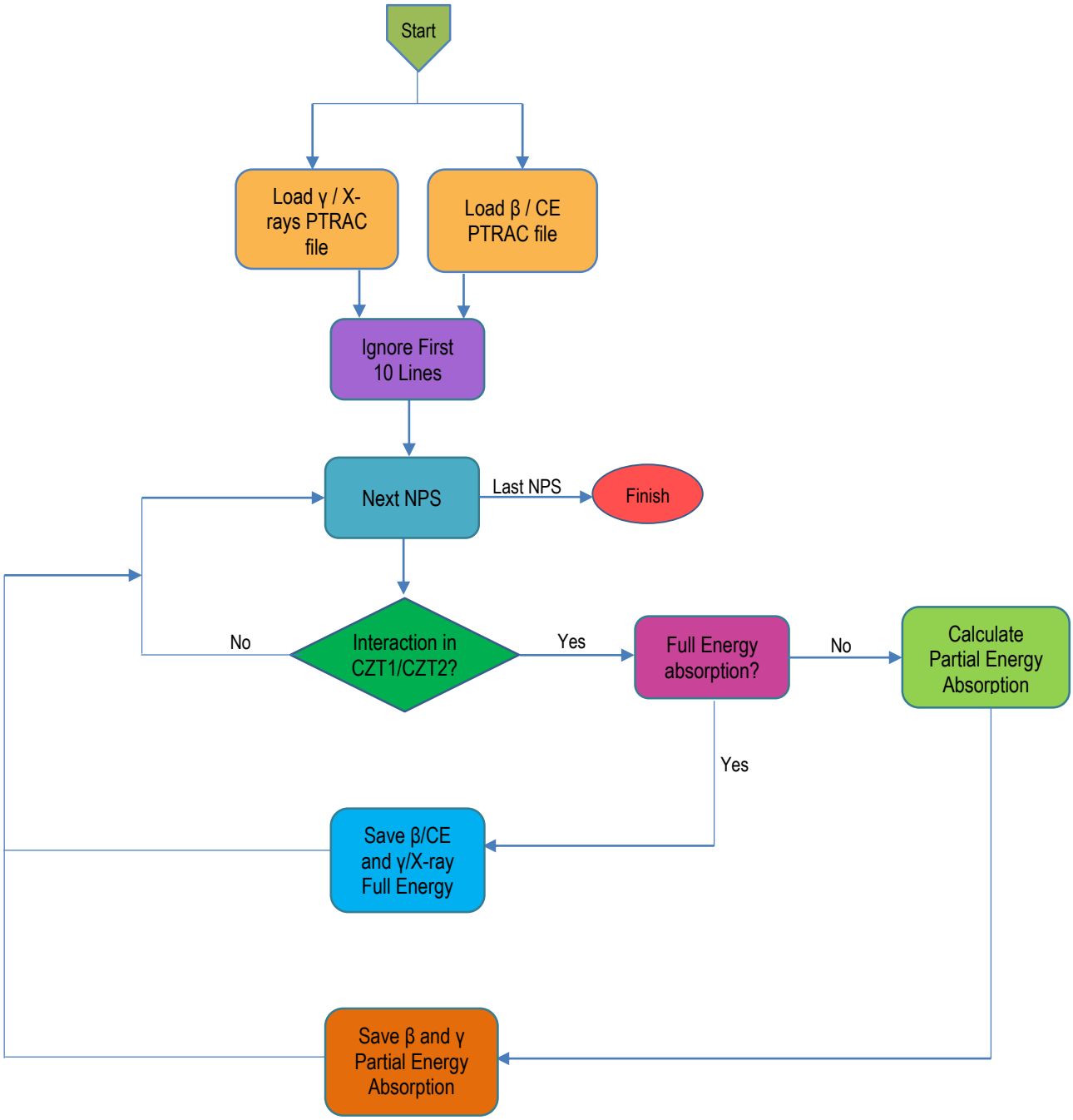

Figure 3-25. Flowchart of the Python code algorithm to parse the PTRAC Files and extract beta/CE and gamma/X-rays energies deposited in CZT 1 and CZT 2. Energies extracted from this flowchart then will be loaded to another flowchart (Figure 3-26) to find and store the beta-gamma coincidence information.

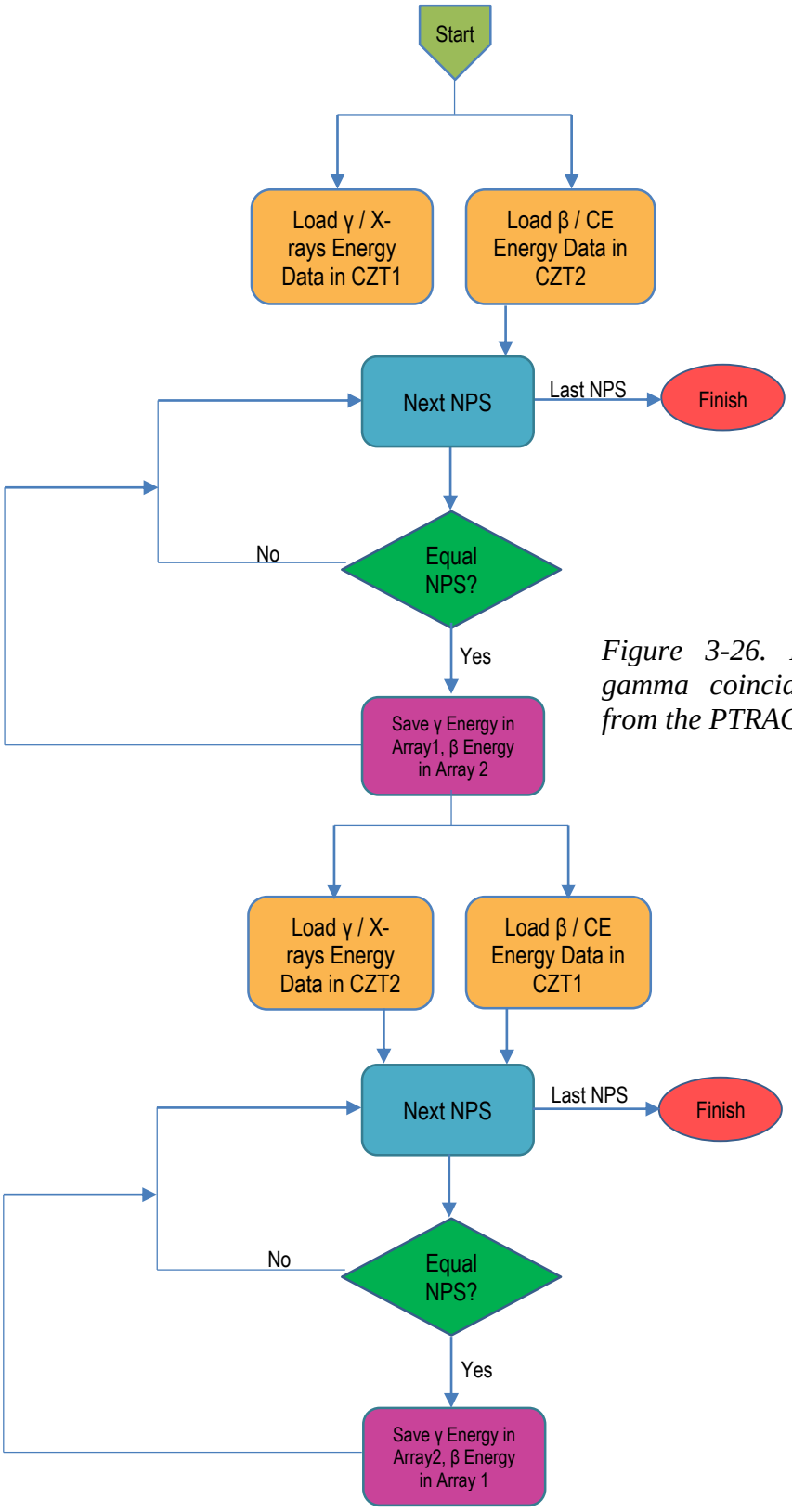

Figure 3-26. Flowchart of the beta-gamma coincidence capture algorithm from the PTRAC files.

3.4.2 Simulation Results

3.4.2.1 ^{135}Xe

After running the Python codes and extracting coincidence energy information, two energy arrays were built (one for each CZT crystal) to construct the coincidence 2-D spectrum.

To make sure our codes are working as we expected, energy deposited by beta and gamma were first plotted separately in each CZT detector (

Figure 3-27and Figure 3-28). The data composing these spectra were extracted from coincidence energies that each beta particle and gamma ray deposited in each of the CZT crystals.

As shown in these figures, shape of the histogram is a combination of the beta and gamma spectra, a distribution of beta energies from 0 to 905 keV and 250 keV gamma peak superimposed on the beta spectrum. In addition, the shape and the number of counts are almost the same for both CZTs, which is also expected due to the symmetric design of the system.

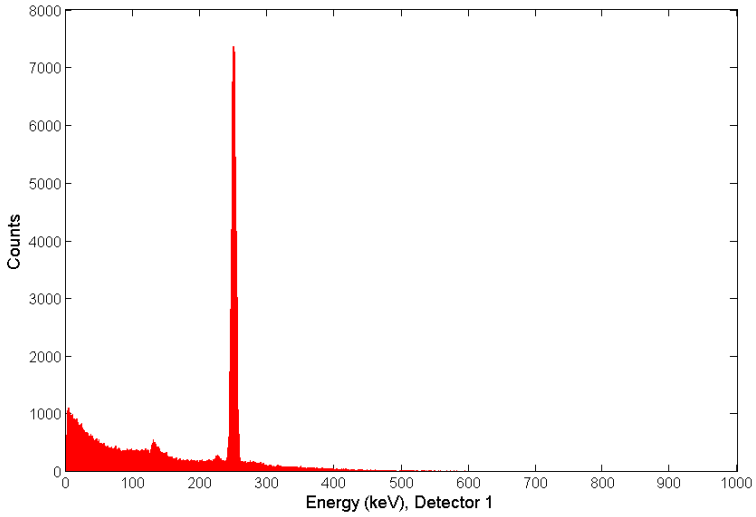

Figure 3-27. Simulated energy deposited by ^{135}Xe coincident events in CZT1.

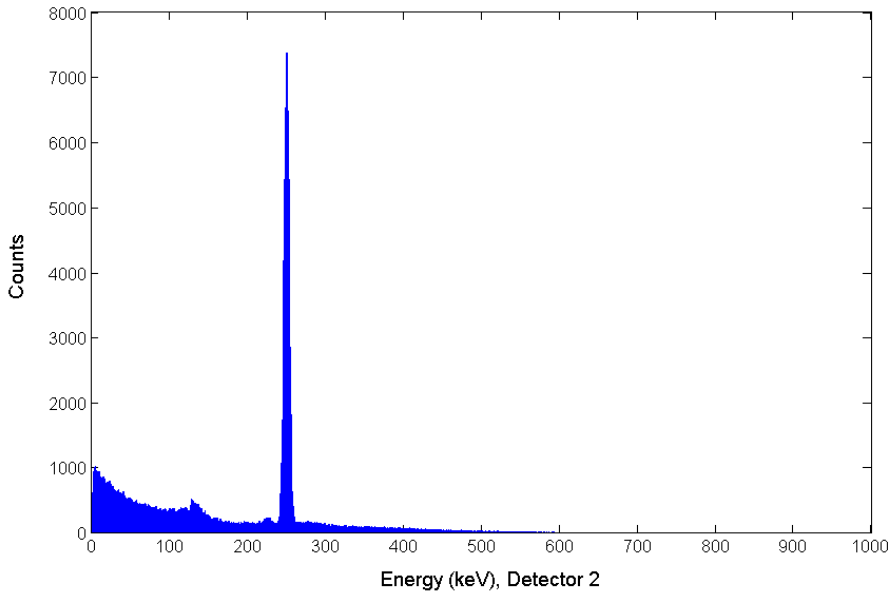

Figure 3-28. Simulated energy deposited by ^{135}Xe coincident events in CZT2.

These figures show that the algorithms implemented in Python to capture energies from the PTRAC files works as we expected and can be used to generate the 2-D coincidence spectra. Lastly, the 2-D beta-gamma coincidence spectrum of ^{135}Xe was plotted using MATLAB. Figure 3-29 shows the resulting 2-D beta-gamma coincidence spectrum of ^{135}Xe. ^{135}Xe emits 250 keV gamma rays in coincidence with beta particles (E_{max} ~ 905 keV). This spectrum features two broad lines at 250 keV which are extended up to around 910 keV (maximum beta energy of ^{135}Xe), forming bands of coincident events with betas detected in the other CZT detector. The most important feature of this spectrum is the line which connects the 250 keV gamma events in one channel (Ch1 Energy 1 axis) to the 250 keV gamma events in the other channel (Ch2 Energy axis). This line represents those coincidence Compton scattering events which deposited energy in both CZT1 and CZT2. This line is expected to be observed in a 2-D spectrum

generated using our CZT-based detection system if the system is functioning properly.

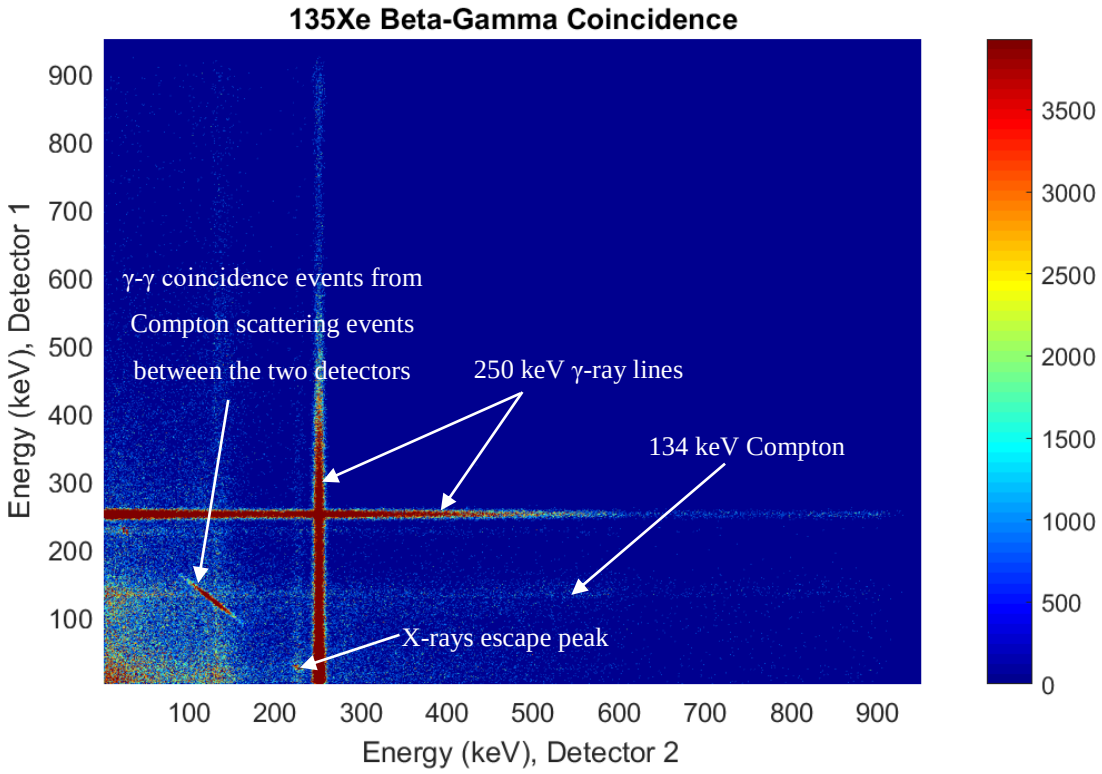

Figure 3-29. Coincidence beta-gamma spectrum from ^{135}Xe simulated using MCNP.

Another important set of features in this spectrum are the X-ray escape peaks from Cd (23 keV) and Te (27 keV) [7] which are seen at 223 and 227 keV. However, because of the broadening applied to the gamma events (energy resolution of the CZT detector) these two lines are faded into each other and appear at about 225 keV. The Compton edge can be also seen in this spectrum at 134 KeV. Since both CZTs can detect either beta or gamma, both axes include the same features.

3.4.2.2 ^{131m}Xe

^{131m}Xe emits 31 keV X-rays in coincidence with 129 keV conversion electrons. Figure 3-30

shows the 2D coincidence scatter plot for ^{131m}Xe obtained using MCNP. As it is clearly visible, two crossing lines are observed at 31 keV where a populated region is formed around 129 keV. These lines have formed from the coincidence events between 31 keV and 129 keV conversion electrons. X-ray escape peaks from Cd (23 keV) and Te (27 KeV) can also be observed at about 5 keV. However, as mentioned in a previous report, this plot did not follow our expectations. Two crossing lines can be observed below 31 keV at about 22 keV whose origin we were unable to account for. After closely looking at the K and L characteristic X-rays from Cd, Zn and Te, it was found that these lines are associated with X-ray escape peaks from Zn. Table 1 shows K edges and characteristic X-rays in Cd, Zn and Te.

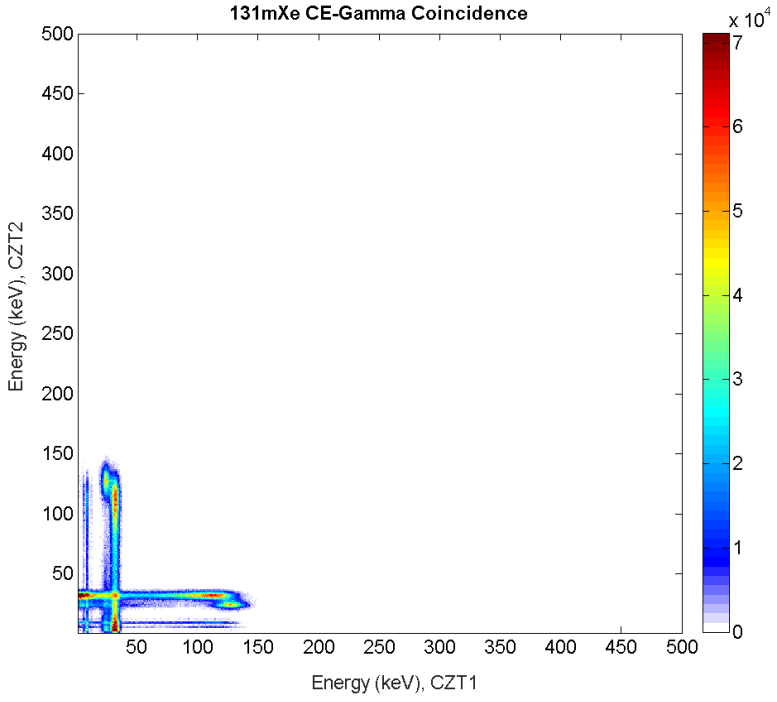

Figure 3-30. Coincidence beta-gamma energy spectrum from ^{131m}Xe simulated using MCNP after applying broadening.

The K edges for Cd, Zn and Te are 26.72, 9.66 and 31.8 keV respectively. Photons with incident energies just above these edges undergo photoelectric interactions, leaving the Cd, Zn and Te atoms in an excited state. When the atoms transition to the ground level they often emit a characteristic X-ray at one of the energies shown in Table 3-2. Depending on the direction, this X-ray may leave the CZT volume so that only a small amount of the incident energy is deposited. This process is responsible for the escape peaks which are observed in our plot.

Table 3-2. Energies of the K edges and the characteristic X-rays in Cd, Zn and Te [2].

Element	K edge (eV)	$K_{\alpha 1}$ (eV)	$K_{\alpha 2}$ (eV)	$K_{\beta 1}$ (eV)	$L_{\alpha 1}$ (eV)
Cd	26.72	23.173	22.984	26.095	31.337
Zn	9.66	8.638	8.615	9.572	1.0117
Te	31.80	27.472	27.201	30.995	3.769

For Zn, the K-edge is 9.66 keV where multiple characteristic X-rays are observed at 8.638, 8.615 and 9.572 keV. The differences between these X-rays and the 31 keV X-ray account for the features shown in Figure 3-30. To see these escape peaks more clearly, we took off the broadening applied to 31 keV X-rays and 129 keV conversion electrons. Then, the 2D coincidence plot was generated again (Figure 3-31). In this figure multiple escape lines belonging to Zn escape peaks are evident below 31 keV.

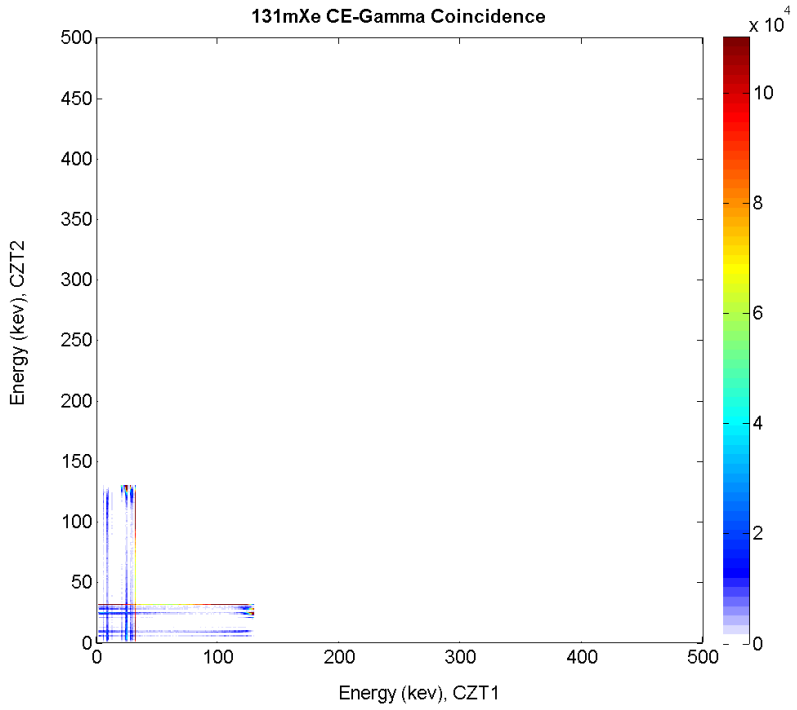

Figure 3-31. Coincidence beta-gamma energy spectrum from ^{131m}Xe simulated using MCNP without applying any broadening.

After applying broadening (determined through measurements) of our detection system, the 2D coincidence plot was generated again. As can be seen here the escape lines below 31 keV are faded into each other and into 31 keV as well (Figure 3-32).

It's worth mentioning that our Python algorithm was also modified and improved to pick all possible coincidence events. After these improvements the diagonal line which shows conversion electrons coincidence events between two CZT crystals was constructed in the 2D coincidence plot as well. These coincidence events belong to those events in which a conversion electron interacts in one of the CZTs, releases parts of its energy there and then back scatters from that crystal and releases its remaining energy into the other crystal.

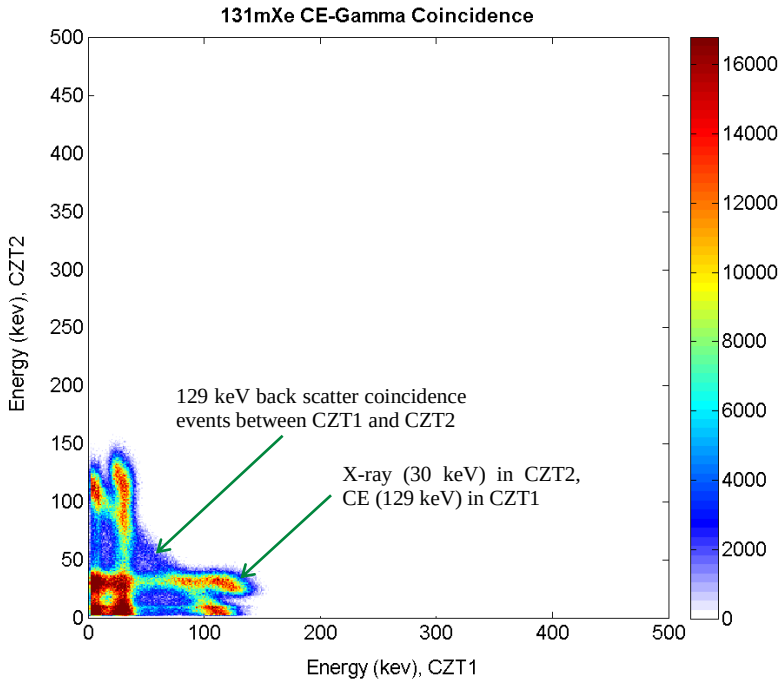

Figure 3-32. Coincidence beta-gamma energy spectrum from ^{131m}Xe simulated using MCNP after applying real broadening of our detection system.

3.4.2.3 ^{133m}Xe

The same issues that were present in our previous simulation results for ^{131m}Xe were also present in our ^{133m}Xe simulations (Figure 3-33). Again for ^{133m}Xe the 2D plot was generated without any broadening (Figure 3-34). Multiple lines associated with the multiple escape peaks of Zn are observed below 31 keV. After applying real broadening of our detection system to 31 keV X-rays and 199 keV conversion electrons these lines were faded into each other and into 31 keV as well (Figure 3-35). Our Python algorithm was also improved to pick all possible coincidence events. After these improvements the diagonal line which shows conversion electrons coincidence events between two CZTs was also appeared in ^{133m}Xe 2D coincidence

plot. These coincidence events belong to those events in which a conversion electron interacts in one of the CZTs, releases part of its energy there and then back scatters from that crystal and releases its remaining energy into the other crystal.

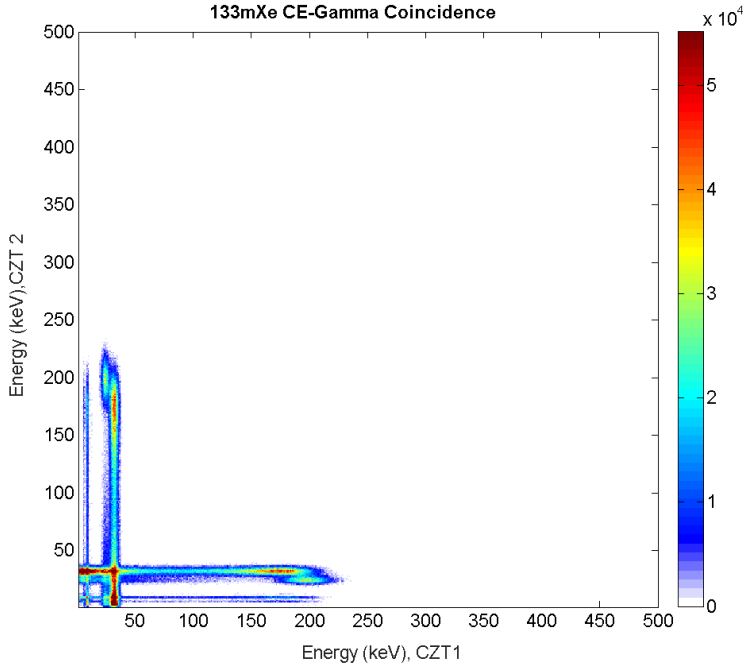

Figure 3-33. Coincidence beta-gamma energy spectrum from ^{133m}Xe simulated using MCNP after applying 20% broadening.

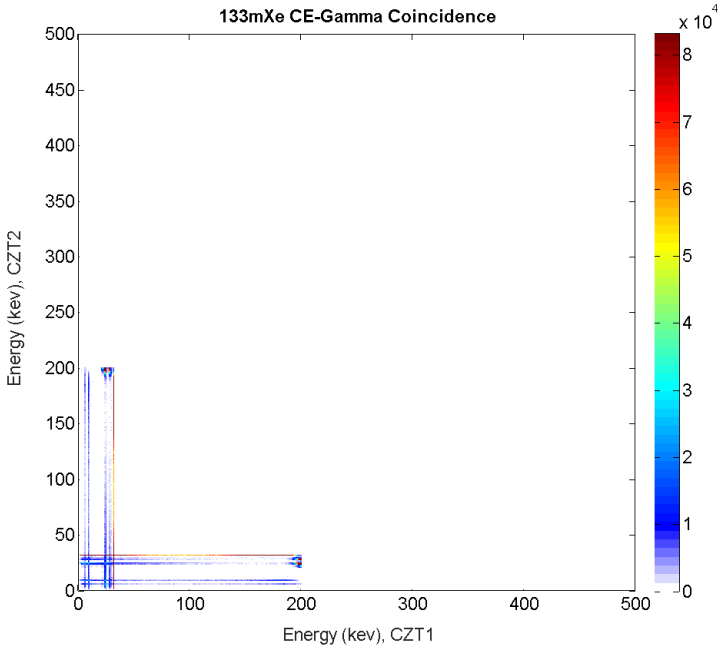

Figure 3-34. Coincidence beta-gamma energy spectrum from ^{133m}Xe simulated using MCNP without applying any broadening.

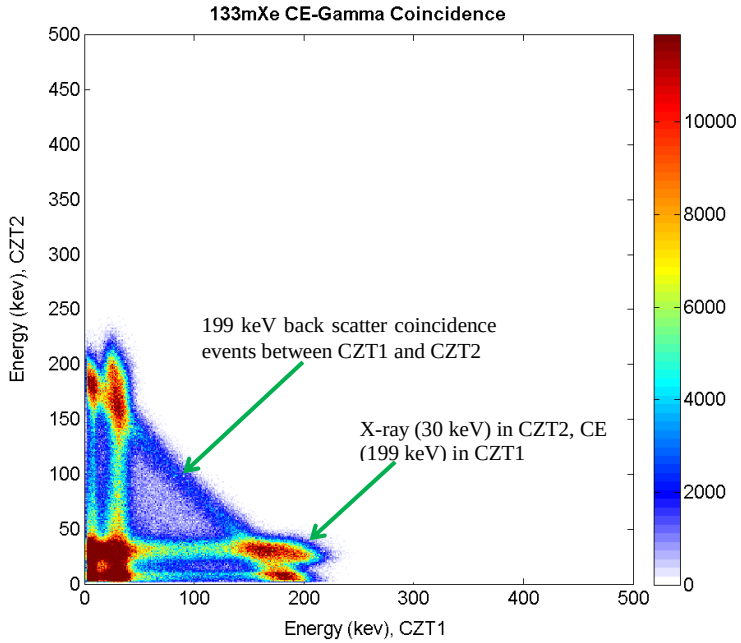

Figure 3-35. Coincidence beta-gamma energy spectrum from ^{133m}Xe simulated using MCNP after applying real broadening of our detection system.

3.4.2.4 ^{133}Xe

^{133}Xe is the most complicated radioxenon due to its multiple coincidence decay modes. It emits beta particles (E_{max}=346 keV) in coincidence either with 81 keV gamma-rays (~37%) or with 31 keV X-ray and 45 keV conversion electrons (~47%).

In order to obtain the 2D coincidence plot for this radioxenon, four separate MCNP decks were run for 31 keV X-rays, 45 keV conversion electrons, 81 keV gamma rays and 346 keV betas. Each simulation was run with 10^7 particles in order to generate PTRAC files for these energies. PTRAC files were then parsed using our Python code. The coincidence information from these PTRAC files was then extracted considering events with the same NPS as the coincidence events. It should be mentioned that to extract these coincidence events the probability of each coincidence mode was also taken into account (37% for 81 keV gammas in coincidence with 346 keV betas and 47.63% for 31 keV+45 keV in coincidence with 346 keV betas).

After identifying all coincidence events, the 2D coincidence plot was generated for ^{133}Xe in MATLAB which is shown in Figure 3-36. To generate this plot 40% FWHM broadening was applied to 31 and 45 keV and 12% FWHM was applied to 81 keV.

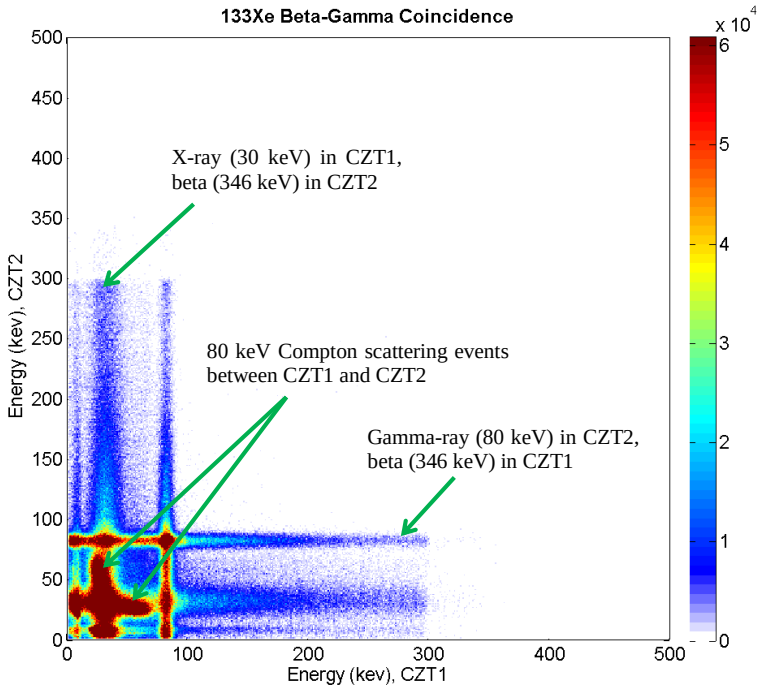

Figure 3-36. Coincidence beta-gamma energy spectrum from ^{133}Xe simulated using MCNP after applying broadening

As can be seen in this figure, two crossing lines are populated at 31 keV and 80 keV and extended up to 346 keV which are representative of coincidence events between beta with 31 and 81 keV. Coincidence Compton scattering events from 81 keV are also observable in this plot.

In this plot, there is a sharp drop at 30 and 80 keV line after 300 kV. The reason for this is that in MCNP deck, the beta source was defined using only 6 energy regions while the probability of energies higher than 300 keV was very small compared to other energy regions.

Do not feel lonely;
The entire universe in inside of you.
Rumi, 13th century Persian poet

4 Results and Discussion

4.1 General Characterization

General and coincidence characterization of the TECZT detector was performed using laboratory sources.

Before performing radioxenon measurements it was vital to find the optimum values for all the parameters that can affect the detector performance. These factors include grid and bias voltages, gain of the collecting and non-collecting grids, trapezoidal filter's flat top and peaking times and so on.

These optimum values were then kept constant during the rest of the measurements with TECZT.

4.1.1 Optimum Operating Voltages and Shaping Parameters

To study the effect of the flat top and peaking times of the trapezoidal filter on the energy resolution as well as to find the optimum operating voltages, ^{109}Cd and ^{137}Cs sources were placed at the top of the detector gas cell as shown in Figure 4-1. These sources were used to study the effect of the filter times on both low and high energy regions.

The flat top and peaking times of the trapezoidal filter were then changed from 0.4 μs to 1 μs with 0.2 μs step and energy resolution of 88 keV from ^{109}Cd and 662 keV from ^{137}Cs were measured each time.

These measurements were also done for two sets of operating voltages: ($V_{cathode}$= 1000 V,

V_g=80 V and $V_{cathode}$= 1500 V, V_g=120 V).

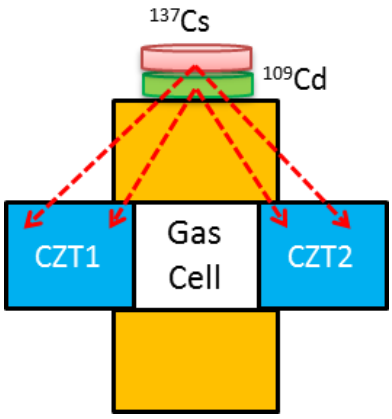

Figure 4-1. Geometry of the measurements to find the optimum flat top and peaking times of the trapezoidal filter as well as the operating voltages.

The results of these measurements are presented in Table 4-1 and Table 4-2. As can be seen from these tables, by increasing the peaking time of the trapezoidal filter, the energy resolution for both 88 keV and 662 keV continues to improve. However, after a flat top time of 0.8 µs, energy resolution begins to worsen instead.

Table 4-1. Energy resolution at different flat top and peaking times for $V_{cathode}$= 1000 V and V_g=80 V.

Peaking Time (µs)	**0.4**		**0.6**		**0.8**		**1**	
Flat top (µs)	**Energy resolution (%)**							
	88 keV	**662 keV**	**88 keV**	**662 keV**	**88 keV**	**662 keV**	**88 keV**	**662 keV**
0.4	13.5	3.5	13.2	2.8	12.5	2.6	12.2	2.41
0.6	13.8	2.7	13.2	2.5	12.3	2.32	11.9	2.3
0.8	13.1	2.67	12.9	2.46	12.1	2.22	**11.8**	**2.1**
1	13.2	2.64	13.6	2.56	12.7	2.41	12.2	2.31

By increasing the grid and cathode voltages, the energy resolution of our system worsen. By increasing the biasing voltage, electrons in the CZT volume travel faster and the chance of trapping will decrease, so we expect to get better energy resolution.

Table 4-2. Energy resolution at different flat top and peaking times for $V_{cathode}$= 1500 V and V_g=120 V.

Peaking Time (μs)	**0.4**		**0.6**		**0.8**		**1**	
Flat top (μs)	**Energy resolution (%)**							
	88 keV	**662 keV**	**88 keV**	**662 keV**	**88 keV**	**662 keV**	**88 keV**	**662 keV**
0.4	15.5	2.52	17.0	2.25	15.6	2.3	13.4	2.2
0.6	18	2.9	14.7	2.42	13.5	2.4	12.7	2.3
0.8	20	2.92	15.5	2.7	15.1	2.5	14.2	2.4
1	23	3.1	17.8	3.3	16.6	2.7	15.8	2.5

However, the leakage current of the system will be more significant by increasing the bias voltage which in turn degrades the energy resolution of the system. Therefore, to avoid increasing the leakage current, lower operating voltages are preferred. For all of the measurements, the following parameters were used, since the best energy resolutions for 88 keV and 662 keV were obtained using a cathode bias voltage of -1000 V, a grid voltage of +80 V, a 1 μs trapezoidal peaking time and a 0.8 μs trapezoidal flat top time.

It should be mentioned that the optimum parameters were found for trapezoidal filter are appropriate to capture both single- and multi-event pulses. Figure 4-2 shows a double-event pulse captured by the DPP2. The response of a trapezoidal filter, with a peaking time of 0.5 μs and a flat top of 1.0 μs, is also shown in Figure 4-2.

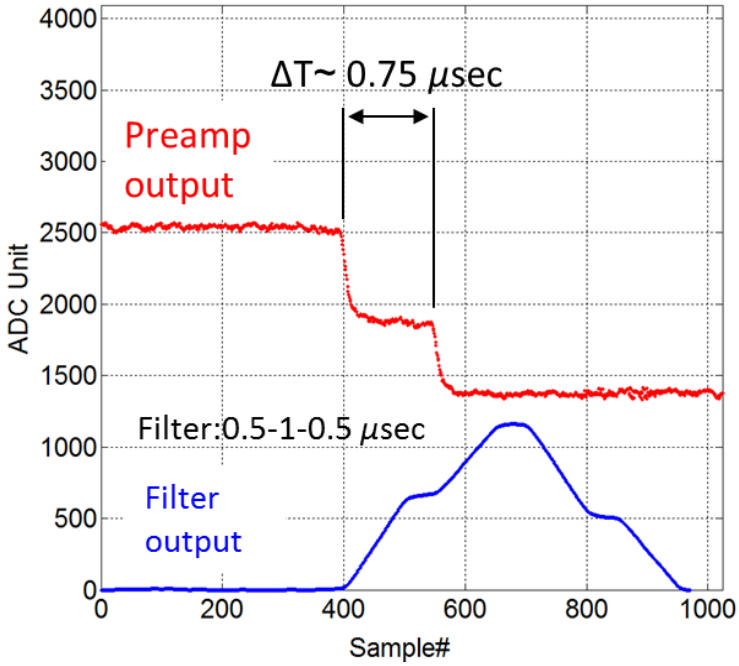

Figure 4-2. A double-event pulse and the response of a trapezoidal filter with peaking and flat times of 0.5 μs and 1.0 μs, respectively.

4.1.2 Optimum Coincidence Time Window

As mentioned before, in the TECZT system, coincidence detection was performed in real time in the FPGA. Coincidence events are captured and transferred to the PC when the two detectors are triggered within Coincidence Time Window (CTW), which is adjustable from 0 to 1.275 μs with 5 nsec steps (ADC's sampling period). Coincidence Detection Unit continuously monitors trigger signals from each channel and issues a one-shot signal (coincidence ready) when both channels have been triggered within the CTW.

Since the arrival time of pulses from a coplanar CZT detector is a function of the interaction depth, an experiment was conducted to investigate the time range of the coincidence events. A

^{60}Co source was placed on the top of the gas cell (Figure 4-3 (a)) and the rate of the coincidence events from the simultaneously-emitted 1.17 and 1.33 MeV gamma rays was recorded versus the coincidence time window set in the FPGA. ^{60}Co emits two cascading gamma-rays (1.17 and 1.33 MeV) and thus is well suited for this experiment.

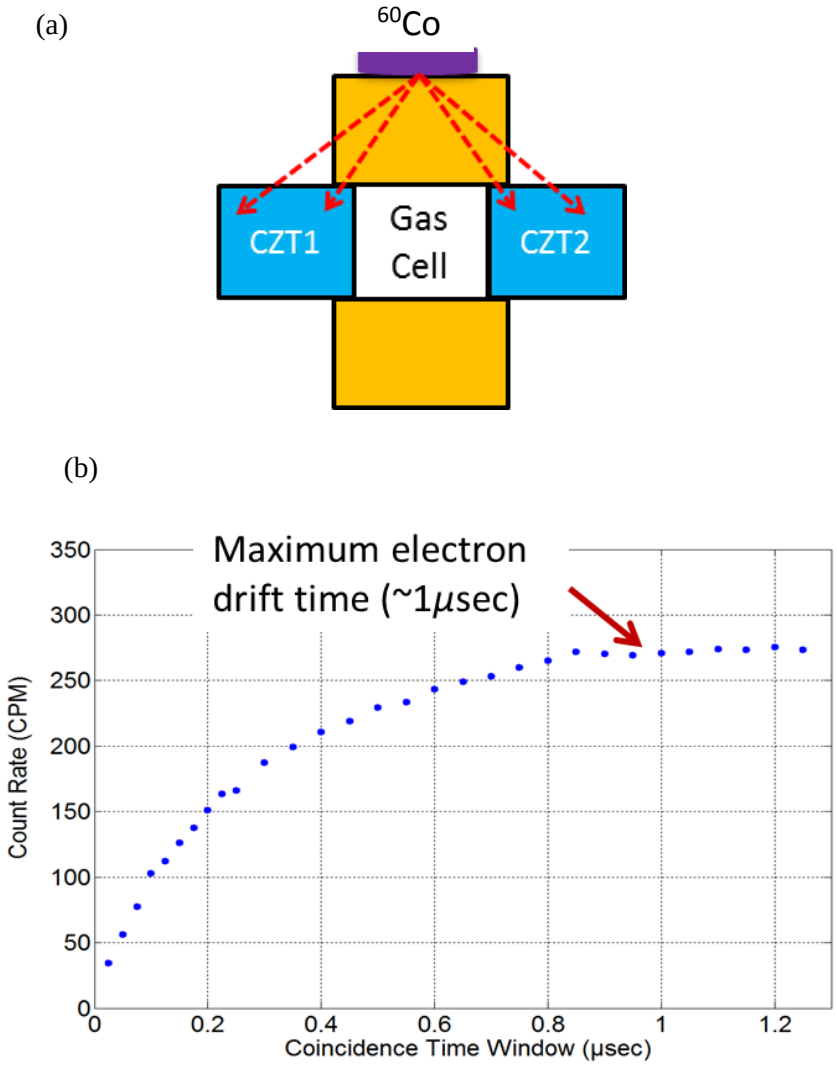

Figure 4-3. (a) Geometry of the measurements used to find the optimum Coincidence Time Window. (b) Coincidence count rate versus Coincidence Time Window measured using ^{60}Co.

Figure 4-3 (b) shows the results of these measurements. As shown in this figure, the

coincidence count rate reaches a flat region at about 0.8 µsec. This is close to the maximum electron drift time (τ_e) in this CZT crystal with detector biasing of 1000 V (~1 µsec) [86]. Therefore, for the rest of the measurements in this work the CTW was set to 0.8 µsec. It should be highlighted that maximum electron's drift time in CZT crystals can be calculated using the following equation [87]:

$$\tau_e = \frac{d}{v_e} = \frac{d}{\mu_e . E} = \frac{d}{\mu_e . (\frac{V}{d})} = \frac{d^2}{\mu_e . V} \qquad (1)$$

Where:

τ_e= electron's drift time in CZT crystal

d: CZT thickness (10 mm)

v_e: electron's drift velocity in CZT crystal

μ_e: electron's mobility in CZT crystal (1350 $cm^2/V.s$)

E: electric field strength in CZT which is proportional to the applied bias voltage

V: applied bias voltage (1000 V)

After finding the optimum operating conditions for the TECZT detector, radioactive lab sources were used to characterize the energy resolution of the system.

Figure 4-4 and Figure 4-5 show energy spectra of ^{137}Cs and ^{60}Co collected from the two CZT detectors. The best energy resolutions obtained for 662 keV were 2.3% and 2.7% FWHM for CZT 1 and CZT 2, respectively.

In order to get the best energy resolutions, detectors must be irradiated from the cathode side of each CZT crystal inside of the gas cell. Since such a setup was not possible with the assembled gas cell, the sources were placed at the top of the gas cell, as shown in Figure 4-3. Additionally, while CZT 1 shows better overall performance compared to CZT 2, the channel connected to CZT 2 shows better electronic performance (11.1 keV FWHM pulser resolution for CZT 2 vs. 11.6 keV FWHM for CZT 1).

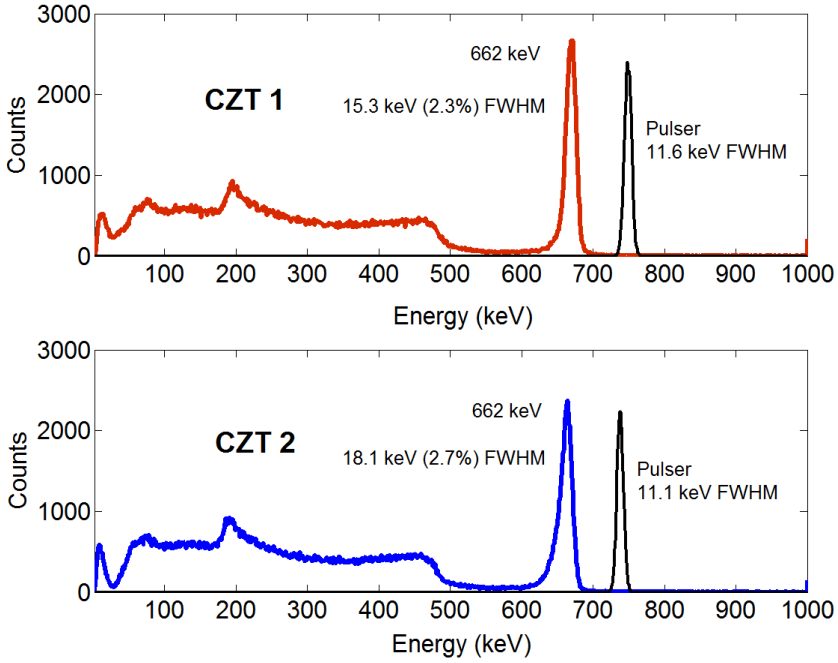

Figure 4-4. Energy spectrum of ^{137}Cs from CZT1 and CZT2.

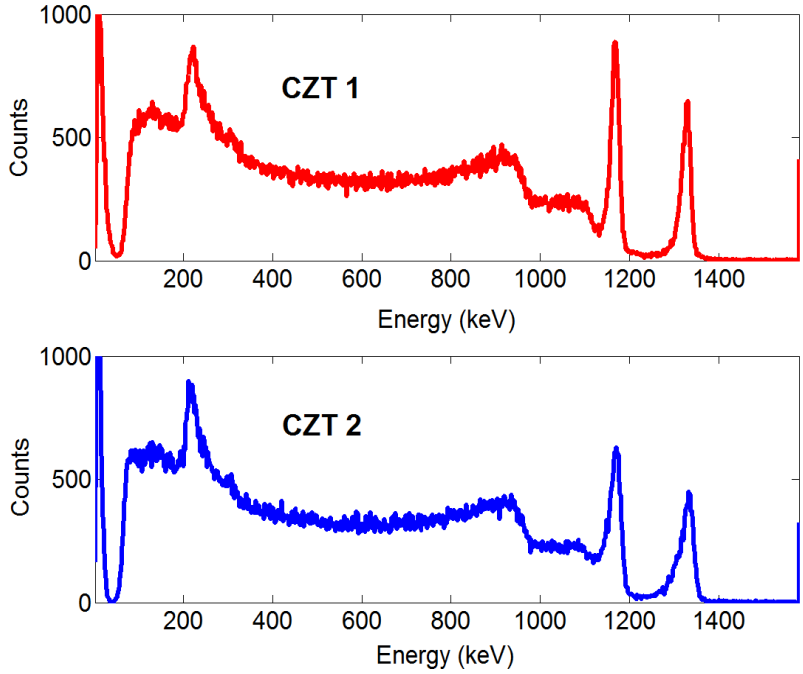

Figure 4-5. Energy spectrum of ^{60}Co from CZT1 and CZT2.

4.1.3 Modification in Electronics and FPGA Firmware

4.1.3.1 Hardware Modifications

As it is illustrated in Figure 4-4, 31 keV peak from ^{137}Cs is not visible in ^{137}Cs energy spectra due to creating pulses whose amplitudes were below the noise level of the prototype readout electronics. To enhance the signal-to-noise ratio and making our detection system capable of detecting 31 keV from ^{133}Xe, ^{133m}Xe and ^{131m}Xe, the electronics of our system were modified. This modification was done by removing a PCB trace that connects the preamplifier to the feedback capacitor (CF). This modification was done on all four preamplifiers used in our detection system.

The amplitude of the signal output (V) generated from the preamplifier can be calculated

as:

$$V = Q/C \qquad (2)$$

where Q is the induced charge on the electrodes and C is the total capacitance including the detector capacitance, feedback capacitance (CF), and any stray capacitance. In our previous measurements, to increase the preamplifier signal amplitude as much as possible, the capacitor was not populated on the board. The internal feedback capacitance in the preamplifier was reported to be 0.25 pF. Although no feedback capacitor was used, there is still a stray capacitance due to unused surface-mount pad for CF on the board. To reduce this stray capacitance and enhance the signal amplitude, this trace was removed from the circuit. Figure 4-6 shows the test preamplifier board before and after this modification.

After removing this trace on all preamplifier test boards, ^{137}Cs was again placed at the top of the gas cell and the coincidence energy spectra from CZT1 and CZT2 were collected. The results are shown in Figure 4-7.

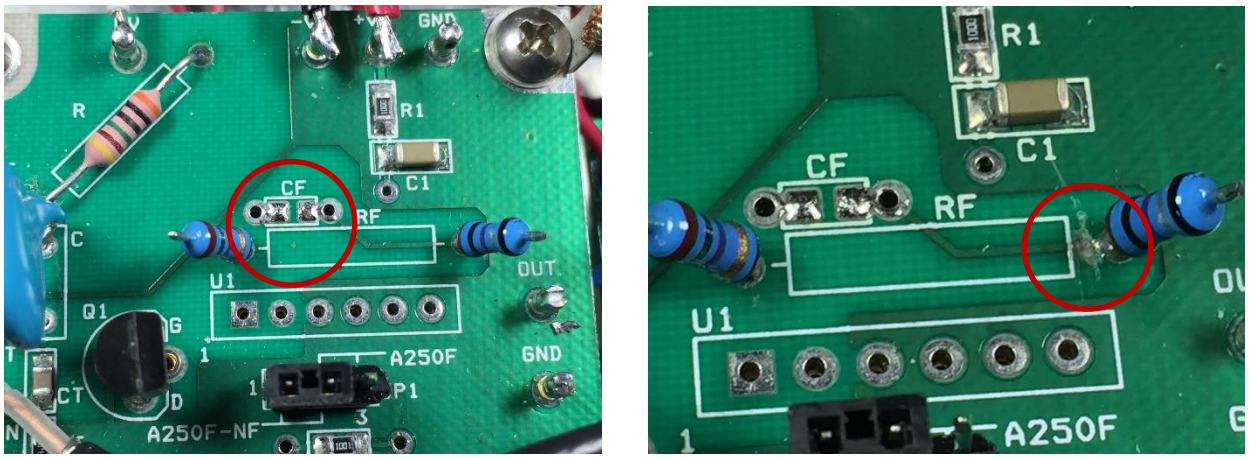

Figure 4-6. Red circle in the left picture shows the pads of feedback capacitor (CF) on the original preamplifier test board. Red circle in the right picture shows disconnected trace to CF on the preamplifier test board.

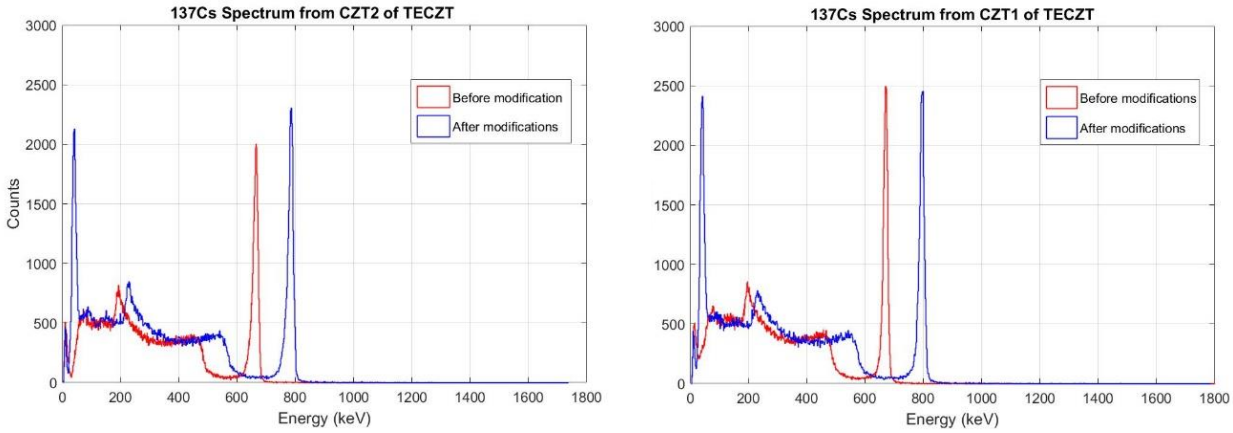

Figure 4-7. Energy spectrum from 662 keV of ^{137}Cs in CZT1 and CZT2 detectors before and after modifications in the electronics and FPGA firmware.

It can be observed that after these modifications, there are 17% and 15% channel shifts (to higher channels) in 662 keV photopeak centroid channel in CZT1 and CZT2 detectors, respectively. The 30 keV X-ray photopeak is now visible in these spectra, as well.

4.1.3.2 FPGA Firmware Modifications

We also replaced the fast trigger filter with a longer filter in FPGA device to have a better discrimination between the low-energy-triggered events and noise-triggered events. In our previous measurements, a triangular filter with a peaking time of 100 nsec was used to trigger the system. We replaced this filter with a 300 nsec trapezoidal filter.

Figure 4-7 shows the energy spectrum from 662 keV in CZT1 and CZT2 detectors before and after FPGA frimware modification as well. This figure shows that after this modification, our detection system is now able to detect 30 keV X-rays.

4.2 Radioxenon Measurements

^{131m}Xe, ^{133m}Xe, ^{133}Xe and ^{135}Xe were produced by activating stable and enriched ^{130}Xe, ^{132}Xe and ^{134}Xe in the Thermal Column of our TRIGA reactor. Figure 4-8 (a) shows the^{130}Xe, ^{132}Xe, and ^{134}Xe vessels.

(a)

(b)

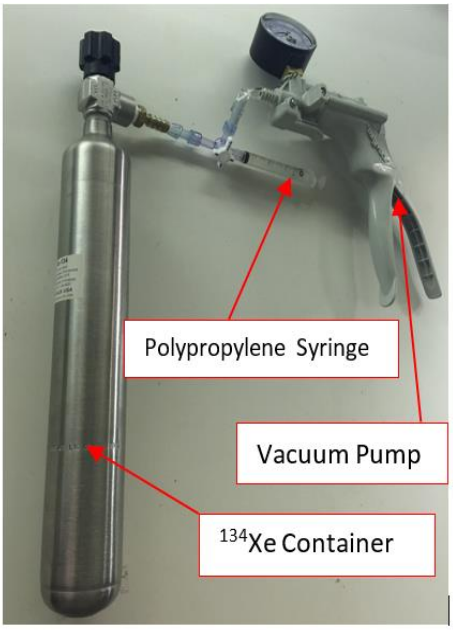

Figure 4-8. (a) Stable xenon gas vessels bought from ISOFLEX Company [88]. (b) Transferring of the stable xenon gases to the polypropylene syringe to be placed in thermal column of the OSU's TRIGA reactor for activation and producing radioxenons of interest.

A volume of 3 mL of stable and highly enriched (>99%) of each sample was first drawn into a polypropylene syringe using a simple hand-pumping system. The polypropylene syringe was chosen because of its low activity after neutron irradiation.

The vacuum/pressure pump was first used to evacuate any existing air in the tube between the gas vessel and the syringe. Then the stable xenon gas was transferred from the gas vessel to

the polypropylene syringe as shown in Figure 4-8 (b).

The syringe was then placed in the Thermal Column of the OSU TRIGA reactor with a flux of ~$7x10^{10}$ n/cm^2.s for several hours. Table 4-3 shows the resulting activity for each radioxenon.

It should be mentioned that the irradiation and cooling of ^{130}Xe and ^{132}Xe were carried out with some time intervals meaning that samples were irradiated for several hours, then TRIGA reactor was shut down overnight and irradiation was continued again the next day.

The activated xenon gas was then injected into the detector gas cell following several hours of cooling time. Figure 4-9 shows the injection of ^{133}Xe to the detector gas cell which is inside the detector housing.

Table 4-3. Neutron irradiation time and resulting activities for ^{130}Xe, ^{132}Xe and ^{134}Xe irradiated in the Thermal Column of the Oregon State University TRIGA reactor.

Stable Xenon isotope	**Irradiation time (hrs)**	**Resulting activities (µci)**
^{134}Xe	7	0.35 (^{135}Xe)
^{130}Xe	25	0.44 (^{131m}Xe)
^{132}Xe	36	0.28 (^{133m}Xe)
^{132}Xe	36	0.98 (^{133}Xe)

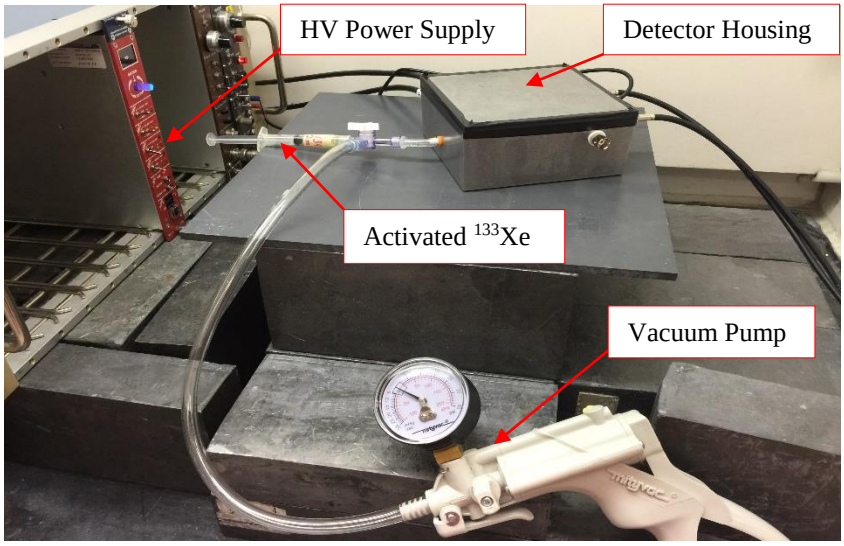

Figure 4-9. Injection of ^{133}Xe to the detector gas cell which is inside the detector housing.

4.2.1 ^{135}Xe Mesurements

Initial radioxenon measurements were performed with ^{135}Xe. Activated xenon gas was injected into the detector gas cell following a cooling time of about 17 hours.

Before starting data collection, the FPGA firmware was set to coincidence mode, in which only coincidence events can trigger the TECZT system. A 2-D coincidence energy spectrum from ^{135}Xe collected by the TECZT detector is depicted in Figure 4-10.

The horizontal axis represents energy absorption in CZT1 and the vertical axis represents energy absorption in CZT2

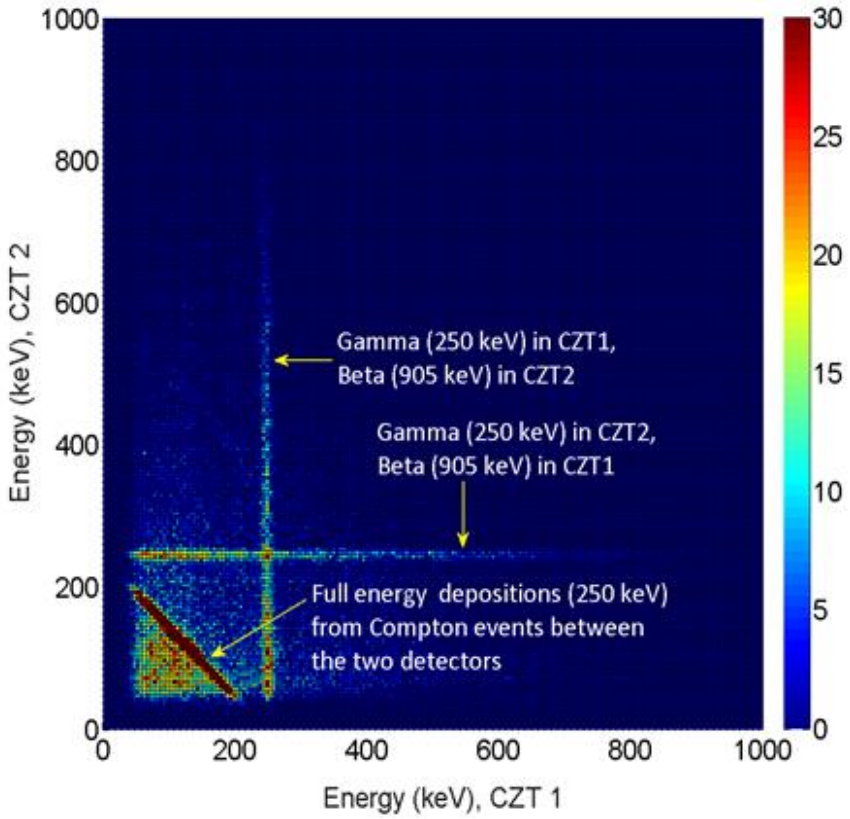

Figure 4-10. 2-D coincidence energy histogram from ^{135}Xe collected by TECZT and DPP2.

As can be seen, beta-gamma coincidence events from ^{135}Xe are dominated by two crossing lines at 250 keV extending from zero to the maximum energy of the beta distribution (905 keV) in one detector and a constant 250 keV energy (gamma-ray photopeak) in the other detector. A diagonal line in this 2-D energy spectrum indicates full energy depositions from Compton events between the two detectors. Events on this line have summation energy equal to the energy of gamma ray emitted from ^{135}Xe (250 keV). This is an indication of the proper functioning of the coincidence mode in the TECZT detector when ^{135}Xe is injected into the gas cell.

Figure 4-11 shows the 2-D energy spectrum when the FPGA's firmware was set to the free

running mode. In this mode, regardless of arrival times, all the events were collected.

Two spectral differences between the coincidence and free-running modes can be identified by comparing Figure 4-10 and Figure 4-11. First, in Figure 4-11, the 250 keV lines extend to energies beyond the maximum energy of the beta particles (905 keV), which is to be expected since in free running mode the two particles can be absorbed in a single detector. Second, the diagonal energy line in Figure 4-10 generated by Compton scatter events between the two detectors is not present in the free running spectrum in Figure 4-11 since the probability of capturing coincidence events in the free running mode is very low.

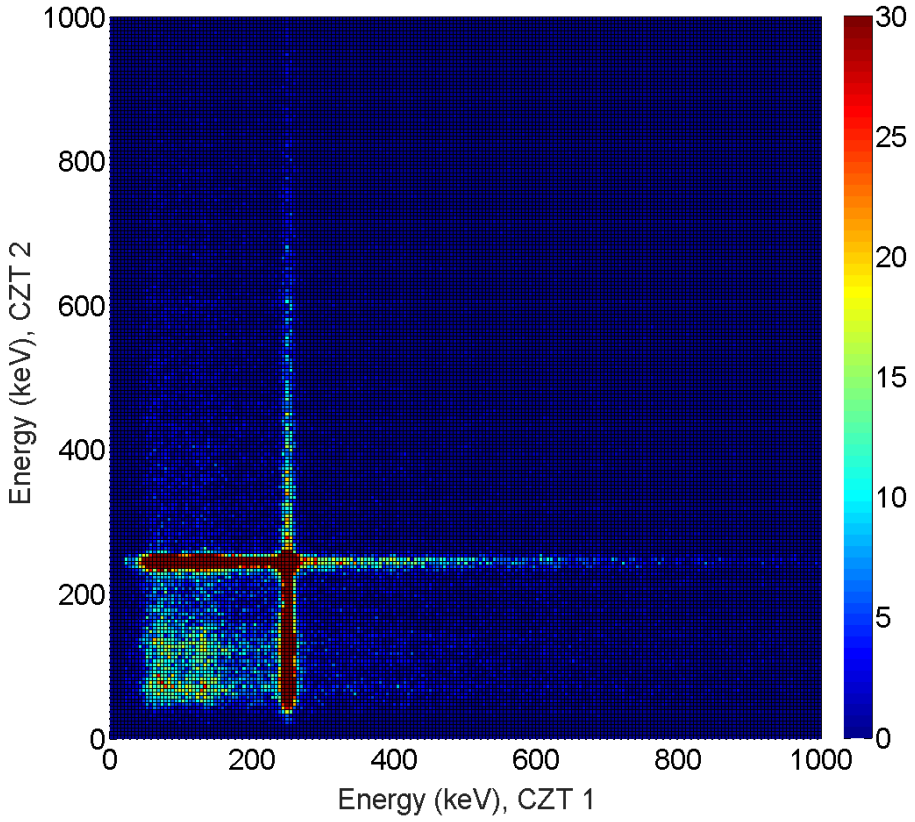

Figure 4-11. 2-D energy histogram from ^{135}Xe collected by TECZT and DPP2 in free running mode (non-coincidence).

Figure 4-12 shows the energy spectrum of ^{135}Xe in each CZT detector when the system was set to the coincidence mode. In both spectra, the 250 keV photopeak is superimposed on the beta distribution which extends up to the maximum beta energy of 905 keV. The energy resolution of the 250 keV photopeak was measured to be 4.4% and 4.7% FWHM for CZT 1 and CZT 2, respectively.

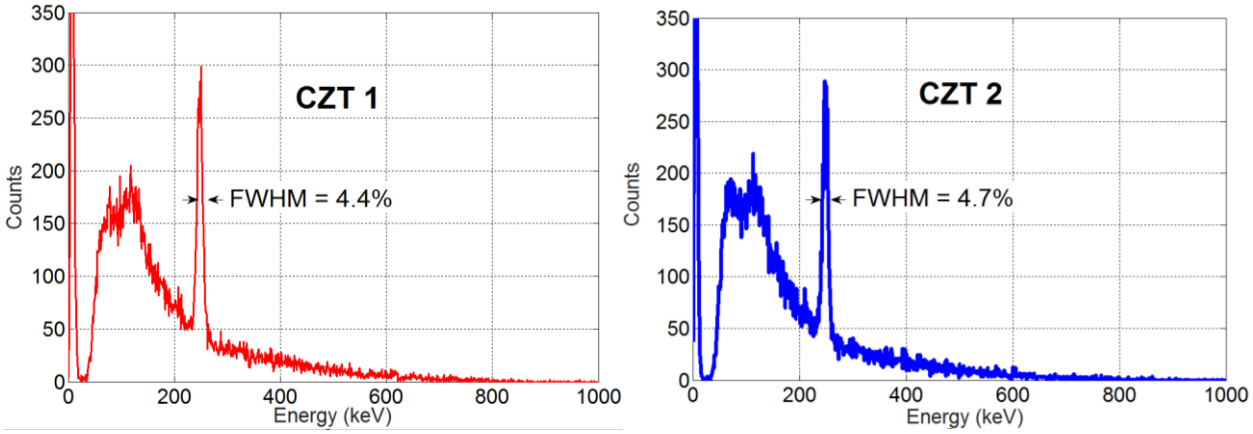

Figure 4-12. Energy histogram (in coincidence mode) for each CZT detector from ^{135}Xe.

4.2.2 ^{133}Xe and ^{133m}Xe Measurements

^{133}Xe emits beta particles (E_{max}=346 keV) in coincidence either with 81 keV gamma-ray (~37%) or with 31 keV X-ray and 45 keV conversion electrons (~47%). ^{133m}Xe emits 31 keV X-rays in coincidence with 199 keV conversion electrons.

The 2-D beta-gamma coincidence energy spectrum from ^{133}Xe and ^{133m}Xe measured by our CZT-based detection system is shown in Figure 4-13. The horizontal axis represents energy

absorption in CZT1 and the vertical axis represents energy absorption in CZT2. As it can be seen in this Figure, 31 keV X-ray and 81 keV gamma-ray forming bands of coincident events with betas are clearly populated and extended up to the maximum energy of beta particles from ^{133}Xe (E_{max} = 346 keV).

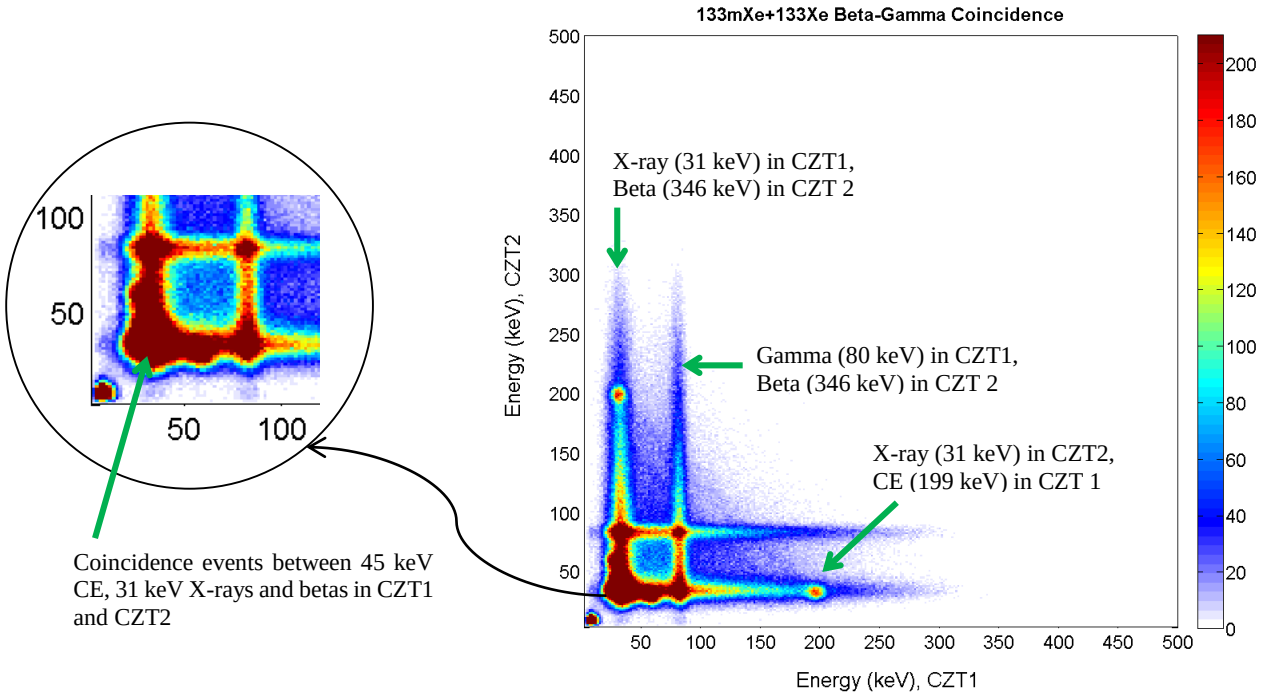

Figure 4-13. 2-D beta-gamma coincidence energy spectrum from ^{133m}Xe + ^{133}Xe collected by our TECZT detection system.

The presence of ^{133m}Xe ($t_{1/2}$=2.19 days) in the injected sample can be confirmed by observing the populated area from conversion electrons on 31 keV X-ray line at about 199 keV in both CZT detectors. Another important feature of this spectrum is the extended 31 keV line to higher energies compared with 80 keV line. This represents the triplet coincidence between

31 keV X-rays, 45 keV conversion electrons and 346 keV betas from ^{133}Xe.

It should be mentioned that in this spectrum, events below about 10 keV are from coincidence events due to electrical noise detected in both detectors.

Figure 4-14 shows coincidence energy deposition in each CZT detector separately. As can be seen, three peaks are clearly observable in these spectra which are superimposed on the beta spectrum; 31 keV and 81 keV peaks from X-rays and gamma rays, respectively, and a peak at the very end represents 199 keV conversion electrons. The energy resolution (FWHM) for 31 keV and 81 keV peaks were measured to be 48.2% and 12.5%, respectively.

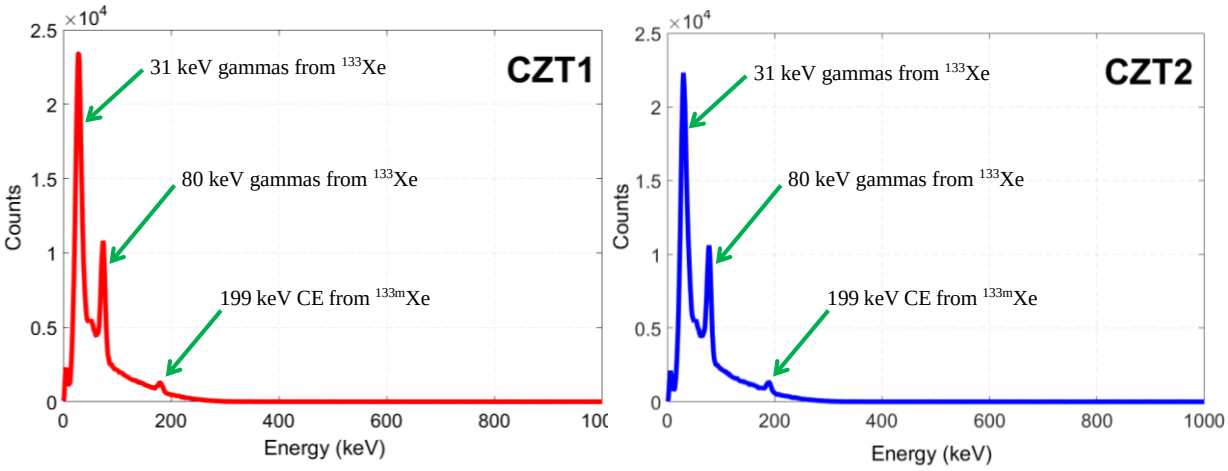

Figure 4-14. Energy spectrum (in coincidence mode) in each CZT detector from ^{133m}Xe and ^{133}Xe.

4.2.3 ^{131m}Xe Measurements

^{130}Xe was activated in our TRIGA reactor to produce ^{131m}Xe and was injected into the gas cell of our detector. Before the injection of ^{131m}Xe into the TECZT, its gas cell was evacuated

several times to empty any remaining ^{133}Xe from previous measurements.

^{131m}Xe emits 31 keV X-rays in coincidence with 129 keV conversion electrons. The 2-D beta-gamma coincidence energy spectrum from ^{131m}Xe measured by our CZT-based detection system is shown in Figure 4-15. Two crossing lines appear at 31 keV which extend up to 129 keV indicating coincidence events between 31 keV X-rays and 129 keV conversion electrons. Ideally, there should only be two populated regions in the 2-D plot showing coincidence emissions of 31 keV X-rays and 129 keV conversion electrons. However, CZT is a high-Z material and there is a high chance of backscattering from CZT surfaces for high-energy electrons. Because of the high backscattering probability, some conversion electrons may only release part of their energy in CZT detectors. Therefore, instead of a confined region around 129 keV, a line starts from the threshold energy (~20 keV) and extends up to 129 keV representing partial energy absorptions from conversion electrons.

Two small regions also appear at approximately 158 keV, representing conversion electrons from 158 keV and 159 keV. Due to the small decay probability of these conversion electrons (14.0% and 15.1%) these regions are not densely populated. A region of coincidence events also connects the 129 keV regions between the two detectors. This region is a result of the backscattering of conversion electrons from one CZT and their absorption in the other.

Figure 4-16 shows energy deposition in each CZT detector separately. As can be seen, three peaks are visible in these spectra, 31 keV and 129 keV from X-rays and conversion electrons and the peak at the very end represents 158+159 keV conversion electrons. The energy resolution (FWHM) for 31 keV and 129 keV peaks was measured to be 41.9% and 10.1%,

respectively.

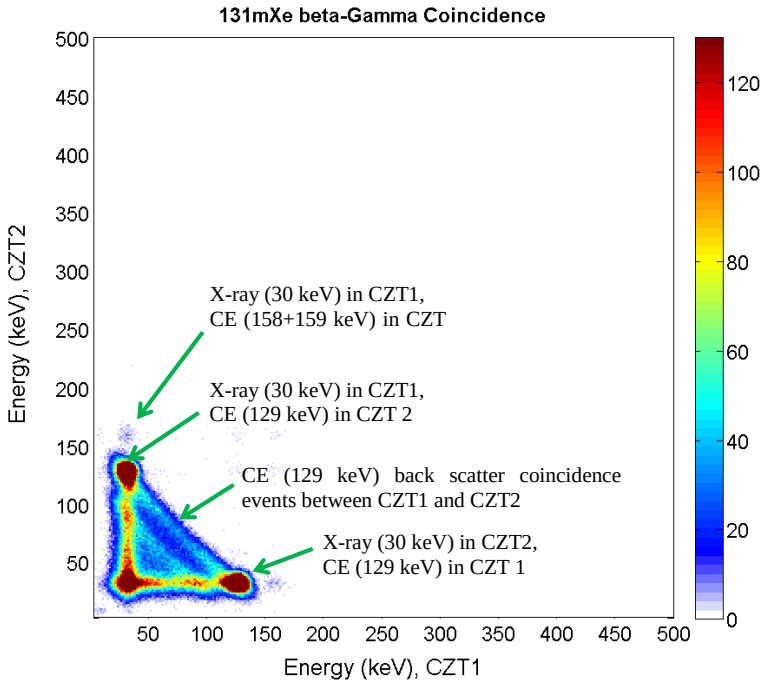

Figure 4-15. 2-D beta-gamma coincidence energy spectrum from ^{131m}Xe collected by our TECZT detection system.

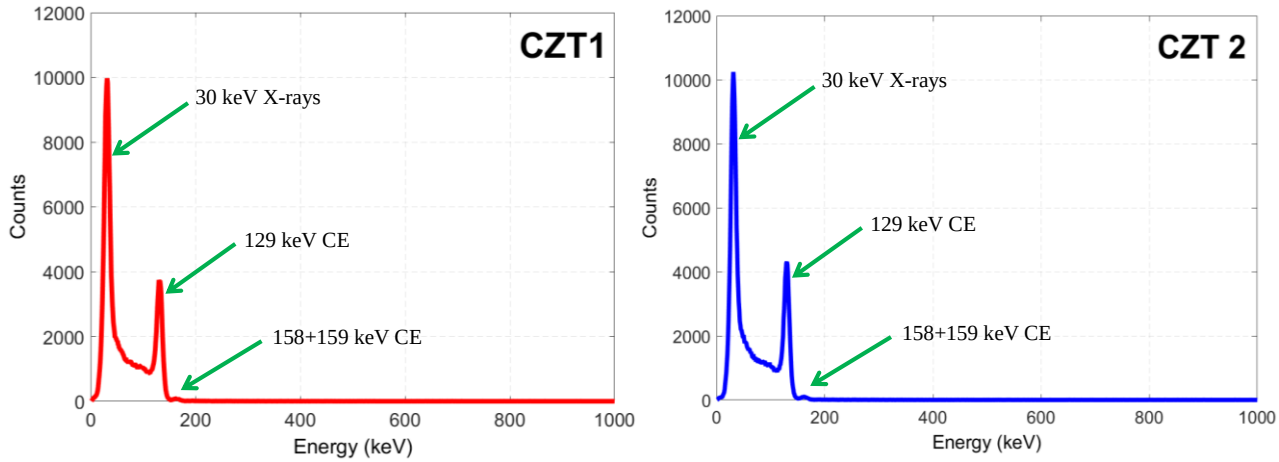

Figure 4-16. Energy histogram (in coincidence mode) in each CZT detector from ^{131m}Xe.

4.3 Energy Resolution and Background Count Rate

Energy resolutions and background count rates from TECZT and other radioxenon detectors have been compared in Table 4-4. Measurement results, listed in this table, show that for all the photon energies except the 31 keV X-ray, the TECZT detector demonstrated better energy resolution compared with other available beta-gamma coincidence-based radioxenon detection systems, a direct result of using CZT detectors instead of scintillators. The 31 keV X-rays do not show better energy resolution due to the noise from the TECZT prototype electronics. The noise can be mitigated by integrating the preamplifier and subtraction circuit onto one compact PCB. In addition, the background count rate for both total and coincidence events is significantly lower compared to the other detection systems.

Table 4-4. Energy resolution and background count rates in TECZT detection system and other radioxenon detection systems.

	Gamma Energy (keV)	**TECZT (this work)**	**WASPD** [34]	**Phoswich** [34]	**SAUNA** [89],[7]	**ARSA** [7],[90]	**BGW** [4],[91]
Energy Resolution (FWHM, %)	31 (^{133}Xe)	**48.2**	47.7	46	23-30	32	18
	80 (^{133}Xe)	**12.5**	27.6	24	13	25	13
	88 (^{109}Cd)	**11.2**	31.5	25	14	NA	14
	122 (^{57}Co)	**6**	NA	24	NA	22	13
	662 (^{137}Cs)	**2.1**	13.6	8.9	7.3	12	8.7
	250 (^{135}Xe)	**4.4**	19.3	13	NA	9.6	NA
Background Rate (counts/s)	Total (all events)	**0.2**	1.26	3.29	7.5-12	30	5.5
	Coincidence Events	**0.0036**	0.02	0.06	0.03	0.1	0.025

4.4 Estimate of Minimum Detectable Concentration (MDC)

Radioxenon detection systems must be sensitive enough to detect trace amount of xenon gases to be eligible candidates for integration into the International Monitoring System (IMS). IMS requires that the MDC of all radioxenon detection systems must be less than or equal to 1 mBq/m^3 for ^{133}Xe [92].

In general, the MDC can be calculated using the following equation:

$$MDC\left(\frac{mBq}{m^3 air}\right) = \left[\frac{2.71+4.65\sigma_0}{\varepsilon_\beta \epsilon_\gamma \beta_{BR} \gamma_{BR}}\right]\left[\frac{\lambda^2}{(1-exp(-\lambda T_c))(-\lambda T_p)(1-exp(-\lambda T_A))}\right]\left[\frac{T_C * 1000}{V_{air}}\right] \quad (3)$$

Where:

σ_0: [Background counts + $(\sigma_{Interferences})^2$]$^{1/2}$

ε_β: β Efficiency

ε_γ : γ Efficiency

β_{BR}: β Branching Ratio

γ_{BR}: γ Branching Ratio

λ: Decay Constant (s^{-1})

T_c: Xenon Collection Time (s)

T_p: Processing Time of Gas (s)

T_A: Acquisition Time of Counts (s)

V_{air}: Sampled Air Volume (m^3)

The first term in equation (3) takes into account the traditional sensitivity expression using the standard deviation of the measured background and interference counts (σ_0) with the beta and gamma detector efficiencies and branching ratios respectively (ε_β , ε_γ , β_{BR}, γ_{BR}). The second term accounts for the decay of the xenon isotope during the collection time T_c, the processing time T_P, and the nuclear acquisition time T_A using the decay constant for the specific isotope λ. Finally, the third term accounts for the volume of air measured V_{Air} and the conversion to milliBecquerels.

Several factors can affect the MDC of radioxenon detection systems such as the background counts and memory effect from the previous sample measurements. Background itself is affected by both radioxenon itself for the 30 keV region and ^{222}Rn daughters (^{214}Pb and ^{214}Bi) for the 81 keV and 250 keV regions. Therefore, to accurately calculate the MDC for a given radixenon isotope in a specific detector a careful accounting of the various backgrounds and interference terms is necessary.

In general σ_0 in the MDC equation can be calculated using [93]:

$$\sigma_0 = \sqrt{BckCnt_{total} + \sigma^2_{BckCnt} + InterferenceCnt + \sigma^2_{InterferenceCnt} + MemoryCnt + \sigma^2_{MemoryCnt}} \quad (4)$$

In this work, $BckCnt_{total}$ in the coincidence region of interest (ROI) was calculated using the method described in [94]. Using this method $BckCnt_{total}$ can be defined as the product of four terms:

$$BckCnt_{total} = [S_{Bck(ROI)}][CTW]\left[\frac{T_A}{T_B}\right][N_{cp}] \quad (5)$$

1- S $_{Bck(ROI)}$: Summation of the background counts in CZT1 and CZT2 for each ROI

2- CTW: The Coincidence Time Window =1 μs for TECZT

3- T_A: Acquisition Time of Counts= 24 hrs

3- T_B: The Background Measurement Time =48 hrs for TECZT

4- N_{cp}: Number of Coincidence Permutations = 2 for TECZT

To find the associated background counts in CZT1 and CZT2, a 48-hour background measurement was performed in coincidence mode. The ROI for the radioxenons were defined based on their coincidence decay emission and using 2 times the FWHM of the energy resolution for that ROI. For radioxenons with multiple ROIs, the background counts in all these ROI were summed together.

To estimate MDC for each xenon radioisotopes, the following assumptions and conditions were considered:

(1) For simplicity, background counts due to interferences, such as those from radon daughters and their associated variance, were ignored ($InterferenceCnt + \sigma^2_{InterferenceCnt} = 0$);

(2) Since we anticipate that our detection system doesn't show a significant memory effect, counts related to memory effect and its associated variance were also ignored $\left(MemoryCnt + \sigma^2_{MemoryCnt} = 0\right)$;

(3) Typical values from the ARSA system [4] for xenon collection time (T_C = 8 h),

processing time (T_p =5.45 h), and acquisition time (T_A = 24 h) were used;

(4) The products of the branching ratios (β_{BR}. γ_{BR}) were taken from values indicated by an "a" superscript in Table 2-1 [3];

(5) The typical air volume V_{air} (20 m^3) is given by the Xe collection system which is a distinctive value in monitoring stations and independent of the detector [94]. However, this parameter was adjusted by a factor equivalent to the ratio of active gas volume in the TECZT and ARSA (1 cm^3/6.14 cm^3) to account for differences in active gas volume in the two detectors. Therefore a value of 3.26 m^3 was used for V_{air} in the MDC formula;

(6) The beta-gamma coincidence detection efficiencies ($\varepsilon_\beta.\varepsilon_\gamma$) of the TECZT for each ROI were estimated by performing a Monte Carlo analysis using the MCNP6 code (Table 4-5).

It should be mentioned that even though ^{133}Xe has two signatures (in 31 keV and 81 keV X-ray/gamma-ray lines), a single MDC was calculated by combining the two MDCs using the following equation which is the weighted average of the errors and is dominated by the smaller of the two MDC calculations [93]:

$$^{133}Xe_{MDC}\left(\frac{mBq}{m^3 air}\right) = \sqrt{\frac{1}{(^{133}Xe_{MDC}^{31keV})^{-2}+(^{133}Xe_{MDC}^{81keV})^{-2}}}. \quad (6)$$

The resulting MDC values using these assumptions are presented in Table 4-5.

Table 4-5. Calculated MDC values for the four xenon radioisotopes using the TECZT detector

Isotope	**B-γ coincidence ROI** (see Table 2-1)	γ_{BR}. β_{BR} (see Table 2-1)	$\varepsilon_\beta.\varepsilon_\gamma$ [MCNP]	**MDC** (mBq/m^3)
^{131m}Xe	31 keV X-rays and 129 keV CE	0.561	0.013	1.45±0.06
^{133m}Xe	31 keV X-rays and 199 keV CE	0.584	0.011	1.85±0.04
^{133}Xe	81 keV gamma and 346 beta	0.372	0.023	1.26±0.09
	31 keV gamma and 346 beta	0.489	0.039	0.57±0.09
^{135}Xe	250 keV gamma and 910 keV beta	0.9	0.032	1.47±0.05

Figure 4-17shows a comparison between the MDCs reported from WASPD [34], SAUNA [46], ARSA [95] , SPALAX [96], 24-PIN Diode array [45] and the MDCs obtained in this work using TECZT. The dashed red line in this figure shows the MDC requirement set by the IMS for ^{133}Xe. In addition, Figure 4-17 shows the estimated MDCs of the SECZT (Six Element CZT detection system) based on the results of the TECZT system. The estimated MDCs of the SECZT system, less than 1 mBq/m^3 for all radioxenons, are comparable to those of the most sensitive radioxenon detection systems currently available, which is a direct result of the improvement in geometric efficiency compared to the TECZT system.

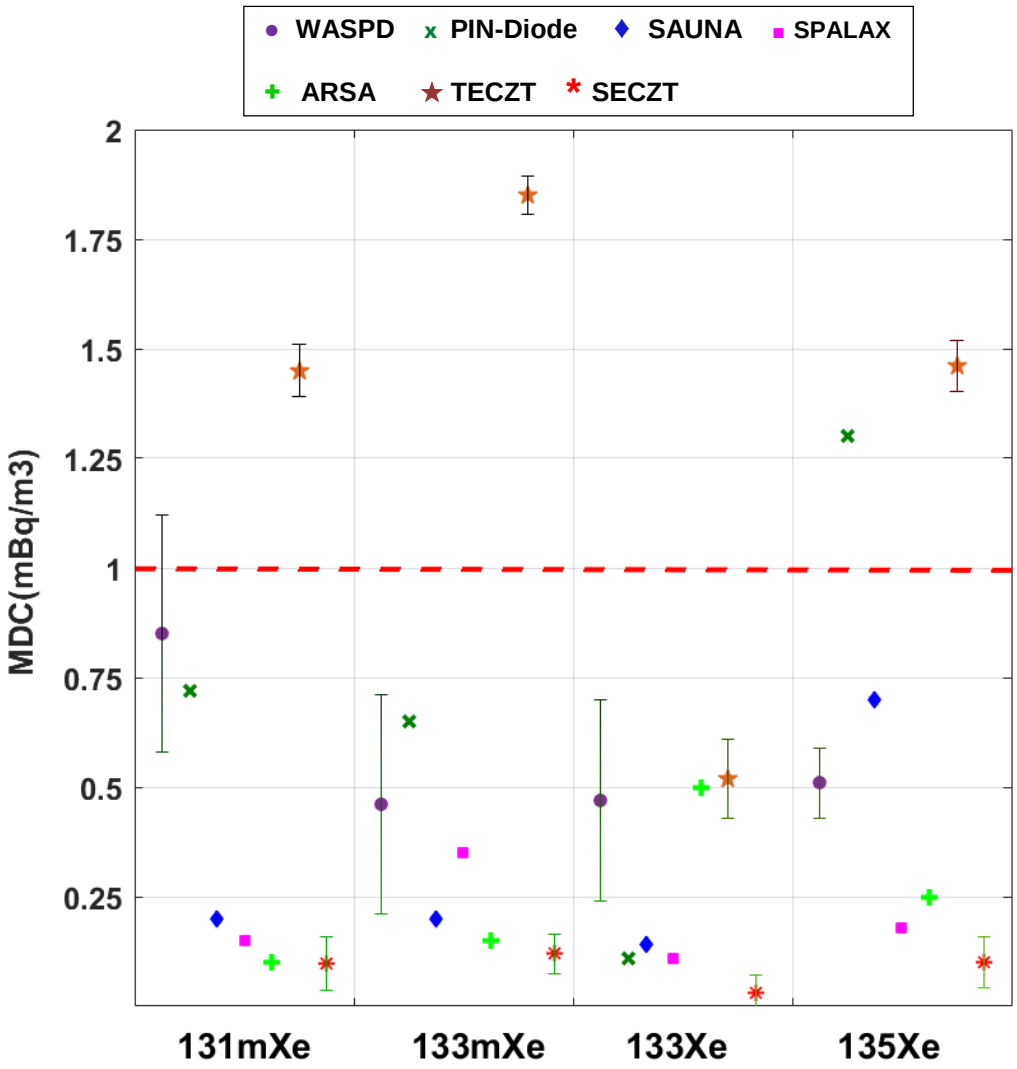

Figure 4-17. MDC comparison of TECZT with other radioxenon detection WASPD, ARSA, SPALAX, and SAUNA, as well as the estimated MDC from the SECZT design. The dashed red line shows the MDC requirement set by the International Monitoring System (IMS) for ^{133}Xe.

One way to improve the MDCs of the CZT-based systems is to use a larger gas cell volume. In future work, 20 x 20 mm^2 CZT crystals may be used in order to accommodate an 8 cm^3 gas cell volume. The increase in gas cell volume (V_{air}) while maintaining a high geometric efficiency will provide a factor of 8 improvement in MDC compared to the current 1 cm^3 gas cell volume. Another way to improve the MDCs of the CZT-based systems is to minimize the conversion

electron backscattering, which can be accomplished by using a low-Z plastic scintillator rather than CZT to detect betas and conversion electrons. The inner surface of the plastic scintillator can be coated with Al_2O_3 to minimize the unwanted memory effect usually seen in plastic scintillators [19], [74].

Yesterday I was clever, so I wanted to change the world;
Today I am wise, so I'm changing myself.
Rumi, 13th century Persian poet

5 Conclusions

5.1 Current Work

The functional radioxenon detector prototype constructed as described herein as well as the characterization of the device fulfills most of the goals of this project and shows that CZT is a very promising material to be used for radioxenon detection in support of the Comprehensive Nuclear Test Ban Treaty.

A two-element CZT detection system was designed, built and characterized to study the response of CdZnTe detectors to xenon radioisotopes through beta-gamma coincidence counting.

This prototype device, namely *Two-Element Coplanar CZT* (TECZT) detection system utilizes two face-to-face coplanar CZT detectors for coincidence detection of beta/conversion electrons and gamma/X-rays.

Coincidence detection was performed in real time in the FPGA. Coincidence events were captured and transferred to the PC when the two detectors are triggered within Coincidence Time Window (CTW), which is adjustable from 0 to 1.275 μs with 5 nsec steps (ADC's sampling period).

TECZT was tested and characterized using radioactive lab sources and radioxenons produced in OSU TRIGA reactor. The detector shows significant improvements in the energy resolution

and background count rates compared to other beta-gamma coincidence detection systems.

Coincidence background count rate for TECZT was measured to be 0.0036 counts/s. Thus, the TECZT can be used in environments where there is high background in the energy range of interest.

From our measurements with ^{137}Cs lab source, we achieved an energy resolution of 2.1% FWHM from 662 keV photopeak. This is much better than the resolution obtained from the ARSA (12%) and SAUNA (7.3%) detectors.

Beta-gamma coincidence measurements of ^{131m}Xe, ^{133m}Xe, ^{133}Xe and ^{135}Xe also showed energy resolutions of 48.2% and 12.5% FWHM for 31 and 81 keV photopeak, respectively. The 250 keV photopeak also showed energy resolution of 4.4% FWHM.

The MDCs of the radioxenons of interest for the TECZT were also calculated in this study. The MDC of ^{133}Xe was found to be 0.52 mBq/m^3 which is less than the IMS requirements (1 mBq/m^3). Based on the MDC results of the prototype two-element system, it was found that a 6-CZT design will have MDCs of less than 1 mBq/m^3 for all radioxenons. For ^{133}Xe the MDC was estimated to be 0.03 mBq/m^3 which is better than the MDC of the available radioxenon detection systems.

5.2 Future Work

Further improvements to the general design can be made by adding 4 CZT crystals to the current design and using a larger gas cell volume. In addition, using a plastic scintillator material to detect betas and conversion electrons in order to reduce conversion electron backscattering can improve the current device.

5.2.1 Increasing Geometric Efficiency of the TECZT

Our estimation shows that by increasing the number of CZT crystals to 6, the geometric efficiency of the TECZT detection system can be enhanced by a factor of 15 to be about 83%. This enhancement will lead to the improvement of the MDC of all radioxenons (less than 1 mBq/m^3). As a result, MDCs will be comparable to those of the most sensitive radioxenon detection systems currently available. In future work, the gas cell of the current system will be modified to accommodate 6 CZT crystals. Another improvement in the TECZT detection system can be also made by using a larger gas cell volume. In future work, 20 x 20 mm^2 CZT crystals may be used in order to accommodate an 8 cm^3 gas cell volume. The increase in gas cell volume while maintaining a high geometric efficiency will provide a factor of 8 improvement in MDC compared to the current 1 cm^3 gas cell volume.

5.2.2 Minimizing Conversion Electrons Backscattering

The 2-D beta-gamma coincidence energy spectrum obtained for ^{131m}Xe shows a high probability of conversion electrons backscattering from CZT surfaces. Ideally, conversion electrons must deposit their full energies in CZT crystals. However, CZT is a high-Z material and there is a high chance of backscattering from CZT surfaces for high-energy electrons. Because of this, some conversion electrons may only release part of their energy in CZT detectors. Therefore, instead of a confined region for conversion electrons in the 2D beta-gamma coincidence spectrum, there can be a spread of energy representing partial energy absorptions from conversion electrons. This can affect the sensitivity of TECZT and hence degrade the MDC

of the system.

To avoid this issue and increase the sensitivity of this detection system a separate low-Z material can be used to detect beta and conversion electrons. Plastic scintillators are a good candidate for this purpose. However, to minimize the memory effect of the system which arises from xenon diffusion to the plastic it should be coated with Al_2O_3.

5.2.3 Minimizing Electronic Noises

To further improve the CZT-base radioxenon detection systems, the electronic noises can be mitigated by integrating the preamplifier and subtraction circuit onto one compact PCB or using proximity charge sensing method [97] where instead of directly deposited coplanar patterns, they are deposited on the PCB board. Using proximity charge sensing method, all electronic components can be placed in close proximity to the CZT crystals. Therefore, electronic noises associated with long leads between the anodes and the preamplifiers can be addressed.

Proximity charge sensing method also reduces the leakage current associated with directly deposited electrodes on the crystal surface and therefore improve the energy resolution of the system. It also promises the compactness of the system and simplifies the fabrication process by eliminating the need to directly deposit electrodes on the CZT crystals.

Finally, it reduces the cost of the whole system which is one of the main consideration in most research projects.

6 Bibilography

[1] C. T. B. Treaty, “Chairman’s Draft Text of the Comprehensive Test Ban Treaty,” *Arms Control Today*, 1996.

[2] “The Global Verification Regime and the International Monitoring System.” Preparatory Commission for the Comprehensive Nuclear-Test-Ban Treaty Organization (CTBTO), 2001.

[3] M. Auer, T. Kumberg, H. Sartorius, B. Wernsperger, and C. Schlosser, “Ten Years of Development of Equipment for Measurement of Atmospheric Radioactive Xenon for the Verification of the CTBT,” *Pure Appl. Geophys.*, vol. 167, no. 4–5, pp. 471–486, May 2010.

[4] J. I. McIntyre, K. H. Abel, T. W. Bowyer, J. C. Hayes, T. R. Heimbigner, M. E. Panisko, P. L. Reeder, and R. C. Thompson, “Measurements of ambient radioxenon levels using the automated radioxenon sampler/analyzer (ARSA),” *J. Radioanal. Nucl. Chem.*, vol. 248, no. 3, pp. 629–635, 2001.

[5] A. Ringbom, T. Larson, A. Axelsson, K. Elmgren, and C. Johansson, “SAUNA—a system for automatic sampling, processing, and analysis of radioactive xenon,” *Nucl. Instrum. Methods Phys. Res. Sect. Accel. Spectrometers Detect. Assoc. Equip.*, vol. 508, no. 3, pp. 542–553, Aug. 2003.

[6] V. V. Prelovskii, N. M. Kazarinov, A. Y. Donets, V. Y. Popov, I. Y. Popov, and N. V. Skirda, “The ARIX-03F mobile semiautomatic facility for measuring low concentrations of radioactive xenon isotopes in air and subsoil gas,” *Instrum. Exp. Tech.*, vol. 50, no. 3, pp. 393–397, May 2007.

[7] J.-P. Fontaine, F. Pointurier, X. Blanchard, and T. Taffary, “Atmospheric xenon radioactive isotope monitoring,” *J. Environ. Radioact.*, vol. 72, no. 1–2, pp. 129–135, Jan. 2004.

[8] T. W. Bowyer, S. R. Biegalski, M. Cooper, P. W. Eslinger, D. Haas, J. C. Hayes, H. S. Miley, D. J. Strom, and V. Woods, “Elevated radioxenon detected remotely following the Fukushima nuclear accident,” *J. Environ. Radioact.*, vol. 102, no. 7, pp. 681–687, Jul. 2011.

[9] F. Xie, X. He, W. Jiang, X. Zhang, Q. Shi, S. Wu, L. Liu, C. Zhang, and L. Chen, “Development of a radioxenon measurement system and its application in monitoring Fukushima nuclear accident,” *Radiat. Phys. Chem.*, vol. 97, pp. 85–89, Apr. 2014.

[10] B. Orr, M. Schöppner, R. Tinker, and W. Plastino, “Detection of radioxenon in Darwin, Australia following the Fukushima Dai-ichi nuclear power plant accident,” *J. Environ. Radioact.*, vol. 126, pp. 40–44, Dec. 2013.

[11] W. Shilian, L. Qi, M. Qinghua, C. Zhanying, Z. Yungang, L. Huijuan, J. Huaimao, C. Yinzhong, L. Shujiang, Z. Xinjun, F. Yuanqing, W. Ling, and L. Yun, “Radioxenon monitoring in Beijing following the Fukushima Daiichi NPP accident,” *Appl. Radiat. Isot.*, vol. 81, pp. 344–347, Nov. 2013.

[12] A. Ringbom, K. Elmgren, K. Lindh, J. Peterson, T. W. Bowyer, J. C. Hayes, J. I. McIntyre, M. Panisko, and R. Williams, “Measurements of radioxenon in ground level air in South Korea following the claimed nuclear test in North Korea on October 9, 2006,” *J. Radioanal. Nucl. Chem.*, vol. 282, no. 3, pp. 773–779, Dec. 2009.

[13] P. R. J. Saey, M. Bean, A. Becker, J. Coyne, R. d’Amours, L.-E. De Geer, R. Hogue, T.

J. Stocki, R. K. Ungar, and G. Wotawa, “A long distance measurement of radioxenon in Yellowknife, Canada, in late October 2006,” *Geophys. Res. Lett.*, vol. 34, no. 20, Oct. 2007.

[14] A. Becker, G. Wotawa, A. Ringbom, and P. R. J. Saey, “Backtracking of noble gas measurements taken in the aftermath of the announced October 2006 event in North Korea by means of the PTS methods in nuclear source estimation and reconstruction,” *Geophys. Res. Abstr.*, vol. 10, no. EGU200-A-11835, 2008.

[15] G. Wotawa, “Meteorological analysis of the detection of xenon and barium/lanthanum isotopes in May 2010 in Eastern Asia,” *J. Radioanal. Nucl. Chem.*, vol. 44, no. 20, 2013.

[16] C. M. Wright, “Low-Yield Nuclear Testing by North Korea in May 2010: Assessing the Evidence with Atmospheric Transport Models and Xenon Activity Calculations,” *Sci. Glob. Secur.*, vol. 21, no. 1, pp. 3–52, Jan. 2013.

[17] A. Ringbom, A. Axelsson, M. Aldener, M. Auer, T. W. Bowyer, T. Fritioff, I. Hoffman, K. Khrustalev, M. Nikkinen, V. Popov, Y. Popov, K. Ungar, and G. Wotawa, “Radioxenon detections in the CTBT international monitoring system likely related to the announced nuclear test in North Korea on February 12, 2013,” *J. Environ. Radioact.*, vol. 128, pp. 47–63, Feb. 2014.

[18] K. Kutsher, “Atmospheric Transport Modeling of Radio-Xenon Detections Possibly Related to the Announced Nuclear Test in North Korea on February 12, 2013,” 2014.

[19] L. Bläckberg, T. Fritioff, L. Mårtensson, F. Nielsen, A. Ringbom, H. Sjöstrand, and M. Klintenberg, “Memory effect, resolution, and efficiency measurements of an Al2O3 coated plastic scintillator used for radioxenon detection,” *Nucl. Instrum. Methods Phys. Res. Sect. Accel. Spectrometers Detect. Assoc. Equip.*, vol. 714, pp. 128–135, Jun. 2013.

[20] S. N. Kile, “Nuclear arms control and non-proliferation,” *SIPRI Yearb. 2004 Armaments Disarm. Int. Secur.*, pp. 617–619, 2011.

[21] B. S. Loeb, “The Limited Test Ban Treaty,” *U. S. St Martins Press*, 1991.

[22] G. P. Shultz, W. J. Perry, H. A. Kissinger, S. Nunn, and others, “A world free of nuclear weapons,” *Wall Str. J.*, vol. 4, p. A15, 2007.

[23] P. Doty, “Strategic Arms Limitation after SALT I,” *Daedalus*, pp. 63–74, 1975.

[24] “https://www.ctbto.org/the-treaty/status-of-signature-and-ratification/,” Feb-2016. .

[25] A. Aust and International Group on Global Security, Eds., *A new look at the Comprehensive Nuclear-Test-Ban Treaty (CTBT)*. Den Haag: Nederlands Instituut of International Relations Clingendael, 2008.

[26] “https://www.ctbto.org/specials/who-we-are/,” Jan-2016. .

[27] “http://www.bgr.bund.de/EN/Themen/Seismologie/__Content_alt/Kernwaffenteststopp_en_alt/kernwaffenteststopp_node_en.html.” .

[28] J. R. Murphy, B. C. Kohl, J. L. Stevens, T. J. Bennett, and H. G. Israelsson, “Exploitation of the IMS and other data for a comprehensive, advanced analysis of the North Korean nuclear tests,” DTIC Document, 2010.

[29] S. J. Gibbons and F. Ringdal, “Seismic Monitoring of the North Korea Nuclear Test Site Using a Multichannel Correlation Detector,” *IEEE Trans. Geosci. Remote Sens.*, vol. 50, no. 5, pp. 1897–1909, May 2012.

[30] M. Zhang and L. Wen, “High-precision location and yield of North Korea’s 2013 nuclear test: NORTH KOREA’S 2013 NUCLEAR TEST,” *Geophys. Res. Lett.*, vol. 40, no. 12, pp. 2941–2946, Jun. 2013.
[31] “http://cvt.engin.umich.edu/,” Jan-2016. .
[32] B. Wernsperger and C. Schlosser, “Noble gas monitoring within the international monitoring system of the comprehensive nuclear test-ban treaty,” *Radiat. Phys. Chem.*, vol. 71, no. 3–4, pp. 775–779, Oct. 2004.
[33] T. W. Bowyer, C. Schlosser, K. H. Aber, M. Auer, J. C. Hayes, T. R. Heimbigner, J. I. McIntyr, M. E. Panisko, P. L. Reeder, H. Satorius, J. Schulze, and W. Weiss, “Detection and analysis of xenon isotopes for the comprehensive nuclear-test-ban treaty international monitoring system,” *J. Environ. Radioact.*, vol. 59, pp. 139–151, 2002.
[34] B. Alemayehu, A. T. Farsoni, L. Ranjbar, and E. M. Becker, “A well-type phoswich detector for nuclear explosion monitoring,” *J. Radioanal. Nucl. Chem.*, vol. 301, no. 2, pp. 323–332, Aug. 2014.
[35] B. Bjurman, L.-E. De Geer, I. Vintersved, A. Rudjord, F. Ugletveit, H. Aaltonen, K. Sinkko, A. Rantavaara, S. Nielsen, A. Aarkrog, and K. Walter, “The detection of radioactive material from a venting underground nuclear explosion,” *J. Environ. Radioact.*, vol. 11 (1), pp. 1–14, 1990.
[36] “Evaluation and compilation of fission product yields.” Los Alamos National Laboratory, LA-UR- 94-3106, ENDF-349, 1995.
[37] “Preparatory commission for the comprehensive nuclear-test-ban treaty organization,” 2016. .
[38] “WOSMIP III - Workshop on Signatures of Medical and Industrial Isotope Production.” Pacific Northwest National Laboratory (PNNL), 2012.
[39] R. W. Perkins and L. A. Casey, “Radioxenons: Their role in monitoring a comprehensive test ban treaty.” Pacific Northwest National Laboratory, 1996.
[40] J. H. Ely, M. W. Cooper, J. C. Hayes, T. R. Heimbigner, J. I. McIntyre, and B. T. Schrom, “Final Technical Report on Radioxenon Event Analysis,” Pacific Northwest National Laboratory (PNNL), Richland, WA (US), 2013.
[41] A. Matthias, “The International Monitoring System noble gas network.” CTBTO Preparatory Comission, 2014.
[42] P. R. J. Saey and L.-E. De Geer, “Notes on radioxenon measurements for CTBT verification purposes,” *Appl. Radiat. Isot.*, vol. 63, no. 5–6, pp. 765–773, Nov. 2005.
[43] J.-P. Fontaine, F. Pointurier, X. Blanchard, and T. Taffary, “Atmospheric xenon radioactive isotope monitoring,” *J. Environ. Radioact.*, vol. 72, no. 1–2, pp. 129–135, Jan. 2004.
[44] Y. V. Dubasov, Y. S. Popov, V. V. Prelovskii, A. Y. Donets, N. M. Kazarinov, V. V. Mishurinskii, V. Y. Popov, Y. M. Rykov, and N. V. Skirda, “The АРИКС-01 Automatic Facility for Measuring Concentrations of Radioactive Xenon Isotopes in the Atmosphere,” *Instrum. Exp. Tech.*, vol. 48 (3), pp. 373–379, 2005.
[45] C. E. Cox, W. Hennig, A. C. Huber, W. K. Warburton, P. M. Grudberg, S. J. Asztalos, H. Tan, and S. Biegalski, “A 24-element Silicon PIN diode detector for high resolution

radioxenon measurements using simultaneous X-ray and electron spectroscopy," in *Nuclear Science Symposium and Medical Imaging Conference (NSS/MIC), 2013 IEEE*, 2013, pp. 1–7.

[46] H. Goha and M. Auer, "1st IMS noble gas system certification_review of certification requirements.," in *In: Proceedings of 2010 INGE workshop (day 2, session 5)*, 2010.

[47] W. Hennig, W. K. Warburton, A. Fallu-Labruyere, K. Sabourov, M. W. Cooper, J. I. McIntyre, A. Gleyzer, M. Bean, P. Korpach, K. Ungar, and others, "Radioxenon measurements with the Phoswatch detector system," *Proc. 2009 Monit. Res. Rev. Ground-Based Nucl. Explos. Monit. Technol. -UR-09-05276*, vol. 2, pp. 641–652, 2009.

[48] A. Ringbom, "Verifying the Comprehensive Nuclear-Test-Ban Treaty by Radioxenon Monitoring," in *AIP Conference Proceedings*, 2005, vol. 769, p. 1693.

[49] "http://www.environnement-sa.com/products-page/en/radionuclide-monitoring-en/automatic-radio-xenon-sampleranalyzer-en/SPALAX-2/," Jan-2016. .

[50] G. Le Petit, C. Jutier, P. Gross, and V. Greiner, "Low-level activity measurement of 131Xem, 133Xem, 135Xe and 133Xe in atmospheric air samples using high-resolution dual X–γ spectrometry," *Appl. Radiat. Isot.*, vol. 64, no. 10–11, pp. 1307–1312, Oct. 2006.

[51] M. W. Cooper, A. J. Carman, J. C. Hayes, T. R. Heimbigner, C. W. Hubbard, K. E. Litke, J. I. McIntyr, S. J. Morris, M. D. Ripplinger, and R. Suarez, "Improved β-γ coincidence detector for radioxenon detection," presented at the 27 Seismic Research Review: Ground-BasedNuclear Explosion Monitoring Technologies.

[52] J. I. McIntyr, "Applied Nuclear Science at Pacific Northwest National Laboratory; The Diverse Work of National Security, International Treaties, and Basic Research." Pacific Northwest National Laboratory (PNNL).

[53] "http://www.SAUNAsystems.se/default.aspx?PID=38," Jan-2016. .

[54] Y. S. Popov, N. M. Kazarinov, V. Y. Popov, Y. M. Rykov, and N. V. Skirda, "Measuring Low Activities of Fission-Product Xenon Isotopes Using the β-γ Coincidence Method," *Instrum. Exp. Tech.*, vol. 48, no. 3, pp. 380–386, 2005.

[55] "https://www.saint-gobain.com/en," Jan-2016. .

[56] J. H. Ely, C. E. Aalseth, and J. I. McIntyre, "Novel beta-gamma coincidence measurements using phoswich detectors," *J. Radioanal. Nucl. Chem.*, vol. 263, no. 1, pp. 245–250, 2005.

[57] J. H. Ely, C. E. Aalseth, J. C. Hayes, T. R. Heimbigner, J. I. McIntyr, H. S. Miley, A. E. Panisko, and M. Ripplinger, "Novel beta-gamma coincidence measurements using phoswich detectors," presented at the 25th Seismic Research Review - Nuclear Explosion Monitoring: Building the Knowledge Base, 2003.

[58] W. Hennig, H. Tan, W. K. Warburton, and J. I. McIntyre, "Digital pulse shape analysis with phoswich detectors to simplify coincidence measurements of radioactive xenon," *Proc. 27th Seism. Res. Rev. Ground-Based Nucl. Explos. Monit. Technol.*, pp. 787–794, 2005.

[59] W. Hennig, Hui Tan, W. K. Warburton, and J. I. McIntyre, "Single-channel beta-gamma coincidence detection of radioactive xenon using digital pulse shape analysis of phoswich detector signals," *IEEE Trans. Nucl. Sci.*, vol. 53, no. 2, pp. 620–624, Apr. 2006.

[60] A. T. Farsoni, D. M. Hamby, K. D. Ropon, and S. E. Jones, "A two-channel phoswich

detector for dual and triple coincidence measurements of radioxenon isotopes," DTIC Document, 2007.

[61] A. Farsoni and D. M. Hamby, "Characterizing a two-channel phoswich detector using radioxenon isotopes produced in the Oregon State Universty TRIGA reactor," presented at the 2010 Monitoring Research Review: Ground-Based Nuclear Explosion Monitoring Technologies, 2010.

[62] A. T. Farsoni, D. M. Hamby, C. S. Lee, and A. J. Elliot, "Preliminary experiments with a triple-layer phoswich detector for radioxenon detection," DTIC Document, 2008.

[63] A. T. Farsoni and D. M. Hamby, "Design and modeling of a Compton-suppressed phoswich detector for radioxenon monitoring," DTIC Document, 2010.

[64] A. T. Farsoni, B. Alemayehu, A. Alhawsawi, and E. M. Becker, "A Phoswich Detector With Compton Suppression Capability for Radioxenon Measurements," *IEEE Trans. Nucl. Sci.*, vol. 60, no. 1, pp. 456–464, Feb. 2013.

[65] M. J. A. de Voigt, J. C. Bacelar, S. L. Micek, P. Schotanus, B. A. W. Verhoef, Y. J. E. Wintraecken, and P. Vermeulen, "A novel compact Ge-BGO Compton-suppression spectrometer," *Nucl. Inst Methods Phys. Res. A*, vol. 356, no. 2, pp. 362–375, 1995.

[66] A. . . Farsoni, B. Alemayehu, A. Alhawsawi, and E. M. Becker, "A compton-suppressed phoswich detector for gamma spectroscopy," *J. Radioanal. Nucl. Chem.*, vol. 296, no. 1, pp. 63–68, 2013.

[67] "http://www.avicennainstruments.com/," Jan-2016. .

[68] G. Le Petit, A. Cagniant, P. Gross, G. Douysset, S. Topin, J. P. Fontaine, T. Taffary, and C. Moulin, "SPALAX^{TM} new generation: A sensitive and selective noble gas system for nuclear explosion monitoring," *Appl. Radiat. Isot.*, vol. 103, pp. 102–114, Sep. 2015.

[69] V. Doost-Mohammadi, H. Afarideh, G. R. Etaati, M. J. Safari, and H. Rouhi, "INGAS: Iranian Noble Gas Analyzing System for radioxenon measurement," *Radiat. Phys. Chem.*, vol. 120, pp. 26–32, Mar. 2016.

[70] P. N. Luke, "Single-polarity charge sensing in ionization detectors using coplanar electrodes," *Appl. Phys. Lett.*, vol. 65, no. 22, p. 2884, 1994.

[71] W. Shockley, "Currents to conductors induced by a moving point charge," *J. Appl. Phys.*, vol. 9, no. 10, pp. 635–636, 1938.

[72] S. Ramo, "Currents induced by electron motion," *Proc Ire*, vol. 27, no. 9, pp. 584–585, 1939.

[73] Z. He, "Review of the Shockley–Ramo theorem and its application in semiconductor gamma-ray detectors," *Nucl. Instrum. Methods Phys. Res. Sect. Accel. Spectrometers Detect. Assoc. Equip.*, vol. 463, no. 1, pp. 250–267, 2001.

[74] L. Bläckberg, A. Fay, I. Jõgi, S. Biegalski, M. Boman, K. Elmgren, T. Fritioff, A. Johansson, L. Mårtensson, F. Nielsen, A. Ringbom, M. Rooth, H. Sjöstrand, and M. Klintenberg, "Investigations of surface coatings to reduce memory effect in plastic scintillator detectors used for radioxenon detection," *Nucl. Instrum. Methods Phys. Res. Sect. Accel. Spectrometers Detect. Assoc. Equip.*, vol. 656, no. 1, pp. 84–91, Nov. 2011.

[75] G. Knoll, *Radiation Detection and Measurement*, 4th ed. John Wiley and Sons, 2010.

[76] "http://www.ansys.com/Products/Electronics/ANSYS-Maxwell," Jan-2016. .

[77] “http://research.engr.oregonstate.edu/masc/content/thermal-evaporation,” Jan-2016. .
[78] K. Qin, L. Wang, J. Zhang, J. Min, J. Huang, X. Liang, K. Tang, and Y. XIA, “A two-step deposition process for electrode fabrication of CdZnTe detectors,” *Vacuum*, vol. 86, no. 7, pp. 827–829, 2012.
[79] A. Burgur, H. Chen, K. Chattopadhyay, D. Shi, S. Morgan, W. Collins, and R. . James, “Characterization of metal contacts on and surfaces of cadmium zinc telluride,” *Nucl. Instrum. Methods Phys. Res. A*, vol. 428, pp. 8–13, 1999.
[80] “http://redlen.ca/,” Jan-2016. .
[81] “http://3dprintingforbeginners.com/filamentprimer-2,” Feb-2016. .
[82] “http://www.pchemlabs.com/product.asp?pid=2144,” 2015. .
[83] Goorley, “MCNP6.1.1-Beta Release Notes.” MCNP6.1.1-Beta Release Notes, 2014.
[84] S. Zarei, “A Monte Carlo Simulation of the Compton camera.” Thesis, San Diego State University, 2010.
[85] “https://www.python.org,” Feb-2016. .
[86] Z. He, G. F. Knoll, and D. K. Wehe, “Direct measurement of product of the electron mobility and mean free drift time of CdZnTe semiconductors using position sensitive single polarity charge sensing detectors,” 1998.
[87] R. Redus, “Application Note ANCZT-2 Rev. 3, Charge Trapping in XR-100T-CdTe and CZT Detectors.” Amptek, 2007.
[88] “http://www.isoflex.com/xenon-xe,” Jan-2016. .
[89] A. Ringbom, T. Larson, A. Axelsson, K. Elmgren, and C. Johansson, “SAUNA—a system for automatic sampling, processing, and analysis of radioactive xenon,” *Nucl. Instrum. Methods Phys. Res. Sect. Accel. Spectrometers Detect. Assoc. Equip.*, vol. 508, no. 3, pp. 542–553, Aug. 2003.
[90] P. . Reeder, T. . Bowyer, J. . McIntyre, W. . Pitts, A. Ringbom, and C. Johansson, “Gain calibration of a β/γ coincidence spectrometer for automated radioxenon analysis,” *Nucl. Instrum. Methods Phys. Res. Sect. Accel. Spectrometers Detect. Assoc. Equip.*, vol. 521, no. 2–3, pp. 586–599, Apr. 2004.
[91] M. W. Cooper, J. I. McIntyre, T. W. Bowyer, A. J. Carman, J. C. Hayes, T. R. Heimbigner, C. W. Hubbard, L. Lidey, K. E. Litke, S. J. Morris, M. D. Ripplinger, R. Suarez, and R. Thompson, “Redesigned β–γ radioxenon detector,” *Nucl. Instrum. Methods Phys. Res. Sect. Accel. Spectrometers Detect. Assoc. Equip.*, vol. 579, no. 1, pp. 426–430, Aug. 2007.
[92] J. Schulze, M. Auer, and R. Werzi, “Low level radioactivity measurement in support of the CTBTO,” *Appl. Radiat. Isot.*, vol. 53, no. 1, pp. 23–30, 2000.
[93] J. I. McIntyre, T. W. Bowyer, and P. L. Reeder, *Calculation of minimum detectable concentration levels of radioxenon isotopes using the PNNL ARSA system*. Pacific Northwest National Laboratory, 2006.
[94] W. Hennig, C. E. Cox, S. J. Asztalos, H. Tan, P. J. Franz, P. M. Grudberg, and W. K. Warburton, “Study of silicon detectors for high-resolution radioxenon measurements,” *Nucl. Instrum. Methods Phys. Res. A*, vol. 652, pp. 216–220, 2011.
[95] K. M. Foltz Biegalski and S. R. Biegalski, “Determining detection limits and minimum

detectable concentrations for noble gas detectors utilizing beta-gamma coincidence systems," *J. Radioanal. Nucl. Chem.*, vol. 248, no. 3, pp. 673–682, 2001.

[96] G. Le Petit, P. Armand, G. Brachet, T. Taffary, J. P. Fontaine, P. Achim, X. Blanchard, J. C. Piwowarczyk, and F. Pointurier, "Contribution to the development of atmospheric radioxenon monitoring," *J. Radioanal. Nucl. Chem.*, vol. 276, no. 2, pp. 391–398, May 2008.

[97] P. N. Luke, C. S. Tindall, and M. Amman, "Proximity Charge Sensing With Semiconductor Detectors," *IEEE Trans. Nucl. Sci.*, vol. 56, no. 3, pp. 808–812, Jun. 2009.

7 Appendices

7.1 An Example of the MCNP Deck for Generating PTRAC Files of 346 keV betas from ^{133}Xe

```
C   CZT Radioxenon Detection system (2 elements)
C  Generating PTRAC files and calculate detection efficiency of the TECZT
C Xe-133 346keV beta
C written by    Lily Ranjbar
C               PhD Student
C               Department of Nuclear science and engineering
C               Oregon state University
C ********************************Cell Cards*********************************
100  1  -0.0045011   -1    -2    -3    4   5    6          imp:e=1 imp:p=1          $Gas cell
200  2  -1.32    -11    12    -7    -8    9   10 #100 #300 #400    imp:e=1 imp:p=1    $Polylactic
acid
300  3  -6          1    -2    -3    4   6   -13          imp:e=1 imp:p=1   $CdZnTe 1
400  3  -6         -2    -3    4   -5   6    14          imp:e=1 imp:p=1   $CdZnTe 2
500  0             #100 #200 #300 #400                  imp:e=0 imp:p=0             $Outside
world

C ******************************Surface Cards********************************
1    pz   0.5
2    py   0.475
```

```
3    px   0.475
4    py  -0.475
5    pz  -0.5
6    px  -0.475
7    py   1.6
8    px   1.6
9    py  -1.6
10   px  -1.6
11   pz   0.8
12   pz  -0.8
13   pz   1.5
14   pz  -1.5

C ******************************Material Cards*****************************
m1   7000   0.3
     54133  0.7    $Mixture of 133Xe and Nitrogen as the carrier
m2   6000   3    1001  4     8016   2
m3   48000  0.45 30000  0.05  52000  0.5
mode e

C ******************************Source Card********************************
```

```
SDEF ERG=d1 X=d2 Y=d3 Z=d4  CEL=100 PAR=3         $Xe-133
si1  H  0  0.01    0.02     0.04    0.1     0.3     0.346
sp1  D  0  6.448   6.2496   11.904  30.851  43.449  0.413 $intensity of 99.2% of beta's is
considered.
si2  -0.475  0.475      $ x-range limits for source volume
sp2   0      1            $ uniform probability over x-range
si3  -0.475  0.475      $ y-range limits for source volume
sp3   0      1            $ uniform probability over y-range
si4  -0.5    0.5          $ z-range limits for source volume
sp4   0      1             $ uniform probability over z-range

C ********************************History*******************************
nps  1e7
PTRAC file=asc write=all event=sur,col,ter  max=1e8 &
 filter=0.01,0.4,erg type=e

C ********************************Tallies*******************************
f8:e 300 400 (300 400)
e8 0 0.02  379i .400  $maximum cut off energy set at 400kev to avoid loosing information
for 346kev
ft8 GEB 1.0210e-02 1.8280e-03 3.7310e+00 $ energy broadening parameters for ft8 tally
```

card extracted from a thesis

print 110

7.2 An Example of the MCNP Deck for Generating PTRAC Files of 31 keV X-rays from ^{133}Xe

```
C CZT Radioxenon Detection system (2 elements)
C  Generating PTRAC files and calculate detection efficiency of the TECZT
C Xe-133 31keV X-rays
C written by    Lily Ranjbar
C               PhD Sudent
C               Department of Nuclear science and engineering
C               Oregon state University

C*********************************Cell Cards*********************************
100  1  -0.0045011   -1    -2    -3    4   5    6          imp:e=1 imp:p=1          $Gas cell
200  2  -1.32    -11    12    -7    -8    9   10 #100 #300 #400  imp:e=1 imp:p=1   $Polylactic
acid
300  3  -6          1    -2    -3    4   6   -13          imp:e=1 imp:p=1   $CdZnTe 1
400  3  -6         -2    -3    4   -5   6    14          imp:e=1 imp:p=1   $CdZnTe 2
500  0            #100 #200 #300 #400                imp:e=0 imp:p=0          $Outside world

C*****************************Surface Cards******************************
1    pz   0.5
2    py   0.475
3    px   0.475
```

```
4    py  -0.475
5    pz  -0.5
6    px  -0.475
7    py   1.6
8    px   1.6
9    py  -1.6
10   px  -1.6
11   pz   0.8
12   pz  -0.8
13   pz   1.5
14   pz  -1.5

C*****************************Material Cards*****************************
m1   7000   0.3
       54133  0.7    $Mixture of 133Xe and Nitrogen as the carrier
m2   6000   3    1001 4     8016  2
m3   48000  0.45 30000 0.05  52000 0.5
mode p
C*****************************Source Card*******************************
SDEF ERG=0.031 X=d1 Y=d2 Z=d3  CEL=100 PAR=2 $Xe-133
si2  -0.475  0.475      $ x-range limits for source volume
```

```
sp2   0      1              $ uniform probability over x-range
si3  -0.475  0.475         $ y-range limits for source volume
sp3   0      1              $ uniform probability over y-range
si4  -0.5    0.5            $ z-range limits for source volume
sp4   0      1              $ uniform probability over z-range

C ********************************History********************************
nps  1e7
PTRAC file=asc write=all event=sur,col,ter  max=1e8 filter=0.005,0.1,erg type=p
C ********************************Tallies********************************
f8:p 300 400 (300 400)
e8 0 0.020 79i .1 $maximum cut off energy set at 100keV to avoid losing information for
31 keV
ft8 GEB 1.0210e-02 1.8280e-03 3.7310e+00
print 110
```

7.3 An Example of the Python Code Used to Parse the PTRAC Files and Extract Energy and NPS Information in One of the CZT Crystals.

```
% extracting energy information for all NPS numbers in CZT 2 (cell number in MCNP=400)

%% import required libraries
import sys
import os
import re

acceptable_cell_number = [400];
acceptable_end_reaction_types = [9000];  %9000 is end of one reaction
out_index = 0;
ignoreLine = 10;

def checkNumber(number, acceptable_numbers):
  length = len(acceptable_numbers);
  for i in range(0, length):
    if number == acceptable_numbers[i]:
      return True;
  return False;

def checkExistance(given_list, acceptable_numbers):
  length = len(acceptable_numbers);
  for i in range(0, length):
    if acceptable_numbers[i] in given_list:
      return True;
  return False;

def getExistanceIndecies(given_list, acceptable_numbers):
  indecies = [];
  length = len(given_list);
  for i in range(0, length):
    if checkNumber(given_list[i], acceptable_numbers):
      indecies.append(i);
  return indecies;
def writeHead(outFile):
  outFile.write('|ID\t\t|NPS\t\t\t\t|Cell_Number\t\t\t\t|Energy\n');

def getPrintString(NPS, energy):
```

```
  global out_index;
  global acceptable_cell_number;

  out_index = out_index + 1;
  sstring = '|' + str(out_index) + '\t\t|' + str(NPS) + '\t\t\t\t|' +
str(acceptable_cell_number[0]) + '\t\t\t\t\t\t|' + str(energy) + '\n';
  return sstring;
# def process_expriment(NPS, reaction_types, cell_numbers, event_infos, event_count,
outFile):
#   global acceptable_cell_number

#   is_accepted = 1;

#   ''' start of filtering '''

#                   if not (checkNumber(reaction_types[event_count-1],
acceptable_end_reaction_types)):
#     is_accepted = 0;
#   if is_accepted == 1:
#     for i in range(0, event_count):
#       if not (checkNumber(cell_numbers[i], acceptable_cell_number)):
#         is_accepted = 0;
#         break;

#   ''' end of filtering '''

#   if is_accepted == 1:
#           outFile.write(getPrintString(NPS, reaction_types, cell_numbers, event_infos,
event_count));
def check_validity(sample):
  global acceptable_cell_number;
  cell_numbers = sample['cell_numbers'];
  event_count = sample['event_count'];
  event_infos = sample['event_infos'];

  if checkExistance(cell_numbers, acceptable_cell_number):
    energy = 0;
    indecies = getExistanceIndecies(cell_numbers, acceptable_cell_number);
    indecies_len = len(indecies);
    NPS = sample['NPS'];
    if indecies_len == event_count:
      ''' all cell_numbers is acceptable '''
```

```
      info = event_infos[0];
      energy = float(info[6]);
    elif indecies_len > 0:
      for i in range(0,indecies_len):
        info = event_infos[indecies[i]];
        energy = energy + float(info[6]);
        if indecies[i]+1 < event_count:
          info = event_infos[indecies[i]+1];
          energy = energy - float(info[6]);

    return (NPS, energy, 1 if energy > 0 else 0);

  return (0, 0, 0);


def process_experiments(collection, outFile):
  print 'start processing .....';
  collection_len = len(collection);
  print 'len of collection: ' + str(collection_len)
  for i in range(0,collection_len):
    (NPS, energy, validity) = check_validity(collection[i]);
    if validity == 1:
      ''' write into file: '''
      outFile.write(getPrintString(NPS, energy));
def main(args):

  ''' sample code for calling this program: python lily.py 31_Kev_X-ray_Test.txt out.txt
'''

  adr = os.getcwd() + '/' + args[1];  ''' input file address'''
  outAdr = os.getcwd() + '/' + args[2];
  try:
    ignoreLine = int(args[3]);
  except:
    ignoreLine = 10;
  outFile = open(outAdr, 'w');
  writeHead(outFile);

  counter = 0;
  newDataLen = 3;
  NPS = 0;
  reaction_types = [];
```

```
  cell_numbers = [];
  event_infos = [];
  event_count = 0;
  ignore_counter = 0;
  collection = [];
  encounter_error = 0;
  for line in open(adr):
    ignore_counter = ignore_counter + 1;
    if ignore_counter > ignoreLine:
      ''' processing the line '''
      line = line.strip(); ''' remove whitespace of the start of each line '''
      line = re.sub(" +", " ", line);  ''' remove whitespace among the line using regular expression (+ mean it should contain one for sure) '''
      ''' extracting information '''
      particle = line.rstrip().split(' '); ''' this line seprate data that exist in one line and represent them as an array (particle) '''
      particle_len = len(particle);
      try:
        if  particle_len > 1:
          if particle_len <= newDataLen:
            if event_count > 0 and encounter_error == 0:

              sample = {};
              sample.setdefault('NPS', 0);
              sample['NPS'] = NPS;
              sample.setdefault('reaction_types', 0);
              sample['reaction_types'] = reaction_types;
              sample.setdefault('cell_numbers', 0);
              sample['cell_numbers'] = cell_numbers;
              sample.setdefault('event_infos', 0);
              sample['event_infos'] = event_infos;
              sample.setdefault('event_count', 0);
              sample['event_count'] = event_count;

              collection.append(sample);
            ''' reset variables '''
            encounter_error = 0;
            counter = 0;
            event_count = 0;
            reaction_types = [];
            cell_numbers = [];
            event_infos = [];
```

```
            event_count = 0;
            # try:
            NPS = int(particle[0]);
            # except:
            #   print line;
            #   sys.exit();

          else:
            if counter % 2 == 1:
              # try:
              reaction_types.append(int(particle[0]));
              cell_numbers.append(int(particle[4]));
              # except:
              #   print line;
              #   sys.exit();
            else:
              event_count = event_count + 1;
              event_infos.append(particle);

      except:
        encounter_error = 1;
      counter = counter + 1;
  print 'end of collecting data ...'
  print 'start processing collection ...'
  process_experiments(collection, outFile);

if __name__ == "__main__":
          main(sys.argv)
```

7.4 An Example of the Python Code Used to Extract Coincidence events between the two detector from the Parsed PTRAC Files

% extracting coincidence events between CZT1 & CZT2 from the Parsed PTRAC files

```
%% import required libraries
 import sys
 import os
 import re

 ignoreLine = 1;

 def checkNumber(number, acceptable_numbers):
   length = len(acceptable_numbers);
   for i in range(0, length):
     if number == acceptable_numbers[i]:
       return True;

   return False;

 def writeHead(outFile):

   outFile.write('|ID\t|NPS\t|Energy1\t|Energy2\n');

 def getPrintString(set_id, NPS, energy1, energy2):

   sstring = '|' + str(set_id) + '\t|' + str(NPS) + '\t|' + str(energy1) + '\t|' + str(energy2) + '\n';
   return sstring;

 def extract_coincidence(in1_data, in2_data, outFile):

   set_id = 0;

   acceptable_npss = [];

   ''' go over all nps that exists in first file '''
   for nps in in1_data.keys():
     ''' check that the specific NPS in file 1 exists in file 2 or not '''
     if nps in in2_data:
       acceptable_npss.append(nps); ''' store the NPS that exists in both files '''

   acceptable_npss.sort();  ''' sort based on NPS values '''
```

```
    acceptedEventCount = len(acceptable_npss);  ''' extract the number of coincidence NPS '''
    for i in range(0, acceptedEventCount):
      nps = acceptable_npss[i];
      set_id = set_id + 1; ''' increment the ID of coincidence events '''
      outFile.write(getPrintString(set_id, nps, in1_data[nps], in2_data[nps])); ''' print coincidence events based on sorted NPS '''

  def writeHead_3_in(outFile):

    outFile.write('|ID\t|NPS\t|Energy1\t|Energy2\t|Energy3\n');

  def getPrintString_3_in(set_id, NPS, energy1, energy2, energy3):

    sstring = '|' + str(set_id) + '\t|' + str(NPS) + '\t|' + str(energy1) + '\t|' + str(energy2) + '\t|' + str(energy3) + '\n';
    return sstring;

  def extract_coincidence_3_in(in1_data, in2_data, in3_data, outFile):

    set_id = 0;

    acceptable_npss = [];

    ''' go over all nps that exists in first file '''
    for nps in in1_data.keys():
      ''' check that the specific NPS in file 1 exists in file 2 or not '''
      if nps in in2_data:
        if nps in in3_data:
          acceptable_npss.append(nps); ''' store the NPS that exists in both files '''

    acceptable_npss.sort();  ''' sort based on NPS values '''

    acceptedEventCount = len(acceptable_npss);  ''' extract the number of coincidence NPS '''
    for i in range(0, acceptedEventCount):
      nps = acceptable_npss[i];
      set_id = set_id + 1; ''' increment the ID of coincidence events '''
      outFile.write(getPrintString_3_in(set_id, nps, in1_data[nps], in2_data[nps], in3_data[nps])); ''' print coincidence events based on sorted NPS '''


  def main(args):
```

```
global acceptable_end_reaction_types

''' sample code for calling this program: python lily.py 31_Kev_X-ray_Test.txt out.txt '''
main_adr = os.getcwd();
adr1 = main_adr + '/' + args[1];  ''' input1 file address'''
adr2 = main_adr + '/' + args[2];  ''' input2 file address'''
outAdr = main_adr + '/' + args[3];
adr3 = main_adr + '/' + args[3];
contains_3_files = 1;
try:
  adr3 = outAdr;
  outAdr = main_adr + '/' + args[4];
except:
  contains_3_files = 0;

ignoreLine = 1;

outFile = open(outAdr, 'w');

writeHead(outFile);

in1_data = {};
in2_data = {};
in3_data = {};
ignore_counter = 0;


for line in open(adr1):
  ignore_counter = ignore_counter + 1;
  if ignore_counter > ignoreLine:
    ''' processing the line '''
    line = line.strip(); ''' remove whitespace of the start of each line '''
    line = re.sub("\|", "", line);  ''' remove | signs from the lines '''
        line = re.sub("\t+", " ", line);  ''' remove tabs among the line using regular expression
  (+ mean it should contain one for sure) '''
    ''' extracting information '''
        particle = line.rstrip().split(' '); ''' this line seprate data that exist in one line and
  represent them as an array (particle) '''
    NPS = int(particle[1]); ''' extract NPS '''
        in1_data.setdefault(NPS, 0); ''' this line just add NPS type to the dictionary (in1_data)
  after this line, you
```

```
                                you can put a value in in1_data[NPS]'''
    in1_data[NPS] = particle[3]; ''' storing energy of NPS in the dictionary (in1_data) '''



 ignore_counter = 0; ''' reset ignore counter '''

 for line in open(adr2):
  ignore_counter = ignore_counter + 1;
  if ignore_counter > ignoreLine:
   ''' processing the line '''
   line = line.strip(); ''' remove whitespace of the start of each line '''
   line = re.sub("\|", "", line);  ''' remove | signs from the lines '''
       line = re.sub("\t+", " ", line);  ''' remove tabs among the line using regular expression
  (+ mean it should contain one for sure) '''
   ''' extracting information '''
       particle = line.rstrip().split(' '); ''' this line seprate data that exist in one line and
  represent them as an array (particle) '''
   NPS = int(particle[1]);  ''' extract NPS '''
       in2_data.setdefault(NPS, 0);   ''' this line just add NPS type to the dictionary
  (in2_data) after this line, you
                                you can put a value in in2_data[NPS]'''
   in2_data[NPS] = particle[3]; ''' storing energy of NPS in the dictionary (in2_data) '''



 if contains_3_files == 1:
  ignore_counter = 0; ''' reset ignore counter '''

  for line in open(adr3):
   ignore_counter = ignore_counter + 1;
   if ignore_counter > ignoreLine:
    ''' processing the line '''
    line = line.strip(); ''' remove whitespace of the start of each line '''
    line = re.sub("\|", "", line);  ''' remove | signs from the lines '''
        line = re.sub("\t+", " ", line);  ''' remove tabs among the line using regular expression
  (+ mean it should contain one for sure) '''
    ''' extracting information '''
    particle = line.rstrip().split(' '); ''' this line seprate data that exist in one line and
represent them as an array (particle) '''
    NPS = int(particle[1]);  ''' extract NPS '''
    in3_data.setdefault(NPS, 0);  ''' this line just add NPS type to the dictionary (in2_data)
```

```
    after this line, you
                                    you can put a value in in2_data[NPS] '"
        in3_data[NPS] = particle[3]; '" storing energy of NPS in the dictionary (in2_data) '"

      if contains_3_files == 0:
        extract_coincidence(in1_data, in2_data, outFile);  '" extract and store coincidence events
'"
      else:
        extract_coincidence_3_in(in1_data, in2_data, in3_data, outFile);   '" extract and store
coincidence events '"

    if __name__ == "__main__":
        main(sys.argv)
```

7.5 An Example of the MATLAB Script Used to Generate 2D beta-gamma Coincidence Spectrum for ^{135}Xe

```
Xe135_1=xlsread('Xe135_Final.xlsx','Sheet1')*1000; %First Set
of Coincidence Events
[m,n] = size(Xe135_1);
Coinc1= zeros(1200);
for i = 1:88680
        X =
ceil(normrnd(Xe135_1(i,1),(0.03/2.35)*Xe135_1(i,1)));
        Y = ceil(Xe135_1(i,2));
        for j=1:1200
            Coinc1(X,Y) = Coinc1(X,Y)+1;
        end
 end

Xe135_2=xlsread('Xe135_Final.xlsx','Sheet2')*1000; %Second Set
of Coincidence Events
[m,n] = size(Xe135_2);
for i = 1:87012
       Y =
ceil(normrnd(Xe135_2(i,1),(0.03/2.35)*Xe135_2(i,1)));
       X = ceil(Xe135_2(i,2));
        for j=1:1200
            Coinc1(X,Y) = Coinc1(X,Y)+1;
        end
end

for i=1:9881 %gamma-gamma in 2 CZT
       X =
ceil(normrnd(Xe135_1(i,4),(0.03/2.35)*Xe135_1(i,4)));
       Y =
ceil(normrnd(Xe135_2(i,4),(0.03/2.35)*Xe135_2(i,4)));
        for j=1:280
            Coinc1(X,Y) = Coinc1(X,Y)+1;
        end

end

figure(1)
h=surfc(Coinc1)
set(h,'LineStyle','none')
set(gca, 'FontSize', 12)
```

```
colorbar
colormap jet
xlabel('Energy (keV), CZT1','Fontsize', 14);ylabel('Energy
(keV), CZT2','Fontsize', 14);title('135Xe Beta-Gamma
Coincidence');
hold on

figure(2)
histogram(Xe135_1(:,9),150);xlabel({'Energy
(keV)'});ylabel({'Counts'});title('135Xe Gamma Coincidence
Events in CZT1');
figure(3)
histogram(Xe135_1(:,2),910);xlabel({'Energy
(keV)'});ylabel({'Counts'});title('135Xe Beta Coincidence
Events in CZT2');
figure(4)
histogram(Xe135_2(:,9),150);xlabel({'Energy
(keV)'});ylabel({'Counts'});title('135Xe Gamma Coincidence
Events in CZT2');
figure(5)
histogram(Xe135_2(:,2),910);xlabel({'Energy
(keV)'});ylabel({'Counts'});title('135Xe Beta Coincidence
Events in CZT1');
figure(6)
histogram(Xe135_1(:,6),910);xlabel({'Energy
(keV)'});ylabel({'Counts'});title('135Xe Beta-Gamma Coincidence
Events in CZT1');
figure(7)
histogram(Xe135_2(:,6),910);xlabel({'Energy
(keV)'});ylabel({'Counts'});title('135Xe Beta-Gamma Coincidence
Events in CZT2');
```

7.6 An Example of the MATLAB Code Used to Communicate Between FPGA and PC, Shape Pulses and Extract Energy Deposited in each CZT Detector

```
m=100000;
bm=5;

timing_array = zeros(1,m);
display =0;
sl=0.0001;
save_data=1;
gain_1 = 1900;
gain_2 = 1900;
offset_1 = 3200;
offset_2 = 2800;



Th_1=85;
Th_2=95;

% Set the RUN MODE
% Run Mode = 0 : Free Runing
% Run Mode = 1 : Syncronized
% Run Mode = 3 : Syncronized and Coincidence events
only
run_mode = 0;
setwireinvalue(xem,16,run_mode*2048,14336);

% Set coincidence window
coin_th =200;
setwireinvalue(xem,16,coin_th*8,2040);
updatewireins(xem);



n=150;
filter_trapiz = [ones(1,n)/-n zeros(1,200)
ones(1,n)/n];
```

```
max_energy= 1000;           % Maximum energy
bin_num= 1000;              % Number of bins
bin_energy = 0: max_energy/(bin_num -1) : max_energy;
%Energy bins
bin=1:bin_num;
a1 =0;
a2 =0;
b1 =double(1.335);
b2 = double(1.211);

% Set the threshold
Th16_1=uint16(Th_1);
Th16_2=uint16(Th_2);
setwireinvalue(xem,17,Th16_1,65535);        % Ch 1
setwireinvalue(xem,18,Th16_2,65535);         % Ch 2
updatewireins(xem);

% Set the gain
setwireinvalue(xem,8,24,65535);         %Ch 1
setwireinvalue(xem,9,gain_1*16,65535);
updatewireins(xem);
activatetriggerin(xem,64,0);

setwireinvalue(xem,8,27,65535);          %Ch 2
setwireinvalue(xem,9,gain_2*16,65535);
updatewireins(xem);
activatetriggerin(xem,64,0)

% Set the offset
setwireinvalue(xem,8,25,65535);         %Ch 1
setwireinvalue(xem,9,(offset_1)*16,65535);
updatewireins(xem);
activatetriggerin(xem,64,0);

setwireinvalue(xem,8,26,65535);          %Ch 2
setwireinvalue(xem,9,(offset_2)*16,65535);
updatewireins(xem);
```

```
activatetriggerin(xem,64,0);

% Reset
setwireinvalue(xem,16,3,0);     % Ch 1
updatewireins(xem);

% RunSys High
setwireinvalue(xem,16,1,1);     % Ch 1
setwireinvalue(xem,16,2,2);     % Ch 2
updatewireins(xem);



for R= 1:bm

    if save_data ==1
        ch_1=zeros(m,1024);
        ch_2=zeros(m,1024);
    end
    energy_1= zeros(1,m);
    energy_2= zeros(1,m);

    valid=0;
    loop=0;
    while m ~= valid;

        updatewireouts(xem);
        pt=getwireoutvalue(xem,32);

        while bitand(pt,7)==0
            updatewireouts(xem);
            pt=getwireoutvalue(xem,32);
        end


        if(R==bm && m==valid+1)
            setwireinvalue(xem,16,0,3);
            setwireinvalue(xem,16,0,14336);
```

```
            updatewireins(xem);
        end


        buf_1 = readfrompipeout(xem,160,2048); %CH 1
        buf_2 = readfrompipeout(xem,161,2048); %CH 2

        for k=1:1024
            j=k*2;
            data_1(k)=uint16(buf_1(j))*256 +
uint16(buf_1(j-1));
        end

        for k=1:1024
            j=k*2;
            data_2(k)=uint16(buf_2(j))*256 +
uint16(buf_2(j-1));
        end

        data_1 =double(data_1);
        data_2 =double(data_2);


        base_1= mean(data_1 (50:150));
        base_2= mean(data_2 (50:150));



        data_1_b=data_1 - base_1;
        data_2_b=data_2 - base_2;

        filter_1 = conv(data_1_b, filter_trapiz);
        filter_2 = conv(data_2_b, filter_trapiz);

        amp_1=max(filter_1)/2;
        amp_2=max(filter_2)/2;
```

```
        if pt==3
            valid=valid+1;
            timing_array (valid) =pt;

            energy_1(valid) = a1 + (b1 * amp_1);
            energy_2(valid) = a2 + (b2 * amp_2);

            if save_data ==1
                ch_1(valid,:)=data_1;
                ch_2(valid,:)=data_2;
            end


            if display ==1

                subplot(2,2,1); %CH 1 Waveforms
                plot(data_1, 'r', 'LineWidth',
3,'markersize',3)
                hold on
                plot(filter_1,'b','LineWidth', 3)
                title('Waveform 1')
                xlabel('Sample#');ylabel('ADC');
                axis([0 1024 0 4095])
                grid on
                hold off

                subplot(2,2,2); %CH 2 Waveforms
                plot(data_2, 'r', 'LineWidth',
3,'markersize',3)
                hold on
                plot(filter_2,'b','LineWidth', 3)
                title('Waveform 2')
                xlabel('Sample#');ylabel('ADC');
                axis([0 1024 0 4095])
                grid on
                hold off
```

```
                spec_1 =
hist(energy_1(1:valid),bin_energy);
                spec_2 =
hist(energy_2(1:valid),bin_energy);

                max_counts_1 = max(spec_1(2:bin_num-
1));
                max_counts_1 = max_counts_1 * 1.1;
                max_counts_2 = max(spec_2(2:bin_num-
1));
                max_counts_2 = max_counts_2 * 1.1;
                if max_counts_1 ==0; max_counts_1=1;
end
                if max_counts_2 ==0; max_counts_2=1;
end

                subplot(2,2,3); % MCA 1
                plot(bin_energy,
spec_1,'k','LineWidth',2,'MarkerSize',3),xlabel('Energ
y (keV)'),ylabel('Counts')
                title('MCA 1')
                axis([2 max_energy 0 max_counts_1])
                grid on

                subplot(2,2,4); % MCA 2
                plot(bin_energy,
spec_2,'k','LineWidth',2,'MarkerSize',3),xlabel('Energ
y (keV)'),ylabel('Counts')
                title('MCA 2')
                axis([2 max_energy 0 max_counts_2])
                grid on

            end

        else
            activatetriggerin(xem,64,1);
        end
```

```
        pause(sl)
        loop = loop +1
        pt
        valid

        disp('----------------------');
    end

    if save_data ==1
        filename_energy = ['Results\General
Characterization\Lab
Sources\Cs137\8_Jan_2016\Energy_Array_' num2str(R)];
        filename_pulses = ['Results\General
Characterization\Lab
Sources\Cs137\8_Jan_2016\Pulse_Array_' num2str(R)]
        save (filename_energy, 'energy_1', 'energy_2')
        save (filename_pulses, 'ch_1', 'ch_2',
'timing_array')
    end

end
```